
LWFA Diagnostics Development for ATLAS-300 and Nonlinear Plasma Wavelength Scalings

Hao Ding



Munich 2021

LWFA Diagnostics Development for ATLAS-300 and Nonlinear Plasma Wavelength Scalings

Hao Ding

Dissertation
an der Fakultät für Physik
der Ludwig-Maximilians-Universität
München

vorgelegt von
Hao Ding
aus Shanxi

München, den 11. 11. 2021

Erstgutachter: Prof. Dr. Stefan Karsch
Zweitgutachter: Prof. Dr. Carl B. Schroeder
Tag der mündlichen Prüfung: 1. Februar 2022

Zusammenfassung

LWFA steht für Laser WakeField Acceleration (oder Accelerator), einer neuen Technologie, die eine drastische Reduzierung der Größe und Kosten von Teilchenbeschleunigern verspricht. LWFA beruht auf dem großen (\sim GV/cm) elektrischen Feld in der Plasmawelle, die durch Laserpulse mit relativistischer Spitzenintensität (10^{18} W/cm²) angeregt wird. Im Rahmen dieser Dissertation wurden die für die LWFA-Forschung am Ti:Saphir Laser ATLAS-300 am Laboratory for Extreme Photonics der Ludwig-Maximilians-Universität München geeignete Diagnostiken entwickelt, sowohl für Charakterisierung der Elektronen als auch zur Untersuchung des Plasmamediums. Zur Elektronendiagnostik wurden Implementierung und Charakterisierung von Szintillationsschirmen und Permanentdipolmagneten durchgeführt. Zur Plasmadiagnose wurde ein Probestrahl mit wenigen Zyklen entwickelt, mit dessen Hilfe fs-Schnappschüsse der Plasmawelle ermöglicht wurden.

Konkret wurde die Lichtemissionseffizienz von neun gängigen Szintillationsschirmtypen mit Elektronenstrahlen des ELBE Linac am Helmholtz Zentrum Dresden-Rossendorf kalibriert. Bestehende Verfahren zur Übertragung der absoluten Kalibrierergebnisse in eine Kreuzkalibrierung mit einer Konstantlichtquelle wurden entscheidend verbessert. Bezüglich des Dipolmagneten wurde die Verteilung des B-Feldes in der Nähe der Mittelebene des Spalts mit einem Hall-Sensor gemessen und die Elektronen wurde in General Particle Tracer mit der gemessenen Feldverteilung getrackt. Szintillationsschirme und der Dipolmagnet bildeten das Elektronenspektrometer, das eine energieaufgelöste Nachweis von im LWFA erzeugten Elektronenstrahlen ermöglichte. Selbstinjizierte Elektronenstrahlen mit mehreren hundert pC Ladung und Spitzenenergien über 1 GeV wurden in einer mit Wasserstoff gefüllten Gaszelle unterschiedlicher Länge beschleunigt. Durch die Injektion an Stoßfronten in überschallenden Gasstrahlen wurden stabile Elektronenstrahlen mit einer spektralen Dichte über 10 pC/MeV dank einer prozentualen Energieverteilung erreicht.

Das Highlight dieser Arbeit ist der Aufbau und die Anwendung eines auf Hohlfasern basierenden Pulskompressionsaufbaus, der während der Experimente als Probestrahl dient. Dieser Aufbau lieferte sub-10 fs Probepulse, mit denen Phasenkontrast-Schnappschüsse der Laser-Plasma-Wechselwirkung aufgezeichnet wurden. Insbesondere wurden lasergetriebene Plasmawellen aufgrund der ultrakurzen Probepulsdauer aufgelöst. Ein Teil des Probestrahls wurde aufgespalten, um ein Nomarski-Interferometer zu beleuchten, was eine unabhängige Messung der durchschnittlichen Plasmadichte mit der Abel-Inversion ermöglicht. Eine systematische Messung der Plasmawellenlänge bei unterschiedlichen Dichten oder Laserintensitäten zeigte, dass das derzeitige Verständnis der Skalierung von nichtlinearen Plasmawellenlänge unzureichend ist. Basierend auf einer Reihe von Particle-in-Cell Simulationen wurde eine empirische Skalierung vorgeschlagen, die die nichtlineare Plasmawellenlänge nicht nur

mit der Spitzenstärke des Treiblasers, sondern auch mit seinem Aspektverhältnis von Punktgröße zu Pulslänge in Beziehung setzt. Es wurde eine hervorragende Übereinstimmung zwischen der Messung und dem neuen Skalierungsgesetz festgestellt.

Abstract

LWFA is the abbreviation of Laser WakeField Acceleration (or Accelerator), which is an emerging technology promising a drastic reduction of particle accelerators' size and cost. LWFA relies on the large (\sim GV/cm) electric field in the plasma wave excited by laser pulses with a relativistic peak intensity in excess of 10^{18} W/cm². During the course of this thesis work, diagnostic tools, for electrons and for the plasma medium, specially adapted to the conditions of LWFA research were developed for the ATLAS-300 Ti:sapphire laser at the Laboratory for Extreme (LEX) Photonics at Ludwig-Maximilians-Universität München (LMU). For electron diagnostics, the implementation and characterization of scintillating screens and permanent dipole magnets were carried out. On the plasma diagnostics side, a few-cycle probe beam for producing fs-snapshots of the plasma wave was developed.

Specifically, the light-emitting efficiency of nine commonly used scintillating screen types were calibrated with electron beams from the ELBE Linac at Helmholtz Zentrum Dresden Rossendorf. Existing methods for transferring the absolute calibration results into cross-calibration with a constant light source were improved upon. Regarding the dipole magnet, the B -field distribution near the gap central plane was measured with a Hall sensor and electron tracking was performed in General Particle Tracer using the measured field map. Scintillating screens and the dipole magnet comprised the electron spectrometer, allowing for energy-resolved detection of electron beams generated in the LWFA. Self-injected electron beams with several hundreds pC of charge and peak energy above 1 GeV were accelerated in a hydrogen-filled varying-length gas cell. Injecting with shock fronts in supersonic gas jets, stable electron beams with spectral density beyond 10 pC/MeV was achieved thanks to a percent-level energy spread.

The highlight of this work is the construction and application of a hollow-core fiber based pulse compression setup, serving as the probe beam during the experiments. This setup delivered sub-10 fs probe pulses, with which, shadowgraphic snapshots of the laser plasma interaction were recorded. In particular, laser-driven plasma waves were resolved owing to the ultrashort probe pulse duration. A portion of the probe beam was split out to illuminate a Nomarski interferometer, enabling independent measurement of the average plasma density with Abel inversion technique. A systematic measurement of plasma wavelength at varying densities or laser intensities revealed insufficiency of the current understanding of nonlinear plasma wavelength scaling. An empirical scaling was proposed based on a set particle-in-cell simulations, which relates the nonlinear plasma wavelength not only to the drive laser's peak strength, but also to its spot-size-to-pulse-length aspect ratio. Excellent agreement was found between the measurement and the new scaling law.

Contents

Zusammenfassung	i
Abstract	iii
1 Introduction	1
2 Basic laser-matter interaction	5
2.1 Description of laser pulse	5
2.1.1 Gaussian pulse	6
2.1.2 Gaussian beam	8
2.2 Electron motion in laser pulse	9
2.2.1 Plane wave - non-relativistic regime	10
2.2.2 Plane wave - relativistic regime	10
2.2.3 Realistic laser pulse	13
2.3 Practical considerations	14
2.4 Strong-field ionization	14
2.5 Definition of plasma	17
2.6 Laser propagation in plasma	17
2.6.1 Optical guiding in plasma	18
3 Laser wakefield acceleration	21
3.1 Wakefield equations	21
3.1.1 Linear wakefield	25
3.1.2 Nonlinear wakefield	26

Contents

3.1.3	Bubble formation	28
3.2	Electron trapping in wakefield	30
3.3	Wave breaking and self-injection	32
3.3.1	2D wave breaking in cylindrical symmetry	33
3.4	Controlled injection schemes	35
3.4.1	Density down-ramp injection	35
3.4.2	Ionization injection	37
3.4.3	Colliding pulse injection	38
3.5	Acceleration limits and scalings	40
3.6	Experimental arrangement	42
3.6.1	Supersonic gas jet with shockfront injector	42
3.7	ATLAS-300 laser system	44
3.8	LWFA experiment with variable-length gas cell	46
4	Basic Diagnostics	49
4.1	Scintillating screen	49
4.1.1	Absolute calibration of scintillating screens	50
4.1.2	Cross-calibration with constant light source	53
4.1.3	Pointing screen in LEX photonics	55
4.2	Magnetic spectrometer	56
4.2.1	Electron tracking	58
4.2.2	Magnet focusing	59
4.3	Interferometry	60
4.3.1	Nomarski interferometer	60
4.3.2	Phase retrieval	62
4.3.3	Abel Inversion	62
5	Few-cycle shadowgraphy	64
5.1	Few-cycle probe setup	64

Contents

5.2	Shadowgraphic observation of linear and nonlinear plasma waves	66
5.3	Nonlinear plasma wavelength scaling	68
5.4	Plasma wave evolution in density up-ramp	73
5.5	Phase reconstruction and wave amplitude	74
5.6	Plasma wave gallery	75
5.6.1	Plasma waves driven by LWFA electron bunches	75
5.6.2	Fully broken bubble after shock front injection	76
5.6.3	Bubble shape change in colliding pulse injection	77
5.6.4	Off-center plasma wave	78
6	Summary and outlook	79
	List of figures	81
	List of tables	83
	Acknowledgement	95

1 Introduction

Particle accelerators have been revolutionizing how mankind perceives the world. Scientists use particles, or secondary radiations derived from accelerators to study the structure and interaction of matter in the hope of unveiling the laws of the nature—the discovery of subatomic particles such as electrons and quarks to name an example. Most recently, collisions of the 7 TeV (center-of-mass) proton beams produced with the Large Hadron Collider (LHC) confirmed the long-standing hypothesis of the Higgs boson—an essential puzzle piece in explaining how mass arises for other fundamental particles in the Standard Model of particle physics [1–3]. Outside the field of fundamental research, clinicians use accelerator-based sources for diagnosing diseases or treating tumors, aiming for improving human living condition. Radiography techniques such as Xray CT have become a routine in modern hospitals. Medical accelerators producing heavy ions with several hundred MeV/u of energy have been successfully used for radiotherapy. The societal benefits of particle accelerators do not end there, one finds myriad industrial applications too [4]. Huge market exists for accelerator-based material processing and treatment, e.g., ion implantation of semiconductor, precision e-beam machining. Neutron source off-sprang from accelerators are widely used for the exploration of natural resources such as gas and oil, as well as for security applications like nondestructive examination of nuclear waste and search for concealed explosives.

Currently, particle accelerators rely mostly on metal cavities operating in the radio frequency (RF) range of a few gigahertz. When a charged particle e.g. a proton or an electron propagates through these RF cavities, the alternating field is effectively rectified in the particle's rest frame so that it can be accelerated to high energies. Particle accelerators are built in the format of either a ring or a straight line. The largest circular accelerator ever built to date is the located at CERN near Geneva—the Large Hadron Collider (LHC) for protons, and the Large Electron–Positron Collider (LEP) for leptons, respectively. The LEP was built in a tunnel with a circumference of 27 km, where electrons collide with positrons at a beam energy of 209 GeV. After the LEP's operation stopped and the machine dismantled in 2000, the same tunnel became the host of the LHC, where two counter-propagating proton beams can be accelerated to 6.5 TeV, i.e., 13 TeV center-of-mass collision energy. In contrast, the Stanford Linear Accelerator at SLAC National Accelerator Laboratory is, as its name suggests, a linear machine for electrons/positrons with beam energy up to 50 GeV achieved in a 2-mile-long tunnel, largest in its kind.

The huge size and hence enormous (construction and operation) cost of these accelerators make it almost economically prohibitive for even larger machines, which also makes the access to these facilities rather restricted. The main reason for that lies in the maximum acceleration gradient achievable with RF technologies, which is limited to ~ 100 MV/m

due to cavity material breakdown. Clearly, novel approaches to increase the acceleration gradient are desired, enabling next-generation energy-frontier accelerators on the one hand, proliferating the currently state-of-the-art machines on the other hand. A promising route is to leverage the rapid development of ultra-fast lasers, as the highest controllable field strength known to mankind is in the focus of a laser pulse. Switching from RF waves to near infrared (NIR) lasers, advanced micro-cavity designs with dielectrics instead of metals have achieved higher fields of up to ~ 250 MV/m [5], albeit only in structures of millimeter-scale so far and the scalability is yet to be demonstrated.

When propagating a high-power laser pulse in a dilute plasma, the laser pulse's ponderomotive force expels the plasma electrons from high-intensity regions and leaves an ion excess in its wake. The electrostatic force of these ions acts as the restoring force and sets up a collective electron oscillation. Thus a density modulation co-propagating with the drive pulse i.e. the plasma wave is formed. The electric field of this wakefield can be huge. For example, a plasma with an average density of 10^{18} cm $^{-3}$ can sustain a field on the order of 100 GV/m, three orders of magnitude higher than possible in RF cavities.

Tajima and Dawson [6] first proposed the idea of harnessing this large plasma field to build accelerators four decades ago. However, it was not until the advent of chirped pulse amplification (CPA) pioneered by Strickland and Mourou [7] that laser plasma accelerators (LPAs) were experimentally demonstrated. LPA experiments prior to 2004 [8] achieved acceleration gradients over 100 GV/m, electron energy beyond 100 MeV, and nC-level charge, although most of the spectral component was contained in the low energy (below 10 MeV) part of the exponentially distributed energy spectrum and only the long tail extends out to above 100 MeV, making these beams unfit for many applications demanding monoenergetic source with percent-level energy spread. On the theory front, contemporaneously, numerical methods, particle-in-cell (PIC) codes in particular, to simulate laser-plasma interactions witnessed a rapid improvement. The ever-growing computing power and the ever-shorter laser pulse duration, hence a reduced interaction volume, enabled fully three-dimensional simulations of the laser wakefield acceleration (LWFA) process. PIC simulations illuminated LWFA physics with fine details and identified the bubble regime [9], in which quasi-monoenergetic electron bunches can be accelerated. This was demonstrated in 2004 when three independent groups reported the production of high-quality electron bunches with ~ 100 MeV peak energy, ~ 100 pC of charge, a few percent of energy spread, and a few milliradians of divergence, marking the beginning of a new era of LWFA research. Ever since, LWFAs have reached multi-GeV beam energies [10–12]; controlled injection schemes have drastically increased their stability and tunability [13–25]; several types of LWFA-based compact X-ray sources have achieved competitive peak brightness compared with RF-based infrastructures [26–28]. Furthermore, these sources have demonstrated their application potential in imaging [29, 30], high energy density physics [31, 32], and tumor treatment [33].

While the field of wakefield acceleration is developing at a fast pace, some basic questions remain not fully answered. In particular, though theories on the formation of plasma wave trains have been studied extensively for the one-dimensional case, their predicting power in a real experiment is often limited due to higher dimensional effects. Studies addressing 3D plasma wave formation date back decades and remain mostly qualitative [34] or phenomenological [35]. Lu et al. [36, 37] established a quantitative model to correlate plasma bubble

size with the laser peak intensity based on a force balance argument, which, however, is only valid in the bubble regime and does not discuss trailing periods of plasma oscillations.

Due to the restrictions of analytical models, interpretation of experimental results usually resorts to numerical simulations. With the recent development of fast particle-in-cell codes such as CALDER-CIRC [38] and FBPIC [39], quasi-3D simulations can be performed in a short period of time, thus enabling systematic parameter scans.

It is often cited in the accelerator community that an accelerator is only as good as its diagnostics. New diagnostics especially design for LPAs such as few-cycle shadowgraphy uniquely combine femtosecond resolution with picosecond observation windows [40–43]. As established models predict a clear relation between the plasma wavelength and the laser peak potential, this method potentially provides a novel non-invasive diagnostic for the laser evolution. Pioneering work of Sävert et al. [40] has demonstrated the lengthening of the plasma bubble [9] and provided important information about the electron injection process.

A considerable portion of the work underlying this thesis was devoted to the commissioning of a new infrastructure, the Laboratory for Extreme (LEX) Photonics, where researches on laser plasma acceleration of electrons and ions were carried out. The Ti:sapphire laser system ATLAS-300 is the backbone of this new lab. With ATLAS-300, GeV-class electron bunches with hundreds of pC charge were accelerated from self-injection in a gas cell target. High-quality electron bunches with unprecedented spectral charge density (> 10 pC/MeV) were achieved with controlled injection, leading to the demonstration of fast betatron X-ray phase contrast tomography [30], the first direct observation of plasma waves and ion motion driven by LWFA bunches [42], and new insights into beam-loading effects [44]. All these successes are supported by accurate quantitative knowledge of the electron beam properties, for which, electron diagnostics, a magnetic spectrometer with absolutely calibrated energy and charge axes in particular, are indispensable. Characterization of electron diagnostics forms the first pillar of this thesis.

The other pillar of this thesis is the commissioning and implementation of a few-cycle probe beam, adapted from that described in the dissertation by Sävert [45] to suit the experimental conditions at ATLAS-300. This few-cycle probe beam enabled shadowgraphic snapshots of plasma waves, driven either by the laser directly [43], or by the electron beams from the LWFA stage powered by ATLAS-300 [42]. Combining few-cycle shadowgraphy with independent density measurement from Nomarski-type interferometry allowed the interrogation of the scaling laws for the non-linear plasma wavelength in a practical regime, and it was found, contrary to the common belief in the community, that the laser peak strength alone is not sufficient to scale the nonlinear plasma wavelength. FBPIC [39] simulations of laser propagation in a plasma closely resembling the experiments reveal that the transverse motion of electrons play an important role in the plasma wave driven by a tightly focused laser whose spot size is comparable to its pulse length. A set of CALDER-CIRC [38] simulations inspired a new empirical scaling involving the peak laser strength and the spot aspect ratio, which showed excellent agreement with the measurement.

The remainder of the thesis is structured as follows:

Chapter 2 starts by laying the theory foundation of high-intensity laser-plasma interaction,

including the fundamental description of a laser pulse, the motion of a single electron in electro-magnetic fields, and basics properties of plasmas.

Chapter 3 gives a general description of laser wakefield acceleration. Plasma dynamics is discussed its simplest form with emphasis on plasma wave formation. Electron injection and acceleration is presented with both mathematical equations and experimental data.

Chapter 4 describes the basic diagnostic tools developed during the course of this thesis work.

Chapter 5 presents the setup and the results obtained with the few-cycle probe beam.

Finally, Chapter 6 summarizes the thesis work and gives prospects.

2 Basic laser-matter interaction

Physics of laser wakefield acceleration (LWFA) involves the understanding of high-intensity laser pulses as well as their interaction with a plasma. To tackle this rather complex problem, the individual building blocks will be examined first and then put together. The discussion of this chapter starts with properties of a laser pulse and the motion of a single electron.

2.1 Description of laser pulse

An intense laser pulse is in essence an electromagnetic (EM) wave, namely, an oscillation of electric field $\mathbf{E}(\mathbf{r}, t)$ and magnetic field $\mathbf{B}(\mathbf{r}, t)$ in space \mathbf{r} and time t . The bold fonts here represent vectors and the explicit function dependence (\mathbf{r}, t) will be dropped hereinafter for brevity. In general, the dynamics of EM fields is governed by Maxwell's equations [46]:

$$\begin{aligned}\nabla \cdot \mathbf{E} &= \frac{\rho}{\varepsilon_0} & \nabla \times \mathbf{E} &= -\frac{\partial \mathbf{B}}{\partial t} \\ \nabla \cdot \mathbf{B} &= 0 & \nabla \times \mathbf{B} &= \frac{1}{c^2} \frac{\partial \mathbf{E}}{\partial t} + \mu_0 \mathbf{j},\end{aligned}\tag{2.1}$$

where ρ and \mathbf{j} denote the electric charge and current density, ε_0 and μ_0 the vacuum permittivity and permeability, and $c = 1/\sqrt{\mu_0\varepsilon_0}$ the speed of light, respectively.

An EM wave carries an energy flow. The rate of energy transfer through a unit area, corresponding to a laser pulse's intensity I_L in practical terms, can be calculated as the time average of the Poynting vector $\langle \mathbf{S} \rangle$. In free space,

$$I_L = \langle \mathbf{S} \rangle = \frac{1}{\mu_0} \langle \mathbf{E} \times \mathbf{B} \rangle = \varepsilon_0 c \langle \mathbf{E}^2 \rangle.\tag{2.2}$$

Later in this work EM fields are often expressed by a four-potential $A^\mu = (\phi/c, \mathbf{A})$. The relation between the fields and the four-potential is given as

$$\begin{aligned}\mathbf{E} &= -\nabla\phi - \frac{\partial \mathbf{A}}{\partial t} \\ \mathbf{B} &= \nabla \times \mathbf{A},\end{aligned}\tag{2.3}$$

with ϕ being the electric scalar potential, and \mathbf{A} the magnetic vector potential.

Employing the definition above, the Lorenz gauge condition $\partial_\mu \mathbf{A}^\mu = 0$,ⁱ and the vector identity $\nabla \times \nabla \times \mathbf{A} = \nabla(\nabla \cdot \mathbf{A}) - \nabla^2 \mathbf{A}$, Maxwell's equations simplify to a wave equation

$$\left(\frac{1}{c^2} \frac{\partial^2}{\partial t^2} - \nabla^2 \right) A^\mu = \mu_0 J^\mu, \quad (2.4)$$

with a four-current $J^\mu = (c\rho, \mathbf{j})$ as the source term. In absence of J^μ , e.g. in vacuum, the wave equation admits harmonic plane wave solutions

$$A^\mu = A_0^\mu \exp(i\mathbf{k}_L \cdot \mathbf{r} - i\omega_L t), \quad A_0^\mu \in \mathbb{C} \quad (2.5)$$

observing the dispersion relation $|\mathbf{k}_L| = \omega_L/c$. \mathbf{k}_L denotes the wave vector, and ω_L the angular frequency of the carrier. The complex-valued amplitude $A_0^\mu = |A_0^\mu| \exp(i\Phi^\mu)$ incorporates the phase Φ^μ of the oscillation. Here A^μ is an analytical representation [47] consisting of the real-valued physical potential and its Hilbert transform—convolution with $1/(\pi t)$. Discarding the imaginary part of the analytical representation recovers the physical potential.

A plane wave with a constant amplitude everywhere in space and time is just an idealized model. It does not directly represent a real laser pulse, whose spatial-temporal extents are finite. However, any laser pulse can be described as a linear superposition of plane waves with various frequencies and wave vectors given a fixed phase relationship (detailed below) owing to the completeness of the basis $\{\exp(i\mathbf{k}\mathbf{r}), \exp(i\omega t)\}_{\omega \in \mathbb{R}}$. The linearity of the wave equation further warrants that such a superposition remains a solution to the equation. Importantly, it follows from the definition in Eq. (2.3) and the dispersion relation that the amplitude of the E -field is a factor of c larger than the B -field. Hence the electron motion in a laser pulse (detailed in section 2.2) will be dominated by the E -field in the non-relativistic regime, and only in the relativistic regime does the B -field play an important role.

2.1.1 Gaussian pulse

Let $\tilde{A}(\omega) \in \mathbb{C}$, the spectrum of a linearly polarized laser pulse,ⁱⁱ be a Gaussian function with an amplitude of $\tilde{A}_0 \in \mathbb{R}$, a mean angular frequency of ω_L , a standard deviation of $\Omega/\sqrt{2}$, and a linear spectral phase $\tilde{\Phi}(\omega) = \kappa\omega + \Phi_0$, i.e.,

$$\tilde{A}(\omega) = \tilde{A}_0 \exp\left[-\frac{(\omega - \omega_L)^2}{\Omega^2}\right] \exp(i\kappa\omega + i\Phi_0). \quad (2.6)$$

An inverse Fourier transform of this spectrum yields

$$\begin{aligned} A(t) &= \int \frac{d\omega}{2\pi} \tilde{A}(\omega) \exp(-i\omega t) \\ &= A_0 \exp\left[-\frac{(t + \kappa)^2}{\tau^2}\right] \exp[-i\omega_L(t + \kappa)], \end{aligned} \quad (2.7)$$

ⁱrepeated index μ is summed over

ⁱⁱThis work uses linearly polarized laser pulses. They have only one significant field component hence can be expressed with a scalar notation.

2.1. Description of laser pulse

with respectively the complex-valued amplitude and the half-width at $1/e$ maximum of

$$A_0 = \tilde{A}_0 \frac{\Omega}{2\sqrt{\pi}} \exp(i\Phi_0), \quad \text{and} \quad \tau = \frac{2}{\Omega}. \quad (2.8)$$

Equation (2.7) is the analytical representation of a Gaussian pulse in the time domain. Apparently, a broader spectrum (larger Ω) can result in a shorter pulse (smaller τ), which is but a manifestation of the Heisenberg's uncertainty principle in the context of laser physics. However, a broad spectrum alone does not ensure a short pulse. The spectral phase plays also an important role. When the spectral phase is linear, as assumed for the calculation above, there will be an instant of time—depending on the phase's slope—where all frequency components of the spectrum interfere constructively and the resulted pulse duration is the shortest. Such a pulse is called transform-limited; cf. Fig. 2.1. On the contrary, a nonlinear spectral phase distorts the pulse—increasing the pulse duration and thereby reducing the pulse's peak power. A pulse with nonlinear phases is called chirped. Chirping the pulse in a controlled manner allows laser pulses to be amplified to high energies, e.g. ~ 5 J before compression for the experiments presented in this work, without damaging the optics. This technique of chirped pulse amplification (CPA) [7] was awarded the Nobel prize in Physics in 2018; cf. Sec. 3.7. Discussions above also constitutes the basic guideline for few-cycle pulse generation, enabling the results on few-cycle shadowgraphy presented in chapter 5; cf. Refs. [43, 45].

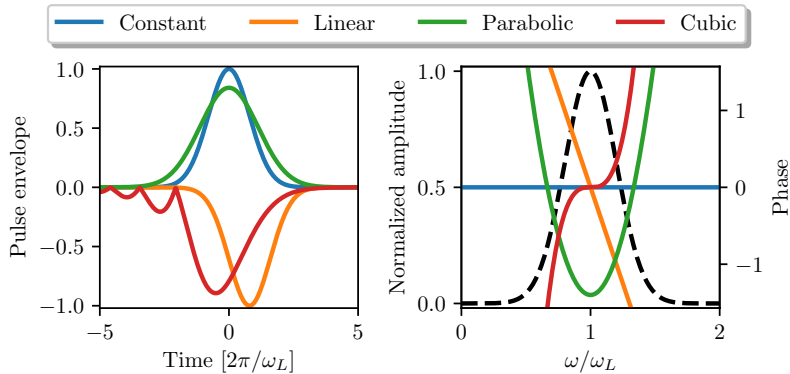


Figure 2.1: Time- (left) and spectral domain (right) representation of laser pulses with identical spectral amplitude and various orders of spectral phase; in the left panel pulses with odd-ordered phase are flipped vertically for better legibility. A constant phase results in a transform-limited centered at $t = 0$; a linear phase shifts the pulse; a parabolic phase broadens the pulse; a cubic phase adds an asymmetry to the pulse.

The product of the temporal duration and spectral width—both in the sense of full width at half maximum (FWHM) of the intensity envelope—is known as the time-bandwidth product. For a transform-limited Gaussian pulse

$$\Delta t_{\text{FWHM}} \cdot \frac{\Delta \omega_{\text{FWHM}}}{2\pi} \approx 0.441. \quad (2.9)$$

The discussion above did not involve the spatial dependence for simplicity. The spatial decomposition is an analogy of the temporal one, that is, a laser beam with finite extent in

space can be decomposed into plane waves with different wave vectors (directions). In the next subsection, the properties of a Gaussian beam will be discussed.

2.1.2 Gaussian beam

A Gaussian beam is of special interest because a) it is often the fundamental transversal mode of a laser resonator or (approximately) of a hollow-core fiber (Sec. 5.1), and b) it is simple enough to be handled analytically in paraxial approximation [48]. Employing the (complex) analytic representation,

$$A(r, z) = A_0 \frac{w_0}{w(z)} \exp\left[-\frac{r^2}{w^2(z)}\right] \exp\left[ik_L \frac{r^2}{R(z)}\right] \exp[ik_L z - i\psi(z)] \quad (2.10)$$

describes a Gaussian beam propagating to the z -direction with the focus at $z = 0$. The radial coordinate r measures the distance to the beam axis. Axial symmetry (hence the coordinate r) and flat phase (see discussion below) in the focus are assumed for simplicity.

$$w(z) = w_0 \sqrt{1 + \frac{z^2}{z_R^2}} \quad (2.11)$$

denotes the beam size at position z , where

$$z_R = \frac{\pi w_0^2}{\lambda_L} \quad (2.12)$$

is the Rayleigh range—the distance from the focus at which the beam area doubles. The wave number k_L and wavelength λ_L are related via $\lambda_L = 2\pi/k_L$.

$$w_0 = w(0) = \frac{\lambda_L}{\pi} \frac{1}{\tan \theta} \quad (2.13)$$

is the beam waist (radius), and

$$\theta = \lim_{z \rightarrow \infty} \arctan \frac{w(z)}{z} \approx \frac{w_0}{z_R} \quad (2.14)$$

is the asymptotic (half) divergence of the beam. The wavefront's radius of curvature

$$R(z) = z + \frac{z_R^2}{z} \quad (2.15)$$

has minima of $\pm 2z_R$ at $z = \pm z_R$. A flat wavefront, i.e. $R(z) \rightarrow \infty$, can be obtained either in the focus, $z \rightarrow 0$, or in the far-field, $z \rightarrow \infty$. A Gaussian beam acquires a phase of $k_L z - \psi(z)$ over a propagation of z , less than that of a plane wave with the same carrier frequency propagating over the same distance, $k_L z$. This r -independent phase shift is known as the Gouy phase [49]

$$\psi(z) = \arctan\left(\frac{z}{z_R}\right). \quad (2.16)$$

2.2 Electron motion in laser pulse

Inside an EM field, the motion of a relativistic electron with rest mass m_e , charge $-e$, and velocity \mathbf{v} can be generally characterized by the Lagrangian [46]

$$L = -m_e c^2 \sqrt{1 - |\mathbf{v}|^2 / c^2} - e(\mathbf{v} \cdot \mathbf{A} - \phi). \quad (2.17)$$

The Euler-Lagrange equation $d_t \partial_{\dot{\mathbf{r}}} L = \partial_{\mathbf{r}} L$ then reads

$$\frac{d}{dt}(\mathbf{p} - e\mathbf{A}) = -e\nabla(\mathbf{v} \cdot \mathbf{A} - \phi), \quad (2.18)$$

which states that the temporal variation of the canonical momentum $\mathbf{p} - e\mathbf{A}$ is given by the gradient of a generalized potential $-e(\mathbf{v} \cdot \mathbf{A} - \phi)$. Here $\mathbf{p} = \gamma m_e \mathbf{v}$ denotes the momentum, $\gamma = 1/\sqrt{1 - \beta^2}$ the Lorentz factor, and $\beta = |\mathbf{v}|/c$ the speed normalized to the speed of light.

Using the chain rule $d/dt = \partial/\partial t + (\mathbf{v} \cdot \nabla)$ for a particle moving in a field, the vector identity $\mathbf{v} \times \nabla \times \mathbf{A} = \nabla(\mathbf{v} \cdot \mathbf{A}) - (\mathbf{v} \cdot \nabla)\mathbf{A}$, and the definition of vector potential \mathbf{A} in Eq. (2.3), the Euler-Lagrange equation above reveals itself as the Lorentz force equation:

$$\frac{d\mathbf{p}}{dt} = -e(\mathbf{E} + \mathbf{v} \times \mathbf{B}). \quad (2.19)$$

Let this single electron be an element of a fluid, another interpretation of the Euler-Lagrange equation can be obtained by considering the vector identity $\nabla(\mathbf{p} \cdot \mathbf{p}) = 2[(\mathbf{p} \cdot \nabla)\mathbf{p} + \mathbf{p} \times (\nabla \times \mathbf{p})]$, which, upon division by $2\gamma m_e$ and rearrangement [50], yields

$$(\mathbf{v} \cdot \nabla)\mathbf{p} = \frac{1}{2\gamma m_e} \nabla |\mathbf{p}|^2 - \mathbf{v} \times (\nabla \times \mathbf{p}). \quad (2.20)$$

Using the relation above to split the total time derivative in Eq. (2.18) and taking into account $\gamma = \sqrt{1 + (|\mathbf{p}|^2/m_e c)^2}$, the partial derivatives of the canonical momentum fulfill

$$\left(\frac{\partial}{\partial t} - \mathbf{v} \times \nabla \times\right)(\mathbf{p} - e\mathbf{A}) = -\nabla(\gamma m_e c^2 - e\phi). \quad (2.21)$$

Since the right hand side of this equation is a gradient, its curl vanishes. Hence taking curl on both sides of Eq. (2.21) results in the vorticity equation

$$\left(\frac{\partial}{\partial t} - \nabla \times \mathbf{v} \times\right)[\nabla \times (\mathbf{p} - e\mathbf{A})] = 0, \quad (2.22)$$

which implies $\nabla \times (\mathbf{p} - e\mathbf{A}) = 0$ for any time t , if $\nabla \times (\mathbf{p} - e\mathbf{A})|_{t < 0} = 0$, e.g., when the electron fluid is at rest before laser's arrival [51]. Hence the momentum equation (2.21) becomes

$$\frac{\partial}{\partial t}(\mathbf{p} - e\mathbf{A}) = -\nabla(\gamma m_e c^2 - e\phi). \quad (2.23)$$

This equation will serve as the starting point to derive plasma wave dynamics later in the next chapter.

2.2.1 Plane wave - non-relativistic regime

The Lorentz equation (2.19) can be easily integrated for the non-relativistic motion in a plane wave propagating in vacuum, i.e. $\gamma \rightarrow 1$, $\beta \rightarrow 0$, $\phi = 0$, and $\mathbf{A} = \mathbf{A}_0 \sin(\mathbf{k}_L \cdot \mathbf{r} - \omega_L t)$. In this case, $\mathbf{p} = m_e \mathbf{v}$ and the $\mathbf{v} \times \mathbf{B}$ term can be neglected due to $B = E/c$ [52]. Using again the chain rule $d/dt = \partial/\partial t + (\mathbf{v} \cdot \nabla)$, Eq. (2.19) becomes

$$\frac{d}{dt}(\mathbf{p} - e\mathbf{A}) = -e(\mathbf{v} \cdot \nabla)\mathbf{A}. \quad (2.24)$$

Since $(\mathbf{v} \cdot \nabla)\mathbf{A} = v_{\parallel} k_L \mathbf{A}_0 \cos(\mathbf{k}_L \cdot \mathbf{r} - \omega_L t)$, v_{\parallel} being the velocity component parallel to the wave vector \mathbf{k}_L , is on the order of $\mathcal{O}(v_{\parallel}/c)$ due to the dispersion relation $|\mathbf{k}_L| = \omega_L/c$, the right hand side of the equation above can be neglected for a non-relativistic electron. Hence

$$\mathbf{p} - e\mathbf{A} = \text{const.} \quad (2.25)$$

For an electron initially at rest, the integration constant above is zero; the quiver velocity is simply $\mathbf{v} = e\mathbf{A}/m_e$ and the quiver motion is purely transverse. Averaging the quiver energy $m_e |\mathbf{v}|^2 / 2$ over one period of the fast oscillation yields the ponderomotive potential [53]

$$U_p = \frac{e^2 A_0^2}{4m_e}. \quad (2.26)$$

If the field is not a simple plane wave with a constant amplitude, the gradient of the ponderomotive potential exerts a force on a test charge and pushes it to lower intensity regions. As will be shown in later chapters, this ponderomotive force can drive large amplitude plasma waves in which particles can be trapped and accelerated to relativistic energies.

The maximal quiver velocity can also be readily obtained as $v_{\text{max}} = eA_0/m_e$. Equating v_{max} to the vacuum speed of light yields $A_0 = m_e c/e$, that is, an electron were to reach the speed of light when quivering in the field with an amplitude of $m_e c/e$, contradicting the non-relativistic assumption. Hence when the normalized vector potential defined as

$$a_0 = \frac{eA_0}{m_e c}, \quad (2.27)$$

approaches unity, relativistic treatment must be applied and the $\mathbf{v} \times \mathbf{B}$ term taken in account.

2.2.2 Plane wave - relativistic regime

In the relativistic regime, the electron motion is more complex. Two constants of motion stemming from symmetries of plane waves can be utilized to ease the understanding [54, 55]:

1. the potential is translation-invariant in the transverse direction, $r_{\perp} \rightarrow r_{\perp} + \Delta r$;
2. the potential is only a function of $t - r_{\parallel}/c$, be r_{\parallel} the propagation distance.

From 1, it follows that the canonical momentum's transverse components conserve, i.e.,

$$\mathbf{p}_\perp - e\mathbf{A}_\perp = C_1. \quad (2.28)$$

Hereafter C_1 will be referred to as the first constant of motion. For an electron initially at rest, $C_1 = 0$. Likewise, it follows from 2,ⁱⁱⁱ

$$\mathbf{p}_\parallel - \frac{\mathcal{E}_{kin}}{c} = C_2, \quad (2.29)$$

where $\mathcal{E}_{kin} = (\gamma - 1)m_e c^2$ denotes the kinetic energy, and \mathbf{p}_\parallel the parallel component of the kinetic momentum. The second constant of motion, C_2 , vanishes as well if the electron has no motion at the beginning. A heuristic way to understand the second constant of motion is that the kinetic energy gain of an electron in the EM field is related to its longitudinal momentum increment via the photon dispersion relation, $k_L = \omega_L/c$, which is a consequence of a plane wave carrying no net transverse momentum.

The relation between the longitudinal and transverse momenta can thus be found, for an initially stationary electron, through the definition of the Lorentz factor $\gamma = \sqrt{1 + \tilde{p}_\perp^2 + \tilde{p}_\parallel^2}$, with $\tilde{p}_{\perp,\parallel} = p_{\perp,\parallel}/m_e c$ denoting the normalized momenta, as

$$\tilde{p}_\parallel = \frac{\tilde{p}_\perp^2}{2}, \quad (2.30)$$

alongside the relation between γ and a :

$$\gamma = 1 + \frac{a^2}{2}. \quad (2.31)$$

The quadratic relation in Eq. (2.30) implies that the electron motion will be dominated by the transverse component in the non-relativistic regime, $\tilde{p}_\perp \rightarrow 0$, whereas in the highly relativistic regime, $\tilde{p}_\perp \gg 1$, the longitudinal motion becomes dominant.

Thus the y - and z -component of the equation of motion, in a laser pulse $a = \hat{\mathbf{y}}a_0 \sin(k_L z - \omega_L t)$, read

$$\tilde{p}_y = \frac{\gamma}{c} \frac{dy}{dt} = a \quad (2.32)$$

$$\tilde{p}_z = \frac{\gamma}{c} \frac{dz}{dt} = \frac{a^2}{2}. \quad (2.33)$$

Introducing the retarded time $\tau = t - z/c$ such that $k_L z - \omega_L t = -\omega_L \tau$ and $\gamma \frac{d}{dt} = \frac{d}{d\tau}$,^{iv} the equations above can be easily integrated to yield

$$y(\tau) = \frac{a_0 c}{\omega_L} [\cos(\omega_L \tau) - 1] \quad (2.34)$$

$$z(\tau) = \frac{a_0^2 c}{4} \left[\tau - \frac{1}{2\omega_L} \sin(2\omega_L \tau) \right]. \quad (2.35)$$

ⁱⁱⁱThe direct consequence of 2 is $\mathbf{p}_\parallel - \mathcal{E}_{total}/c = C_2^*$. Subtracting both sides by $m_e c^2$ yields Eq. (2.29)

^{iv} $\gamma \frac{d}{dt} = \gamma \frac{d\tau}{dt} \frac{d}{d\tau} = (\gamma - \frac{\gamma}{c} \frac{dz}{dt}) \frac{d}{d\tau} = \frac{d}{d\tau}$, cf. Eqs. (2.31) and (2.33).

At first glance, Eq. (2.34) represents a transverse oscillation at the laser frequency ω_L , and Eq. (2.35) a longitudinal drift (due to the $a_0^2 c \tau / 4$ term) superimposed with an oscillation at $2\omega_L$. In fact, however, they contain *all* orders of nonlinear motion because τ is a function of z [56]; cf. the middle panel of Fig. 2.2. This becomes evident when the phase slippage between the laser and the electron is examined. Solving the drift term $a_0^2 c \tau / 4$ for t results in a drift velocity of

$$v_{\text{drift}} = \left\langle \frac{z}{t} \right\rangle = \frac{a_0^2}{4 + a_0^2} c \quad (2.36)$$

along the laser propagation direction, which effectively reduces the phase slippage angular frequency to^v

$$\omega = \frac{4}{4 + a_0^2} \omega_L. \quad (2.37)$$

As a result, the transverse oscillation becomes the nonlinear quiver with a period of $2\pi/\omega$, and the amplitude scales linearly with a_0 . In the longitudinal direction, oscillation period elongates to π/ω , and the amplitude scales with $a_0^2/(4 + a_0^2)$, which is almost a constant for $a_0 \gg 2$. In the average rest frame co-moving with the velocity v_{drift} , the electron trajectory appears as a figure-of-8; shown in the right panel of Fig. 2.2.

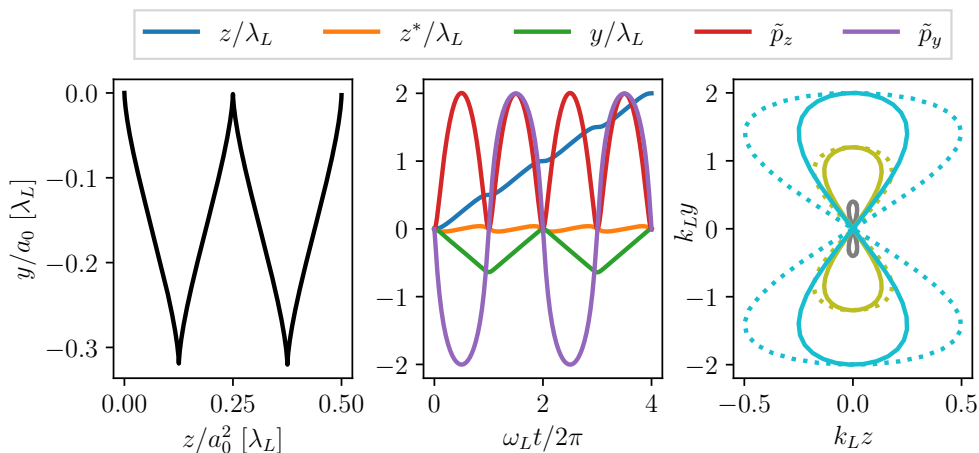


Figure 2.2: *Left:* Electron trajectory in a plane wave in the lab frame; λ_L denotes the laser wavelength. *Middle:* Evolution of dynamical variables for $a_0 = 2$; $z^* = z - v_{\text{drift}} t$ is the coordinate in the average rest frame. Note that the angular frequency is $\omega = \omega_L/2$ for the transverse oscillation and $2\omega = \omega_L$ for the longitudinal motion. *Right:* Electron trajectories for $a_0 \in [0.4, 1.2, 2.0]$ in the average rest frame; solid curves account for τ 's z -dependence hence the oscillation amplitude is reduced (see main text) whereas dotted curves are $y(\tau)$ v.s. $z(\tau) - a_0^2 c \tau / 4$; cf. Eqs. (2.34) and (2.35); k_L denotes the laser wavenumber; the center of figure-of-8 is deliberately shifted to the coordinate origin.

^vFor an electron moving at a velocity of $v_{\text{drift}} = a_0^2 c / (4 + a_0^2)$, it takes $t = \lambda_L / (c - v_{\text{drift}})$ for a laser pulse to outrun this electron by one wavelength of λ_L , corresponding to a phase slippage of 2π between the laser and the electron. The angular frequency of phase slippage is therefore $\omega = 2\pi/t = 4\omega_L / (4 + a_0^2)$.

2.2.3 Realistic laser pulse

Based on the knowledge of electron motion in a monochromatic plane wave, this section adds complexity to the model in two steps to make it closer to reality. In the first step, a Gaussian temporal envelope is considered while the pulse remains translation-invariant in the transverse direction, i.e., a plane wave pulse; in the second step, the spatial dependence is accounted for as a Gaussian beam with a finite-sized waist, i.e., a pulsed Gaussian beam. In either case, the peak value of the field is assumed sufficient to drive the electron motion to the relativistic regime. See section 2.1 for the definition of Gaussian pulses and beams.

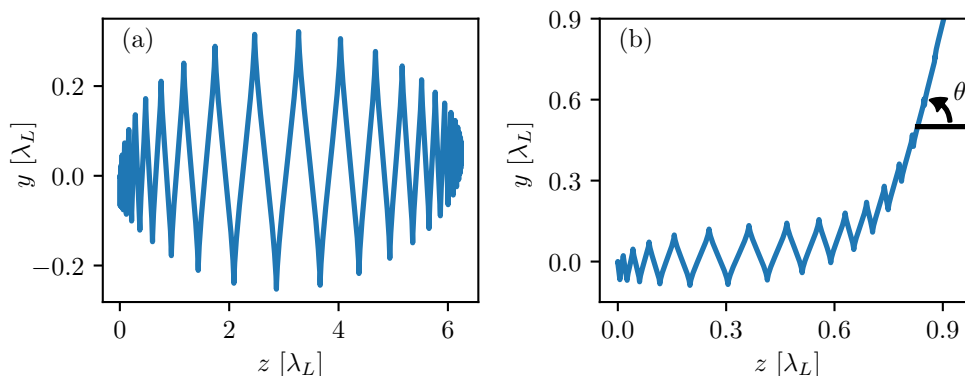


Figure 2.3: Electron trajectory in (a) a plane wave pulse and (b) a pulse focused to a spot with $w_0 = 0.6\lambda_L$. In both panels, $a_0 = 2.0$, and λ_L denotes the laser wavelength.

In a plane wave pulse, the electron motion starts as a pure transverse oscillation in the leading edge of the pulse. With the increase of field strength, the oscillation amplitude grows; the longitudinal oscillation and drift kick in near the peak of the pulse. As the pulse fades away, the electron motion gradually becomes a pure transverse oscillation again. After the laser pulse has passed, the electron will be merely displaced in space. No net energy transfer from the laser to the electron is achieved, because all the kinetic energy gain of the electron during the oscillation will be eventually given back to the laser field; cf. Fig. 2.3 (a). That sounds rather discouraging. In reality, however, the energy contained in the pulse is limited, meaning that the relativistic intensity can only be sustained over a small focal volume in space. For example, typical full width at half maximum (FWHM) focal spot size in this work is about $30\ \mu\text{m}$; correspondingly, the Rayleigh range is about $3\ \text{mm}$.

A pulsed Gaussian beam has its intensity peak in the center of the focal volume and the intensity decreases both longitudinally and transversely. In the rising edge of the pulse, the electron motion is similar to that in step one. Once the intensity peak overtakes the electron, however, the motion becomes different: an electron moving away from the axis will find itself in a lower intensity region, hence the reduced restoring force can not pull the electron back to the high intensity region any more; cf. Fig. 2.3 (b). Eventually, the electron will scatter out of the laser beam. Experimentally first observed by Moore et al. [57], the electron's scattering angle, θ , is related to the ratio of its transverse and longitudinal momenta as $\tan \theta = p_{\perp}/p_{\parallel}$. Particularly, for an electron initially at rest, $\theta = \arctan \sqrt{2/(\gamma - 1)}$.

Such a scattering effect is another way of interpreting the ponderomotive potential introduced

2.3. Practical considerations

in the previous section. As the electron motion becomes relativistic, the expression for the ponderomotive potential, Eq. (2.26), needs to be modified accordingly. Defining the potential again as the cycle-averaged kinetic energy, the formula can be given in terms of the Lorentz factor as

$$U_p = m_e c^2 (\gamma - 1). \quad (2.38)$$

The notation of a bare γ above already implies averaging over fast oscillations, which holds true hereinafter unless otherwise mentioned.

2.3 Practical considerations

The discussion so far is around quantities mostly beyond direct experimental access. To get a feeling for numbers, the aforementioned normalized vector potential is linked to a laser pulse via

$$a_0 = \sqrt{\frac{e^2 \lambda_L^2 I_0}{2\pi^2 \varepsilon_0 m_e^2 c^5}} \approx 0.85 \lambda_L [\mu\text{m}] \sqrt{I_0 [10^{18} \text{ W}/\text{c}^2\text{m}]}, \quad (2.39)$$

with λ_L denoting the wavelength and I_0 the peak intensity of the laser; e and m_e are electron's charge and mass; ε_0 and c are the permittivity and speed of light in vacuum, respectively. In terms of a_0 , the peak values of the EM fields and the laser intensity can be given as

$$\begin{aligned} E_0 &= \frac{2\pi m_e c^2}{e} \frac{a_0}{\lambda_L} && \approx \frac{a_0}{\lambda_L [\mu\text{m}]} \cdot 3.21 \times 10^{12} \text{ V m}^{-1} \\ B_0 &= \frac{2\pi m_e c}{e} \frac{a_0}{\lambda_L} && \approx \frac{a_0}{\lambda_L [\mu\text{m}]} \cdot 1.07 \times 10^4 \text{ T} \\ I_0 &= \frac{2\pi^2 \varepsilon_0 m_e^2 c^5}{e^2} \frac{a_0^2}{\lambda_L^2} && \approx \left(\frac{a_0}{\lambda_L [\mu\text{m}]}\right)^2 \cdot 1.37 \times 10^{18} \text{ W}/\text{c}^2\text{m}. \end{aligned} \quad (2.40)$$

In order to drive electron motion to the relativistic regime, which is required to form the plasma waves for electron acceleration (cf. Sec. 3.1), $a_0 \gtrsim 1$ is necessary, corresponding to an intensity in excess of $10^{18} \text{ W}/\text{c}^2\text{m}$ for laser systems operating at near infrared (NIR) wavelengths, $\lambda_L \sim 1 \mu\text{m}$. Such a high intensity is reached in this work by focusing laser pulses containing 2.5 J of energy within a duration of 30 fs FWHM to a spot with an FWHM size of 30 μm ; cf. section 3.7.

2.4 Strong-field ionization

The high intensity of a laser pulse means a very strong electric field. With a simple calculation it can be shown that the peak field strength of a laser pulse of a relativistic intensity is much higher than the field that binds the electron to the proton in a hydrogen atom. It follows immediately that such a laser pulse is capable of ionizing matter.

Schematically represented in figure 2.4, there are several mechanisms of strong-field ionization. In the intensity range of $10^{14} \text{ W}/\text{c}^2\text{m}$ to $10^{15} \text{ W}/\text{c}^2\text{m}$, multi-photon ionization (MPI;

panel a) and tunnel ionization (TI; panel b) play a major role. The Keldysh parameter [58, 59] defined as the square root of the ratio between the ionization potential U_{ion} and twice the ponderomotive potential U_p

$$\gamma_K = \sqrt{\frac{U_{\text{ion}}}{2U_p}} \quad (2.41)$$

can be used to distinguish these two ionization regimes. When $\gamma_K \gg 1$, MPI is the more accurate picture, whereas when $\gamma_K \ll 1$, TI gives a more appropriate description. However, for a laser pulse with a relativistic peak intensity ($> 10^{18} \text{ W/c}^2\text{m}$), the intensity values mentioned above only occur at the feet of the pulse. Instead, the most probable mechanism is the barrier-suppression ionization (BSI; panel c), which works as follow:

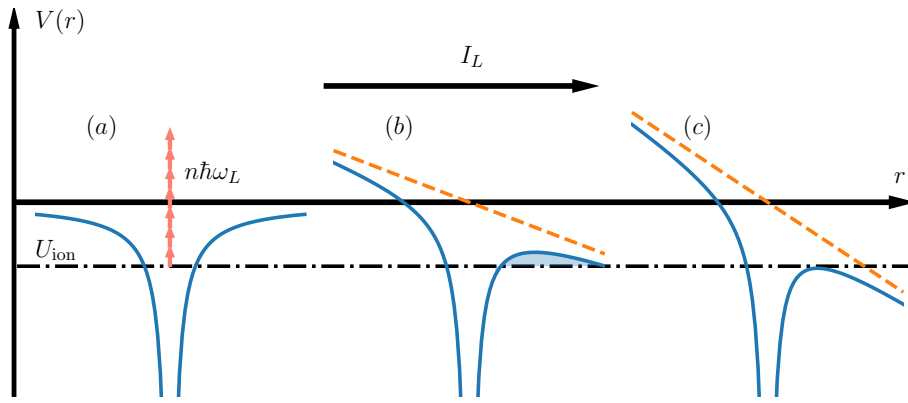


Figure 2.4: Strong field ionization of an atom or ion at various laser intensities. The blue line represents the spatial dependence of the combined Coulomb potential of the ion and the laser pulse; the dashed orange line represents the potential of the laser alone; each pink arrow represents a laser photon. As the laser intensity increases from $10^{14} \text{ W/c}^2\text{m}$ to $10^{15} \text{ W/c}^2\text{m}$ level, the dominant ionization mechanism evolves from (a) multi-photon ionization to (b) tunnel ionization, and the atomic potential starts to distort. The shaded area in (b) suggests that the electron has to tunnel through a potential barrier before ionization, in contrast to (c), where the barrier is fully suppressed at even higher intensities.

Since the wavelength of a laser pulse ($\sim \mu\text{m}$) is much larger than the size of an atom, its electric field E_L can be considered a constant in the vicinity of the atom. Hence the combined electric potential of an ion in the charge state $Z+$ in presence of the laser field can be written as

$$V(r) = -\frac{Ze^2}{4\pi\epsilon_0|r|} - eE_L r. \quad (2.42)$$

Z is the charge state after ionization, e.g. $Z = 1$ for hydrogen.

The critical field for the BSI can be estimated by equating this potential maximum with the ionization potential

$$V(r_0) = U_{\text{ion}}, \quad \text{with} \quad \left. \frac{dV(r)}{dr} \right|_{r=r_0} = 0. \quad (2.43)$$

The maximum appears at $r_0 = \sqrt{Ze/4\pi\epsilon_0 E_L}$ and the laser field strength can be solved as

$$E_L = \frac{\pi\epsilon_0 U_{\text{ion}}^2}{Ze^3}. \quad (2.44)$$

Once this critical field is reached, the electron becomes unbound instantaneously. Within a fast oscillation of the laser field, the potential barrier is most suppressed when the field reaches its maximum, making BSI most likely to happen near the peaks of the electric field. Since the peak of the electric field corresponds to the minimum of the vector potential, or equivalently the quiver velocity (cf. Sec. 2.2) the BSI process leads to a very low initial kinetic energy of electrons compared to the ionization potential and the ponderomotive energy. As a result, the so generate electrons have a very low temperature, normally only a few electronvolts.

To reach the critical field strength for BSI, the intensity required can be calculated according to Eq. (2.2):

$$I_L = \frac{\varepsilon_0 c E_L^2}{2} \approx 4 \times 10^9 Z^{-2} U_{\text{ion}}^4 [\text{eV}] \text{W cm}^{-2}. \quad (2.45)$$

In table 2.1 the BSI thresholds for ions involved in this work are given. The choice of the unit is to emphasize that the ionization happens at the foot the laser pulse, long before the peak intensity arrives. As will be shown later in chapter 5, this feature can be utilized to monitor the temporal contrast of the laser intensity.

Ion product	U_{ion} [eV]	I_{ion} [10^{18} W/ $c^2\text{m}$]
H ⁺	13.6	0.00014
He ⁺	24.6	0.0015
He ²⁺	54.4	0.0088
N ⁵⁺	97.9	0.015
N ⁶⁺	552	10
Ar ⁺	15.8	0.00025
Ar ⁸⁺	144	0.027

Table 2.1: Ionization threshold and correspondingly the required laser intensity for various ions relevant to this work, calculated with Eq. (2.45).

As the inner shells' ionization energy is drastically different from the outer shells', this clear separation of scale can facilitate ionization injection; cf. subsection 3.4.2.

It has been shown that atoms get ionized when irradiated by an intense laser pulse. If one considers the vacuum as bound virtual electrons-positrons pairs, the vacuum can be broken following similar procedures discussed therein. The onset field strength for such effects is known as the Schwinger limit, which corresponds to an intensity of $\sim 10^{29}$ W/ $c^2\text{m}$ for visible to near-infrared (VIS-NIR) wavelengths. Since the intensity range of interest in this work $\sim 10^{18}$ W/ $c^2\text{m}$ is many orders of magnitude below the Schwinger limit, a laser pulse used here will leave no wakefield in vacuum. In order to generate the wakefield, some medium is necessary. As strong-field ionization normally initiates long before the peak intensity arrives, the peak of a pulse will interact with a medium in an ionized state, or the so-called plasma state. The remainder of this chapter illustrates some basic properties of a plasma.

2.5 Definition of plasma

F. F. Chen gives a useful definition: “A plasma is a quasineutral gas of charged and neutral particles which exhibits collective behavior.” in his *Introduction to plasma physics and controlled fusion* [60]. In other words, a medium qualifies as a plasma, when its dynamics is dominated by the long range Coulomb interaction and not by collisions between its constituent particles. This is the case when the plasma parameter, i.e. the number of charged particle N_D in a sphere with a radius of the Debye length

$$\lambda_D = \sqrt{k_B T_e / 4\pi n_e e^2} \quad (2.46)$$

is much larger than unity. Here k_B denotes the Boltzmann constant, T_e the electron temperature, n_e the electron density, and e the elementary charge.

The typical plasma density used in this work is $4 \times 10^{18} \text{ cm}^{-3}$, which leads to $N_D = 28$ for 1 eV of electron temperature, hence collisions can be safely ignored. Taking into account the typical time (10s fs) and intensity ($10^{18} \text{ W}/\text{c}^2\text{m}$) scale encountered in this work, the ions in the plasma can be mostly considered static due to their high inertia. Therefore the plasma will be modeled as an electron fluid in front of an immobile ion background hereafter, unless otherwise pointed out.

When electrons in such a plasma are perturbed by an external force, e.g. the ponderomotive force of a laser pulse, a space charge field builds up which acts as the restoring force. Under the influence of this restoring force, electrons oscillate about their equilibrium positions with a characteristic frequency defined as the (electron) plasma frequency [60]

$$\omega_p = \sqrt{\frac{n_e e^2}{m_e \epsilon_0}}, \quad (2.47)$$

where m_e denotes the rest mass of an electron, and ϵ_0 the free space permittivity.

Since ω_p depends only on the density and not on any plasma wave number k_p , the group velocity $d\omega_p/dk_p = 0$, i.e., the plasma oscillation is local and does not propagate. Therefore the phase advance of a laser driven plasma wave is due completely to the propagation of the drive laser, detailed below.

2.6 Laser propagation in plasma

The propagation of electromagnetic (EM) waves in a cold plasma (characterized by the plasma frequency ω_p) is governed by the dispersion relation [59]

$$\omega_L^2 = c^2 k_L^2 + \omega_p^2, \quad (2.48)$$

where ω_L and k_L represent the angular frequency and the wave number of the laser respectively, and c is the vacuum speed of light. The plasma’s refractive index, defined as

$$\eta = \frac{k_L c}{\omega_L} = \sqrt{1 - \frac{\omega_p^2}{\omega_L^2}} = \sqrt{1 - \frac{n_e}{n_c}}, \quad (2.49)$$

determines the (linear) group velocity v_g and the phase velocity v_ϕ of the laser:

$$v_g = \eta c, \quad \text{and} \quad v_\phi = c/\eta. \quad (2.50)$$

When the laser frequency is higher than the plasma frequency, the refractive index η is between 0 and 1 and the laser wave number $k_L = \eta\omega_L/c$ is a real number. Hence the phase term $\exp(ik_L z)$ (cf. Sec. 2.1) is oscillatory, meaning the laser can propagate and the plasma is transparent. Such a plasma will be called under-dense. On the other hand, when the laser frequency is less than the plasma frequency, the refractive index hence k_L is purely imaginary. The $\exp(ik_L z)$ term becomes an exponential decay, indicating that the laser can only penetrate a skin depth of the order $1/|k_L|$. Thus the plasma is opaque, reflective, and will be called over-dense. In the special case where the laser frequency equals the plasma frequency, the refractive index vanishes and the plasma is of the critical density n_c .

To name a concrete example, the typical density used in this work, $4 \times 10^{18} \text{ cm}^{-3}$, amounts about 0.2% the critical density for the central laser wavelength of 800 nm. The drive laser pulse's group velocity v_g , hence the plasma wave phase velocity v_p , is $v_p = v_g = 0.999c$.

2.6.1 Optical guiding in plasma

Since the electron density n_e and mass m_e appear in the definition of plasma frequency, which in turn determines the plasma refractive index, electron density perturbation and relativistic mass increase will influence the laser propagation in a plasma. Expressing the modified plasma frequency as $\omega_p^* = \omega_p \sqrt{n_e/n_0} \gamma$, with n_0 denoting the ambient plasma density, the radial profile of refractive index in a sufficiently under-dense plasma can be approximated accordingly [61]:

$$\eta^*(r) \approx 1 - \frac{\omega_p^2}{2\omega_L^2} \frac{n_e(r)}{n_0 \gamma(r)}, \quad (2.51)$$

where the cycle-averaged Lorentz factor $\gamma(r) = 1 + \langle \tilde{a}^2(r) \rangle / 2 = 1 + a^2(r)/4$ is determined from the laser envelope $a(r)$ assuming a linear polarization; cf. Subsec. 2.2.2. The fast optical oscillation of the laser field is averaged over because the plasma response time $\sim 1/\omega_p$ is comparatively large, which yields the additional factor of 1/2 in the expression for $\gamma(r)$. In the limits of small density perturbation, $n_e = n_0 + \delta n$ with $\delta n \ll n_0$, and low intensity, $a^2 \ll 1$, the refractive index profile in Eq. (2.51) can be written as

$$\eta^*(r) \approx 1 - \frac{\omega_p^2}{2\omega_L^2} \left(1 + \frac{\delta n(r)}{n_0} - \frac{a^2(r)}{4} \right). \quad (2.52)$$

The $\delta n/n_0$ term can be the result of either preformed density channel, or the plasma response to the drive laser's ponderomotive force. As such, a density profile with a minimum on-axis, or an intensity profile with a peak in the center, e.g. a Gaussian beam, leads to $\partial_r \eta^* < 0$, which acts effectively as a focusing lens and offers the possibility of optical guiding. Stable guiding is achieved when focusing caused by the refractive index profile balances out that of the diffraction.

Diffraction of e.g. Gaussian beams is characterized by $w(t) = w_0 \sqrt{1 + t^2/\tau_R^2}$, with the diffraction time $\tau_R = z_R/c$ related to the Rayleigh range $z_R = k_L w_0^2/2$; cf. Subsec. 2.1.2. The spot size evolution near the focus ($t \ll \tau_R$) can be approximated as $w(t) \approx w_0(1 + t^2/2\tau_R^2)$, hence

$$\frac{\partial^2 w}{\partial t^2} \approx \frac{4c^2}{k_L^2 w_0^3}. \quad (2.53)$$

Focusing, on the other hand, can be estimated by examining the wavefront bending originating from the plasma refractive index profile [61]. Let θ denote the angle at which the wavefront bends inward, $v_{\phi 0}$ and $v_{\phi 1}$ denote the phase velocities on the laser axis and $r = w$ away from the axis at the peripheral of the beam, respectively. It follows $\theta = (v_{\phi 1} - v_{\phi 0})\Delta t/w$ over an infinitesimally small time interval Δt . As the energy flow i.e. Poynting vector is perpendicular to the wavefront, the spot size w reduces at a rate of $\partial_t w = c \sin \theta \approx c\theta$. Hence

$$\frac{\partial^2 w}{\partial t^2} \approx \frac{v_{\phi 0} - v_{\phi 1}}{w} c. \quad (2.54)$$

Considering only the contribution to $v_\phi = c/\eta^*$ from the relativistic term $a^2(r)/4$ in Eq. (2.52), Eq. (2.54) becomes

$$\frac{\partial^2 w}{\partial t^2} \approx -\frac{1}{8} \frac{\omega_p^2}{\omega_L^2} \frac{c^2}{w} a_0^2, \quad (2.55)$$

where the term containing $a^2(w)$ is neglected at the edge of the beam, and $a_0 = a(0)$. The condition for relativistic self-focusing can thus be given, by comparing Eq. (2.53) and Eq. (2.55) near the focus ($w \rightarrow w_0$), as

$$\frac{a_0^2 w_0^2 \omega_p^2}{32 c^2} > 1. \quad (2.56)$$

This condition can be formulated as a power threshold $P/P_c > 1$, because a_0^2 is proportional to the peak intensity I_0 , cf. Eq. (2.40), and $P = I_0 \pi w_0^2/2$ for a Gaussian beam. Thus the critical power is given by

$$P_c = 8\pi\epsilon_0 c \left(\frac{m_e c^2}{e} \right)^2 \frac{\omega_L^2}{\omega_p^2} \approx 17.4 \frac{\omega_L^2}{\omega_p^2} [\text{GW}]. \quad (2.57)$$

Density contrast induced guiding can be analysed in a similar manner. The critical channel depth n_c for a parabolic channel can be given as [8]

$$n_c = \frac{1}{\pi r_e r_0^2}, \quad \text{with} \quad r_e = \frac{1}{4\pi\epsilon_0} \frac{e^2}{m_e c^2} \quad (2.58)$$

denoting the classical electron radius ($r_e \sim 2.8 \times 10^{-15}$ m), and r_0 the matched spot radius. A Gaussian beam with $w_0 = r_0$ can be stably guided in this channel whereas an unmatched spot will oscillate in size while being confined by the channel given the channel is sufficiently broad [8]. The spot oscillation period Λ can be estimated as [62]

$$\Lambda = \frac{\pi^2 r_0^2}{\lambda_L}. \quad (2.59)$$

Although the equation above is derived for a parabolic plasma channel, it works reasonably well in the self-guided regime employed in this work; cf. Fig. 5.4.

With the propagation of a laser pulse established, next chapter starts to address the central question of this thesis: plasma wave excitation and electron acceleration.

3 Laser wakefield acceleration

The plasma wakefield can support large electric field in excess of 1 GV/cm, three orders of magnitude higher than the acceleration gradient in a state-of-the-art radio frequency accelerator. Harnessing the wakefield could potentially shrink the size of a particle accelerator by the same factor, making accelerators more cost-effective and accessible. However, the small size ($\lambda_p \sim 10 \mu\text{m}$) and high phase velocity ($v_p \sim c$) of a laser driven wakefield poses stringent requirements on particle trapping and acceleration. In order to build a laser wakefield accelerator for particles, electrons particularly, these requirements need to be fulfilled. This chapter discusses the condition of electron trapping in the wakefield, techniques to achieve electron injection, limitations and scalings of a laser driven wakefield accelerator, and possible strategies to overcome these limitation.

3.1 Wakefield equations

Vlasov-Maxwell system

In general physical properties of a collisionless fluid can be retrieved from the evolution of the density distribution $f(\mathbf{r}, \mathbf{p}, t)$, where \mathbf{r} denotes the spatial coordinate, \mathbf{p} the momentum, and t the time. Dropping $(\mathbf{r}, \mathbf{p}, t)$ for brevity, the dynamics of f follow the Vlasov equation [63]

$$\frac{df}{dt} = \frac{\partial f}{\partial t} + \frac{d\mathbf{r}}{dt} \cdot \frac{\partial f}{\partial \mathbf{r}} + \frac{d\mathbf{p}}{dt} \cdot \frac{\partial f}{\partial \mathbf{p}} = 0, \quad (3.1)$$

which is in essence a continuity equation for the particle density in the in the (\mathbf{r}, \mathbf{p}) phase space. As such the equation above is only valid when the total charge in the plasma is conserved, namely, when ionization and recombination do not play an important role.

In conjunction with Maxwell's equations (2.1) governing the electromagnetism, the Lorentz force equation (2.19) driving the fluid motion, and the explicit form for charge and current density

$$\rho = -e \int f d^3p, \quad \mathbf{j} = -e \int \mathbf{v} f d^3p, \quad (3.2)$$

$\mathbf{v} = d\mathbf{r}/dt$ being the velocity of a fluid element, the system is in principle determined. One can solve these equations numerically using for instance particle-in-cell (PIC) codes. Especially with the recent code development such as CALDER-CIRC [38] and FBPIC [39], fast quasi-3D simulations become feasible, which allows for systematic parameter scans; cf. section 5.3.

The particle density distribution f is not very practical to be handled analytically. Instead, a reduced system can be introduced to intuitively grasp some of the essential physics. Integrating the Vlasov equation (3.1) over the entire momentum space and plugging in Eq. (3.2) yields the continuity equation in the coordinate space

$$\frac{\partial \rho}{\partial t} + \nabla \cdot \mathbf{j} = 0. \quad (3.3)$$

Charge separation sets up an electric potential according to the Poisson equation

$$\nabla^2 \phi = -\frac{\rho}{\varepsilon_0}. \quad (3.4)$$

Along with the electromagnetic wave equation, cf. Eq. (2.4),

$$\left(\frac{1}{c^2} \frac{\partial^2}{\partial t^2} - \nabla^2 \right) A^\mu = \mu_0 J^\mu, \quad (3.5)$$

the equation of motion for a fluid element, cf. Eq. (2.23),

$$\frac{\partial}{\partial t} (\mathbf{p} - e\mathbf{A}) = -\nabla(\gamma m_e c^2 - e\phi), \quad (3.6)$$

completes the set of fundamental equations.

Conventions and assumptions

To simplify the problem even further, a series of conventions and assumptions are adopted and listed below:

- immobile, neutralizing ion background;
- cold plasma, since the typical electron temperature of few eV is well below the oscillation/ponderomotive energy of a few MeV; cf. section 2.4;
- quasi-1D, the laser pulse is not tightly focused, namely, $w_0 k_p \gg 1$, with w_0 being the laser spot size, and $k_p = \omega_p/c$ the plasma wave number;
- the linearly polarized drive laser pulse propagates to the z -direction with a group velocity v_g without evolution, i.e. $\mathbf{A} = A_\perp(z - v_g t)$; the assumption of a non-evolving laser is justified as long as $z_R k_p \gg 1$, i.e., the Rayleigh range (the length scale of laser evolution) is much larger than the length scale of plasma dynamics $1/k_p$.

Natural units and normalization

As the discussion is about the motion of an electron fluid in the relativistic regime, there is a natural set of units to normalize the dynamical variables, which removes distractions and emphasizes physics. They are listed below in table 3.1.

3.1. Wakefield equations

Quantity	Notation	Norm. notation	Value
speed of light	c	n/a	1
elementary charge	e	n/a	1
electron mass	m_e	n/a	1
electron momentum	p	\tilde{p} , or $\gamma\beta$	$p/m_e c$
electron density	n_e	n	n_e/n_0
vector potential	A	a	$eA/m_e c$
scalar potential	ϕ	φ	$e\phi/m_e c^2$

Table 3.1: Summary of natural units and normalization. n_0 denotes the ambient electron density.

With these conventions, $\mu_0 = \varepsilon_0^{-1} = \omega_p^2 = k_p^2$, hence the dimensionless form of the equations above reads

Continuity

$$\frac{\partial n}{\partial t} + \frac{\partial}{\partial z}(n\beta_z) = 0, \quad (3.7)$$

Poisson

$$\frac{\partial^2 \varphi}{\partial z^2} = k_p^2(n - 1), \quad (3.8)$$

EOM

$$\frac{\partial}{\partial t}(\gamma\beta_z) = \frac{\partial}{\partial z}(\varphi - \gamma), \quad (3.9)$$

and EM wave

$$\left(\frac{\partial^2}{\partial t^2} - \frac{\partial^2}{\partial z^2}\right)a = k_p^2 n \beta_\perp = k_p^2 \frac{na}{\gamma}. \quad (3.10)$$

To get Eqs. (3.9) and (3.10) conservation of transverse canonical momentum $\gamma\beta_\perp = a$ is used, with β_\perp denoting the transverse fluid velocity. Equation (3.10) accounts for the laser pulse evolution caused by the transverse plasma oscillation, which will be neglected in the derivation below.

Co-moving coordinates

These equations are usually solved using the co-moving coordinates $\tau = t$, $\zeta = z - \beta_p t$, such that [59]

$$\frac{\partial}{\partial z} = \frac{\partial}{\partial \zeta} \quad \text{and} \quad \frac{\partial}{\partial t} = \frac{\partial}{\partial \tau} - \beta_p \frac{\partial}{\partial \zeta}, \quad (3.11)$$

with $\beta_p = \sqrt{1 - 1/\gamma_p^2}$, and $\gamma_p = \omega_L/\omega_p$ being the Lorentz factor associated with the plasma wave's phase velocity, which roughly equals the group velocity of a non-evolving driver (cf. Sec. 3.5). Thus the equations become

Continuity

$$\frac{\partial n}{\partial \tau} = \frac{\partial}{\partial \zeta} [n(\beta_p - \beta_z)], \quad (3.12)$$

Poisson

$$\frac{\partial^2 \varphi}{\partial \zeta^2} = k_p^2 (n - 1), \quad (3.13)$$

EOM

$$\frac{\partial}{\partial \tau} (\gamma \beta_z) = \frac{\partial}{\partial \zeta} [\varphi - \gamma (1 - \beta_p \beta_z)]. \quad (3.14)$$

Note that the transform into the co-moving coordinate is Galilean and therefore does not conform with special relativity.

Quasi-static approximation

The advantage of the co-moving coordinates—together with the assumption of a non-evolving driver—is that it facilitates the quasi-static approximation (QSA) [59], where the partial time derivatives are neglected, namely, $\partial/\partial \tau = 0$. In the QSA, the equation of motion (3.14) can be easily integrated to give

$$\gamma (1 - \beta_p \beta_z) - \varphi = 1, \quad (3.15)$$

with the initial condition that the plasma is unperturbed before the arrival of the laser, i.e., $\gamma = 1$, $\beta_z = 0$, $\varphi = 0$ for $\zeta \rightarrow -\infty$. Similarly, the continuity equation (3.12) with $\beta_z = 0$ and $n = 1$ for $\zeta \rightarrow -\infty$ results in

$$n (\beta_p - \beta_z) = \beta_p, \quad (3.16)$$

Equation (3.16) implies that the fluid velocity can not exceed the plasma wave phase velocity i.e. $|\beta_z| < \beta_p$, otherwise when $\beta_p < \beta_z$, the electron density $n = \beta_p / (\beta_p - \beta_z) < 0$. This negative density can be interpreted as wave breaking; cf. Sec. 3.3. It suggests also that the electron density becomes very large when $\beta_z \approx \beta_p$; such density spikes are a feature of nonlinear plasma waves. Furthermore the density has a minimum of 0.5 when $\beta_z \approx -\beta_p$.

Separating the γ -factor into parallel and transverse components:

$$\gamma = \gamma_\perp \gamma_\parallel \quad \text{with} \quad \begin{cases} \gamma_\perp = (1 + a^2)^{1/2} \\ \gamma_\parallel = (1 - \beta_z^2)^{-1/2}, \end{cases} \quad (3.17)$$

β_z can be explicitly solved with the quadratic formula as [59]

$$\beta_z = \frac{\beta_p - \psi}{1 - \beta_p \psi} \quad \text{with} \quad \psi = \sqrt{1 - \frac{1 + a^2}{\gamma_p^2 (1 + \varphi)^2}} \quad (3.18)$$

by squaring Eq. (3.15) after substituting γ with Eq. (3.17).

The other root $\beta_z^* = (\beta_p + \psi) / (1 + \beta_p \psi)$ is not physical because $\beta_z^* - \beta_p = \psi / \gamma_p^2 (1 + \beta_p \psi) > 0$, which suggests wave-breaking; cf. section 3.3. The electron density, n , results from inserting Eq. (3.18) into Eq. (3.16):

$$n = \gamma_p^2 \beta_p (\psi^{-1} - \beta_p). \quad (3.19)$$

Thus the Poisson equation (3.13) turns into the 1D wakefield equation [59]

$$\frac{d^2\varphi}{d\zeta^2} = k_p^2 \gamma_p^2 (\beta_p \psi^{-1} - 1) \quad (3.20)$$

$$= k_p^2 \gamma_p^2 \left\{ \beta_p \left[1 - \frac{1+a^2}{\gamma_p^2(1+\varphi)^2} \right]^{-1/2} - 1 \right\}. \quad (3.21)$$

In a sufficiently under-dense plasma, the plasma wave's phase velocity is highly relativistic, i.e. $\gamma_p \gg 1$, $\beta_p \approx 1 - 1/2\gamma_p^2$, and $\psi^{-1} \approx 1 + (1+a^2)/2\gamma_p^2(1+\varphi)^2$. Substituting β_p and ψ^{-1} into Eq. (3.20) yields, to the leading order,

$$\frac{d^2\varphi}{d\zeta^2} \approx \frac{k_p^2}{2} \left[\frac{1+a^2}{(1+\varphi)^2} - 1 \right]. \quad (3.22)$$

3.1.1 Linear wakefield

For a weak driver ($a \ll 1$, $\varphi \ll 1$), neglecting terms with higher order than $\mathcal{O}(\varphi)$ further reduces the wakefield equation (3.22) to

$$\left(\frac{\partial^2}{\partial \zeta^2} + k_p^2 \right) \varphi = \frac{k_p^2}{2} a^2, \quad (3.23)$$

which is an inhomogeneous Helmholtz equation with a formal solution [59]

$$\varphi(\zeta) = \frac{k_p}{4} \int_{-\infty}^{\zeta} d\zeta' |a(\zeta')|^2 \sin [k_p (\zeta - \zeta')]. \quad (3.24)$$

Taking for example a drive pulse with a \sin^2 -shaped intensity envelope

$$a^2(\zeta) = \begin{cases} a_0^2 \sin^2(\pi\zeta/\zeta_L) & \text{for } 0 \leq \zeta \leq \zeta_L \\ 0 & \text{otherwise,} \end{cases} \quad (3.25)$$

the wake potential behind the driver ($\zeta < 0$) can be solved as

$$\begin{aligned} \varphi(\zeta) &= \frac{k_p a_0^2}{4} \int_{\zeta_L}^0 d\zeta' \sin^2(\pi\zeta'/\zeta_L) \sin [k_p (\zeta - \zeta')] \\ &= -C_{\text{env}} \sin [k_p (\zeta - \zeta_L/2)], \end{aligned} \quad (3.26)$$

which is a sinusoidal modulation with a period of the cold plasma wavelength

$$\lambda_p = 2\pi/k_p = 2\pi c \sqrt{\frac{m_e \varepsilon_0}{n_e e^2}} \approx \frac{33 \mu\text{m}}{\sqrt{n_e [10^{18} \text{ cm}^{-3}]}}. \quad (3.27)$$

The envelope constant, $C_{\text{env}} = a_0^2 \sin(k_p \zeta_L/2)/(4 - k_p^2 \zeta_L^2/\pi^2)$, summarizes the properties of the drive pulse. The longitudinal electric field is simply

$$\begin{aligned} E_\zeta &= -\frac{\partial \varphi}{\partial \zeta} \\ &= k_p C_{\text{env}} \cos [k_p (\zeta - \zeta_L/2)]. \end{aligned} \quad (3.28)$$

3.1. Wakefield equations

This result can be generalized to 3D given the laser pulse is not tightly focused i.e. $w_0 \gg \zeta_L$, where w_0 is the waist assuming a Gaussian transverse profile $a(r) = a_0 \exp(-r^2/w_0^2)$, with r being the distance from the optical axis. As such the radial field is

$$\begin{aligned} E_r &= -\frac{\partial \varphi}{\partial r} \\ &= -\frac{4r}{w_0^2} \exp\left(-\frac{2r^2}{w_0^2}\right) C_{\text{env}} \sin[k_p(\zeta - \zeta_L/2)]. \end{aligned} \quad (3.29)$$

Close to the axis, the radial field increases with the the distance from the axis, enabling stable bunch formation in the focusing phase. Along the laser propagation direction, the radial field is $\pi/2$ out of phase with the longitudinal field. Therefore only one quarter of the period is simultaneously accelerating and focusing, as shown in Fig. 3.1.

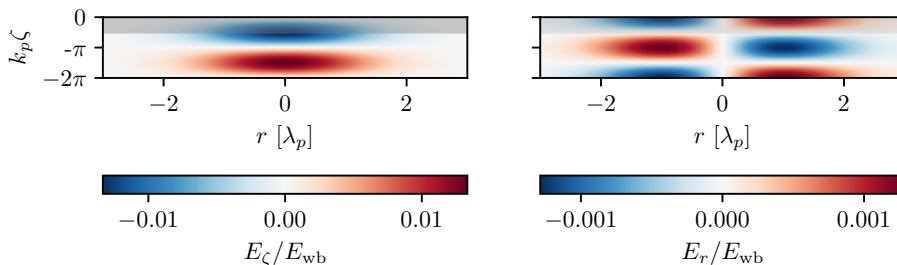


Figure 3.1: Longitudinal (left) and transverse (right) electric field of a linear plasma wave generated by a laser pulse with a \sin^2 -shaped intensity envelope as in Eq. (3.25), with $\zeta_L = \lambda_p/2$, and $a_0 = 0.2$. The pulse has a Gaussian transverse profile with a waist of $w_0 = 2\lambda_p$ and propagates to the top of the page. The fields are normalized to the cold wave-breaking field $E_{wb} = m_e c \omega_p / e$; cf. section 3.3. The shaded area represents the phase that is simultaneously accelerating and focusing, $k_p \zeta \in (-\pi/2, 0)$.

When $dC_{\text{env}}/d\zeta_L = 0$, or $\zeta_L \approx 0.83\lambda_p$, a \sin^2 -shaped pulse drives a linear plasma wave most effectively, yielding a maximum accelerating field of

$$|E_{\zeta, \text{max}}| = k_p C_{\text{env}}|_{\zeta_L \approx 0.83\lambda_p} \approx 0.4a_0^2 E_{wb}, \quad (3.30)$$

with $E_{wb} = m_e c \omega_p / e$, or $E_{wb}[\text{V/m}] \approx 96\sqrt{n_e[\text{cm}^{-3}]}$, being the cold wave breaking field; cf. early work by Dawson [64] and Sec. 3.3. This resonant condition is more often formulated in terms of the full width at half intensity maximum pulse duration, τ , as $c\tau \sim \lambda_p/2$, to incorporate other pulse shapes such as Gaussian pulses. Taking $a_0 = 0.2$ for instance, the peak field strength would be approximately 3 GV/m for the typical density of $4 \times 10^{18} \text{ cm}^{-3}$.

Compared to linear plasma waves, a nonlinear plasma wave offers a higher acceleration gradient (Sec. 3.1.2) and a larger overlap region for accelerating and focusing phase (Sec. 3.1.3), which is more desirable for an accelerator and will be discussed below.

3.1.2 Nonlinear wakefield

The 1D nonlinear wakefield equation (3.22) is usually solved numerically, as analytical solutions exist only for simple pulse shapes such as rectangular pulses [8]. Figure 3.2 compares

3.1. Wakefield equations

numerical solutions for laser pulses with a Gaussian intensity envelope at two different peak intensities—one with $a_0 = 0.2$ on top and the other with $a_0 = 2.0$ on the bottom. Two key features should be noticed: a) the electron density modulation becomes more spiky hence the E -field is partwise almost a linear function of space, in contrast to the sinusoidal density modulation and E -field at the low intensity; and b) the wavelength of the plasma oscillation becomes longer when the laser intensity gets higher.

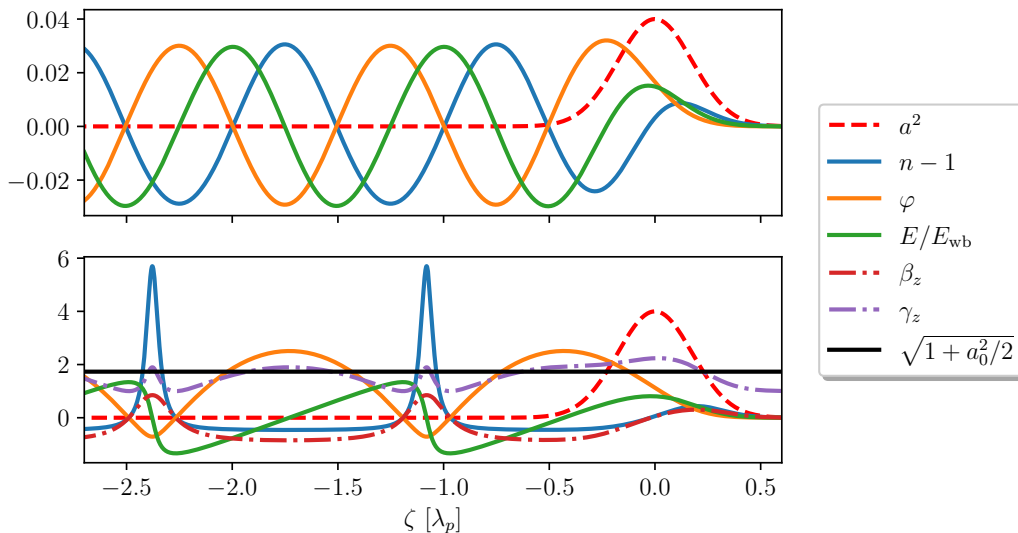


Figure 3.2: Comparison of 1D linear and nonlinear plasma waves driven by Gaussian pulses with peak potentials a_0 of 0.2 (upper) and 2.0 (lower). The full width at $1/e$ of intensity (a^2) maximum pulse length is $\lambda_p/2$ in both panels. The electric field is normalized to the cold wave breaking field E_{wb} . Note the difference in the ordinate scale— $|E| > E_{wb}$ can occur in a nonlinear plasma wave.

Let $\lambda_{p,nl}$ denote this elongated nonlinear plasma wavelength. Analytical solutions, for square pulses with optimal length for plasma wave excitation ($\sim \lambda_p/2$), predict an intensity dependency of $\lambda_{p,nl}$ as [8]

$$\lambda_{p,nl} = \lambda_p \begin{cases} 1 + 3\chi^2/16 & \text{for } \chi \ll 1 \\ (2/\pi)(\chi + \chi^{-1}) & \text{for } \chi \gg 1 \end{cases} \quad (3.31)$$

with the scaling parameter $\chi = (a_0^2/2)/\sqrt{1 + a_0^2/2}$.

A slightly different scaling of $\lambda_{p,nl}$ can be obtained when the electron oscillation in the plasma is examined. Since the electron oscillation in a nonlinear plasma wave is relativistic, the wave lengthening can be attributed to the reduction of plasma frequency due to the relativistic increase of electron mass [65], i.e., the lengthening factor $\lambda_{p,nl}/\lambda_p = \sqrt{\gamma}$. As the quiver momentum should scale with the vector potential a , an estimate of the Lorentz factor would be $\gamma = \sqrt{1 + a_0^2/2}$. The factor of $1/2$ accounts for the average over fast oscillations assuming a linear polarization, and a_0 denotes the peak value of the normalized vector potential; cf. the lower panel of Fig. 3.2. Consequently, the scaling can be given as

$$\lambda_{p,nl}/\lambda_p = (1 + a_0^2/2)^{1/4}. \quad (3.32)$$

Figure 3.3 compares these two scalings, alongside the wave lengthening drawn from numerical solutions of the 1D wakefield equation (3.22). All 1D models introduced so far predict a plasma wave elongation yet their values can differ by more than 20% for $a_0 > 1$, where the majority of wakefield acceleration experiments are performed. As will be shown in Secs. 5.2 and 5.3, few-cycle shadowgraphy allows for measurement of the nonlinear wavelength at a precision that distinguishes among these models. Shadowgraphic measurements show that 1D models are insufficient in explaining plasma wave lengthening in a practical experimental configuration, where 3D effects, transverse electron motion in particular, play a crucial role.

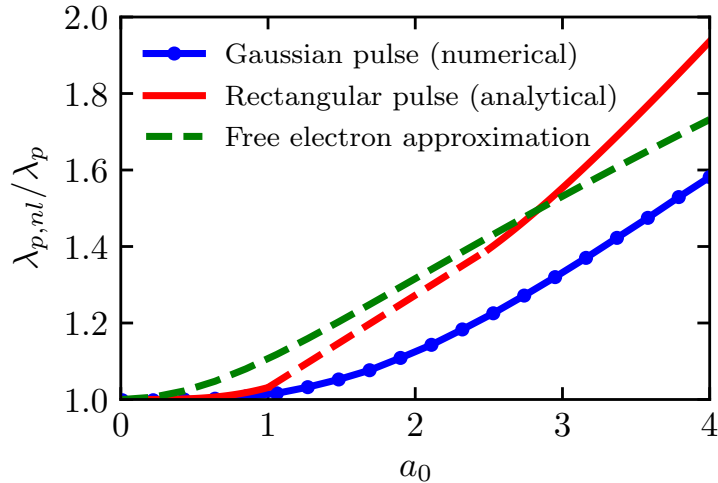


Figure 3.3: Comparison of nonlinear plasma wavelength scalings found in literature [8, 65] with wave lengthening obtained from numerical solutions of the 1D wakefield equation (3.22) for Gaussian pulses. Note the analytical solutions of rectangular pulses have two disconnected regions of validity; the dashed segment of the red curve is to guide the eye. Parameters for numerical solutions are chosen to closely resemble experiments performed in this work, namely, the plasma density is $3 \times 10^{18} \text{ cm}^{-3}$ and the drive pulse’s FWHM duration is 30 fs. Figure reproduced from Ref. [43].

3.1.3 Bubble formation

Analogous to the linear case discussed in subsection 3.1.1, the 1D nonlinear wakefield theory can also be extended to higher dimensions for a wide spot ($w_0 \gg c\tau$), where the electron motion is predominantly longitudinal. As all models outlined above predict that the plasma wave lengthens as the driver intensity increases, the higher intensity near the laser axis will result in a larger period of the plasma oscillation, given a Gaussian-like transverse intensity profile. Hence the phase fronts of a nonlinear plasma wave become curved, with an increasing curvature farther behind the driver; cf. Fig. 3.4. This phase front curvature makes almost the entire axially accelerating phase of the nonlinear wake (cf. Fig. 3.2) radially focusing, which constitutes roughly a half of the wake period, superior to the quarter period offered by a linear wake (Sec. 3.1.1). It will be shown later in Sec. 3.3 that transverse wave-breaking [34] takes place once the phase front curvature exceeds certain threshold, which can lead to self-injection of electrons into the plasma wave.

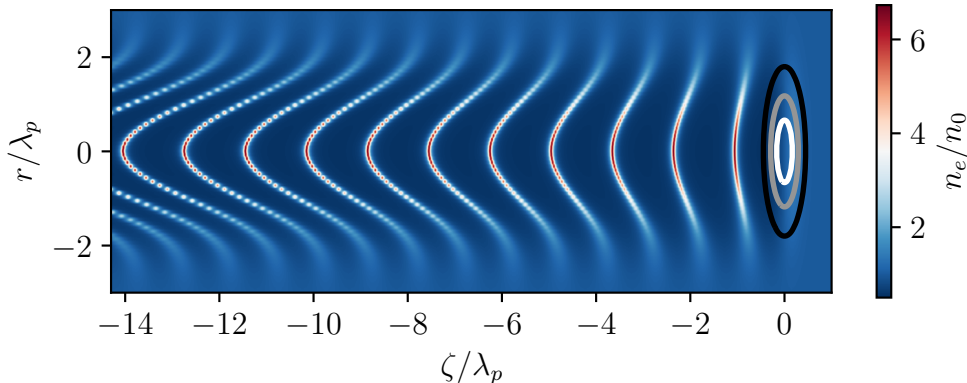


Figure 3.4: A naive extension of the 1D nonlinear wakefield solution to 3D, indicating plasma wave phase front curvature caused by the drive laser’s transverse intensity profile. The drive laser is a wide Gaussian pulse $a_0 \exp(-r^2/w_0^2) \exp(-\zeta^2/2L^2)$ with $a_0 = 2$, $w_0 = 2\lambda_p$ and $L = 0.25\lambda_p$. Gray-scale contours represent $a \in [0.4, 1.0, 1.6]$.

The situation is more complicated if the laser pulse is tightly focused, i.e., when the spot size w_0 is comparable to the pulse length $c\tau$. In this case, transverse ponderomotive force pushes electron sideways and a region with nearly zero electron density can form behind the driver, known as the bubble or blowout [9]. Note that bubble formation is necessarily a three-dimensional effect, because $n_e = 0.5$ is the minimal electron density allowed by a 1D plasma wave; cf. Sec. 3.1. Though closed-form theory for this bubble regime does not yet exist due to its complexity, some properties of the plasma blowout can be deduced from simple physical arguments. As electrons are blown out by the drive laser’s ponderomotive force, which only extends out to the edge of the laser, the blowout radius should be roughly the laser spot size, i.e. $R_b \sim w_0$. Assuming an approximately spherical bubble with zero electron density, Lu et al. [36, 37] deduced the bubble radius, in the unit of $1/k_p$,

$$R_b \simeq 2\sqrt{a_0} \quad (3.33)$$

by balancing the transverse ponderomotive force of the laser pulse $\nabla_{\perp} a_0^2/\gamma \sim a_0/R_b$ and the Coulomb force of the ion channel $E_r \sim R_b$. The refinement factor of 2 is inferred from particle-in-cell simulations; and $a_0 \sim \gamma$ is used to estimate the ponderomotive force.

For a given laser power and plasma density, there is a matched condition allowing for well-defined narrow bubble sheath formation and good guiding properties for the laser [35]:

$$a_0 \simeq 2(P/P_c)^{1/3}. \quad (3.34)$$

Initially unmatched spot will oscillate in size due to the interplay between relativistic self-focusing and diffraction (cf. Sec. 5.3). In particular, for a spot size much larger than the matched one, a_0 will be too small to cause blowout. Full blowout is only achieved once the laser relativistically self-focuses to (or below) the matched size. On the other hand, when the laser is focused too tight, electrons near the laser axis will be blown out rapidly due to a stronger transverse ponderomotive force while electrons at the laser edge will feel a very small ponderomotive force hence barely move. This leads to a wide sheath, and an ineffective guiding due to an insufficient refractive index gradient to counter-act diffraction [36].

3.2 Electron trapping in wakefield

As a prerequisite for the discussion of electron trapping, the motion of a test electron in the wakefield will first be modelled. The Lagrangian for a test electron in a wakefield described by its potential, φ , and in the presence of a laser field, a , cf. Eq. (2.17), reads

$$\mathcal{L} = -\frac{1}{\gamma} - \beta \cdot a + \varphi, \quad (3.35)$$

with all variables in the natural units listed in table 3.1. The Legendre transformation of the Lagrangian gives the Hamiltonian [46]

$$\begin{aligned} \mathcal{H} &= \beta \cdot \frac{\partial \mathcal{L}}{\partial \beta} - \mathcal{L} \\ &= \gamma - \varphi. \end{aligned} \quad (3.36)$$

To make use of the wakefield potential $\varphi(\zeta)$ obtained in the previous chapter, \mathcal{H} needs to be transformed into the same co-moving coordinates $\zeta = z - \beta_p t$. This transformation can be performed with a type-2 generating function [66], $F_2(z, p, t) = p(z - \beta_p t)$, such thatⁱ

$$\zeta = \frac{\partial F_2}{\partial p} \quad \text{and} \quad \tilde{p}_z = \frac{\partial F_2}{\partial z} = p. \quad (3.37)$$

The Hamiltonian in the co-moving coordinates then reads

$$\begin{aligned} H(\zeta, p) &= \mathcal{H} + \frac{\partial F_2}{\partial t} \\ &= \sqrt{1 + a(\zeta)^2 + p^2} - \varphi(\zeta) - p\beta_p. \end{aligned} \quad (3.38)$$

Since $H(\zeta, p)$ has no explicit time dependence i.e. its value conserves, a contour in the (ζ, p) phase space corresponds to a stationary orbit of a test electron in the wakefield.

Phase space separatrix

The forward momentum p can be solved from the equation above with the quadratic formula as

$$p = \gamma_p^2 \left[\beta_p (H + \varphi) \pm \sqrt{(H + \varphi)^2 - \frac{1 + a^2}{\gamma_p^2}} \right]. \quad (3.39)$$

Plotting p versus ζ for various values of H results in the orbits shown in the lower panel of figure 3.5. Two distinct types of orbits can be identified: open orbits are attributed either to electrons that oscillate with relatively low energies and are considered to contribute to the plasma wave formation, e.g. electrons with initial Hamiltonian $H_0 = 1$ or equivalently $p = 0$, or to electrons that have very large forward momenta and overtake the wakefield, which rarely present in a cold plasma; in contrast, closed orbits accommodate electrons that get trapped and gain a significant amount of energy in the wakefield.

ⁱThe new momentum p is only the longitudinal component of the original momentum \tilde{p}_z .

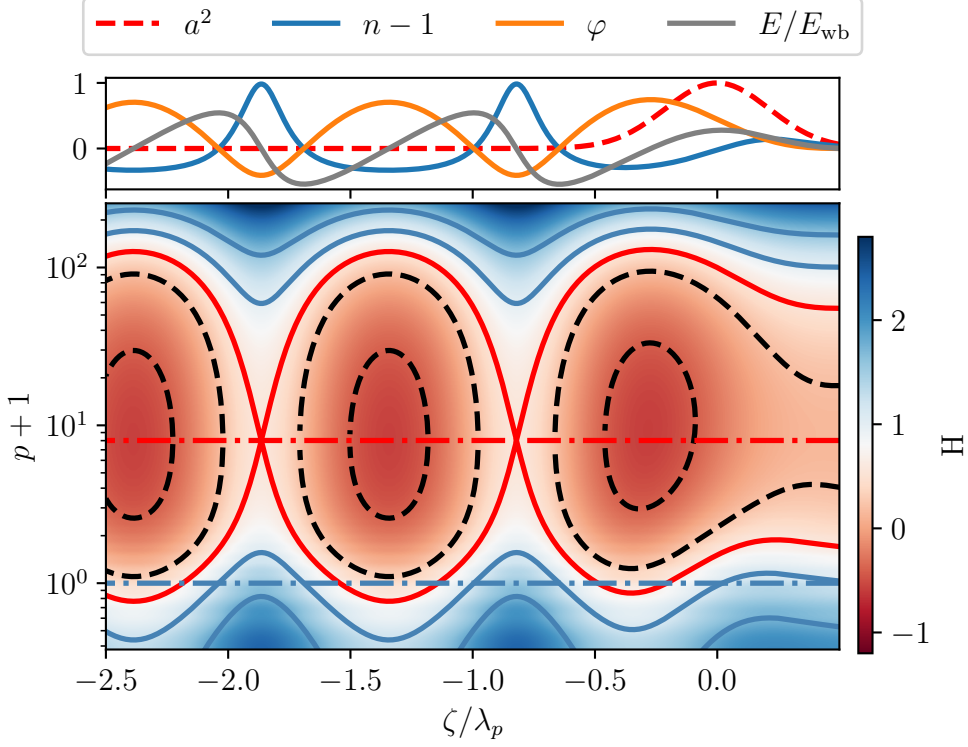


Figure 3.5: *Top*: Numerical solutions of the 1D wakefield equations for a Gaussian pulse with $a_0^2 = 1$, $c\tau_{\text{FWHM}} = 0.5\lambda_p$, in a plasma with $\beta_p = 0.99$. *Bottom*: Electron orbits in the (ζ, p) phase space. Dashed black lines are trapped orbits; solid blue lines are fluid orbits. The solid red line represents the separatrix with the dash-dotted red line indicating $p = \gamma_p\beta_p$. The dash-dotted blue line marks $p = 0$. The color scale is for the value of H . Note that the p -axis is shifted by 1 for a better representation on a logarithmic scale.

The boundary between those two types, the separatrix, belongs to electrons having exactly the plasma wave phase velocity at nodes (minima) of the wake potential, i.e. $p(\zeta_{\text{node}}) = \gamma_p\beta_p$, with $\varphi(\zeta_{\text{node}}) = \varphi_{\text{min}}$. This is the case when the discriminant in Eq. (3.39) is zero, i.e.

$$H_{\text{sep}} = \frac{\sqrt{1 + a^2(\zeta_{\text{node}})}}{\gamma_p} - \varphi_{\text{min}}. \quad (3.40)$$

With stationary electron orbits inside the wakefield established, the following sections discuss electron trapping and acceleration.

Trapping condition

An electron is considered trapped if it has a longitudinal momentum greater than the smaller-of-the-two value of the separatrixⁱⁱ before the arrival of the laser, i.e. $p > p_{\text{sep}}$, when $\zeta \rightarrow +\infty$.

ⁱⁱThe electron momentum also needs to be less than the larger value of the separatrix, corresponding to MeV-level kinetic energy before driver's arrival, which is automatically fulfilled in the cold plasma with few-eV temperature considered here.

This condition translates into a threshold of electron kinetic energy [66]

$$\mathcal{E}_{\text{trap}} = \sqrt{1 + p_{\text{sep}}^2(+\infty)} - 1. \quad (3.41)$$

Shown in Fig. 3.6, the trapping threshold is lower for plasma waves with higher amplitude or lower phase velocity. As such, various injection methods have been discovered.

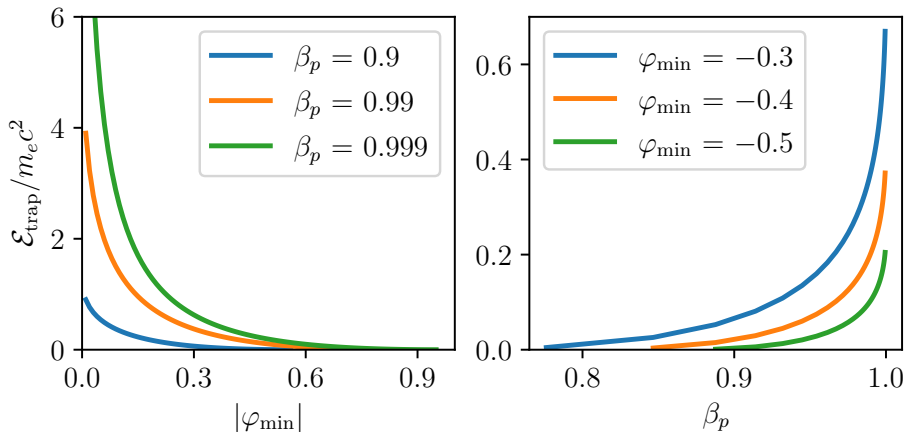


Figure 3.6: *Left*: Trapping threshold as a function wakefield amplitude for various wakefield phase velocities; *Right*: Trapping threshold as a function of plasma wake phase velocity for various wakefield amplitudes.

3.3 Wave breaking and self-injection

Since trapping favors a stronger wake, questions regarding the maximal attainable plasma wave amplitude naturally arise. Especially, in the context of electron acceleration the wave amplitude defines the acceleration gradient.

One can first have an estimate without resorting to numerical solutions of the wakefield equations. Recall the equation of motion for a fluid element (3.14) and Poisson equation (3.13) in the quasi-static approximation

$$\begin{aligned} \frac{\partial \varphi}{\partial \zeta} &= \frac{\partial}{\partial \zeta} \gamma (1 - \beta_p \beta_z) \\ \frac{\partial^2 \varphi}{\partial \zeta^2} &= k_p^2 (n - 1). \end{aligned}$$

Multiplying respectively the LHSs and RHSs of these two equations, and substituting the electron density with $n = \beta_p / (\beta_p - \beta_z)$ according to Eq. (3.16), results in

$$\frac{\partial \varphi}{\partial \zeta} \frac{\partial^2 \varphi}{\partial \zeta^2} = k_p^2 \frac{\beta_z}{\beta_p - \beta_z} \left(\frac{\partial \gamma}{\partial \zeta} - \beta_p \frac{\partial \gamma \beta_z}{\partial \zeta} \right). \quad (3.42)$$

Behind the driver, $a = 0$, and $\gamma = 1/\sqrt{1 - \beta_z^2}$; cf. Eq. (3.17). The equation above, upon noticing $\partial_\zeta(\gamma\beta_z) = (\partial_\zeta\gamma)/\beta_z$,ⁱⁱⁱ simplifies to

$$\frac{1}{2} \frac{\partial}{\partial \zeta} \left(\frac{\partial \varphi}{\partial \zeta} \right)^2 = \frac{1}{2} \frac{\partial}{\partial \zeta} E_\zeta^2 = -k_p^2 \frac{\partial \gamma}{\partial \zeta}, \quad (3.43)$$

which, can be easily integrated and results in [59]

$$E_\zeta(\zeta) = \pm \sqrt{2[\gamma_{\max} - \gamma(\zeta)]} k_p, \quad (3.44)$$

with γ_{\max} associated with the maximal velocity of the fluid oscillation.

The fluid velocity can not exceed the plasma wave phase velocity, otherwise neighboring electron sheaths may cross and the wave loses its coherence, marking the onset of self-trapping. Therefore in the limit of $\beta_z \rightarrow \beta_p$ i.e. $\gamma_{\max} \rightarrow \gamma_p$, the maximal electric field can be obtained, in physical units, as

$$|E_{\max}| = \sqrt{2(\gamma_p - 1)} E_{\text{wb}}, \quad \text{with} \quad E_{\text{wb}} = \frac{m_e c \omega_p}{e} \quad (3.45)$$

known as the cold wave-breaking limit [64, 67]. Setting $\gamma(\zeta) = 1$ is based on the recognition that extrema of the E -field occur at the points where fluid electrons have zero momentum;^{iv} cf. Fig. 3.5 where the blue dash-dotted line ($p = 0$) intersects the blue curve around it.

One way of injecting electrons into the wakefield is to drive the wakefield to the wave-breaking limit so that the trapping threshold approaches zero. Thus even the electrons initially at rest can get trapped and accelerated. This condition relaxes for a warm plasma [68, 69] for two-fold reasons: on the one hand, plasma thermal pressure prevents density spikes from getting too sharp; on the other hand, thermal motion in the direction of the wave propagation leads to self-trapping at a even lower wave amplitude hence damps the wave growth.

3.3.1 2D wave breaking in cylindrical symmetry

The 1D scenario just presented already allows longitudinal wave breaking to take place. In a real experiment, 3D effects will relax the condition even further [34]. For instance, in a plasma guiding channel with a parabolic profile, the lower plasma density near the axis leads to a longer local plasma wavelength. Such a transverse variation of the plasma wavelength gives rise to curved phase fronts analogous to the relativistic effect introduced in Sec. 3.1.3, with the radius of curvature getting larger the farther behind the driver.

The curved phase front caused by the transverse variation of the plasma wavelength can be approximated by a parabolic function $2\rho z = r^2$ in the vicinity of the axis, where ρ denotes the local radius of curvature, z the coordinate along propagation direction, and r the distance to the axis. Cylindrical symmetry is assumed here for simplicity. For a nonlinear plasma wave, the oscillation amplitude of fluid electrons $\psi(r)$ can be very large ($\sim \lambda_p$), and the

ⁱⁱⁱ $\partial_\zeta\gamma = \beta_z\gamma^3\partial_\zeta\beta_z$, hence $\partial_\zeta\gamma\beta_z = \gamma\partial_\zeta\beta_z + \beta_z\partial_\zeta\gamma = (1/\beta_z\gamma^2 + \beta_z)\partial_\zeta\gamma = [(1 + \beta_z^2\gamma^2)/\beta_z\gamma^2]\partial_\zeta\gamma = (\partial_\zeta\gamma)/\beta_z$

^{iv}The inverse statement also holds true and is probably more obvious: extrema of fluid momentum coincide with zero-crossings of the E -field—otherwise the electron would be accelerated or decelerated by the non-zero field and the momentum wouldn't be an extremum.

actual position of the plasma wave phase fronts will be shifted accordingly. When that shift is comparable to the the local radius of curvature, i.e. $\psi(r) \simeq \rho$, transverse wave breaking can destroy the regular structure of the plasma wave. Let $\psi(r)$ be perpendicular to the phase front derived above, the shifts can then be expressed as [34]

$$\begin{aligned} z' &= z + \psi(r)\rho/\sqrt{\rho^2 + r^2} \\ r' &= r - \psi(r)r/\sqrt{\rho^2 + r^2} \\ z &= r^2/2\rho. \end{aligned} \tag{3.46}$$

If the spatial dependence of ψ can be neglected, the model above predicts a swallowtail-shaped vortex for sufficiently large phase front shift, e.g. when $\psi_0/\rho = 1.5$, with ψ_0 being the on-axis shift; cf. the red line in Fig. 3.7 (a). In reality, the oscillation of fluid electrons should be stronger on-axis due to the higher local laser intensity. Approximating it with a Gaussian distribution, the phase front again self-intersects, though with a slightly different morphology; cf. Fig. 3.7 (b).

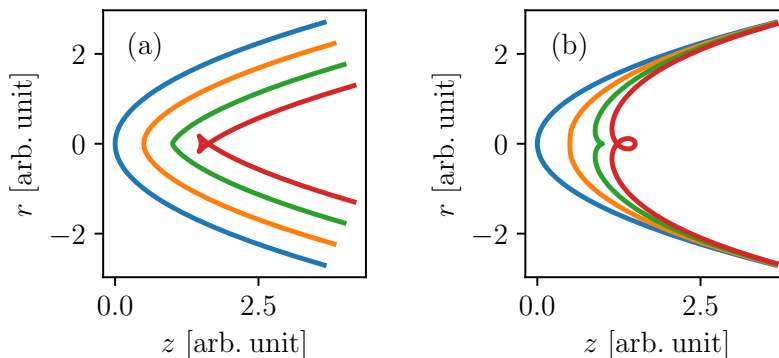


Figure 3.7: Schematic representation of 2D wave breaking scenarios. In panel (a) the phase front shift does not depend on r , whereas in (b) the shift follows a Gaussian function $\psi(r) = \psi_0 \exp(-r^2/2\rho^2)$. In both panels, from left to right, $\psi_0/\rho \in [0, 0.5, 1, 1.5]$

In both cases, a small amount of electrons may enter the wakefield from the transverse direction and get trapped and accelerated. As the oscillation amplitude ψ required for sheath crossing is smaller than the plasma wavelength ($\psi \simeq \rho \simeq \lambda_p/2$ assuming a spherical bubble; cf. Sec. 3.1.3), transverse wave breaking can happen at a lower wave amplitude than the longitudinal breaking introduced above. Hence it provides an effective mechanism for self-injection. In most experiments relying on self-injection to date, transverse wave breaking is the dominant injection mechanism.

When an electron is transversely injected into the wakefield, it will have a larger transverse momentum than longitudinally injected electrons [70]. Therefore it undergoes enhanced betatron oscillation and generates more radiation, rendering it an interesting X-ray source [26].

Due to its experimental simplicity, self-injection was the primary injection mechanism of laser plasma based particle acceleration experiments in their early stage [71, 72] and is still widely used to date [12, 73]. However, it has some drawbacks: First of all, electrons will be continuously injected into the wakefield once the wave-breaking initiates, which normally

leads to a broadband energy spectrum, whereas many accelerator applications call for mono-energetic electrons with per-cent level energy spread. It should be pointed out that when operating an LWFA in the highly nonlinear broken-wave regime [9], self-injection is able to produce to beams with monoenergetic features, which was experimentally demonstrated by three independent groups [74–76]. Reaching this regime usually relies on the nonlinear evolution of laser pulses in the plasma, which makes self-injection very sensitive to small parameter changes during the experiment hence lags behind in shot-to-shot stability and little can be done to control the process. These drawbacks make self-injection a less optimal option for a practical accelerator. The following section introduces controlled injection methods to address these issues.

3.4 Controlled injection schemes

Controlling the injection is of utmost importance for any accelerator development. Within the rapid progressing LWFA field, several methods of controlled injection aiming at improved beam quality have been proposed and experimentally demonstrated [13–25]. These methods are based on manipulating either the gas target—density tailoring and/or gas mixture—or the laser pulse(s). For the former, density down-ramp injection [13–17] and ionization injection [18–24] will be discussed in this section. For the latter, colliding pulse injection [25] will be briefly introduced.

3.4.1 Density down-ramp injection

As outlined in subsection 3.2, the trapping threshold is lower for a plasma wave with lower phase velocity. In a homogeneous plasma, the plasma wave phase velocity roughly equals the group velocity of the drive laser, which is essentially determined by the density of the plasma. Tailoring the density profile therefore offers a means to control the particle trapping conditions.

Injection in gradual down-ramp

Given a highly relativistic driver and 1D geometry, the phase of the wakefield can be expressed as $\Phi(z, t) = \zeta k_p(z)$ [13], where $\zeta \approx z - t$ and $k_p(z)$ contains only the explicit spatial dependence of the plasma wave number (or equivalently, the plasma frequency). As such, the instantaneous value of the local wave number $k(z, t) = \partial\Phi/\partial z$ is linked to the plasma frequency $\omega_p(z) = -\partial\Phi/\partial t$ via $\partial k/\partial t = -\partial\omega_p/\partial z$. The local phase velocity of the plasma wave can thus be deduced as

$$\beta_p(z) = \frac{\omega_p}{k} = \left(1 + \frac{\zeta}{k_p} \frac{\partial k_p}{\partial z}\right)^{-1}. \quad (3.47)$$

In a density down-ramp, $\partial k_p/\partial z < 0$, hence the plasma wave behind the driver ($\zeta < 0$) effectively slows down since $\beta_p < 1$. Injection takes place if the wakefield phase velocity is

slow enough to trap background electrons. When there is a long ($\gg \lambda_p$) and gradual ramp, electrons can get continuously injected, which results in a broadband energy spectrum as shown by Fig. 3.14 in section 3.8 and Refs. [14–16].

In a density up-ramp, the wake phase velocity is super-luminal ($\partial k_p / \partial z < 0$ and $\beta_p > 1$) hence injection is suppressed. Moreover, the plasma wave number decreases, or equivalently the plasma wavelength increases as a function of time. When the wave number decreases to near zero, the wavelength of plasma oscillation approaches infinity. As the wave number keeps on decreasing and becomes negative i.e. the absolute value of the wave number increases, an interesting effect of wake reversal will occur as reported by Zhang et al. [77, 78]; cf. section 5.4.

Shock front injection

Contrary to slow down-ramps, a sharp ($\lesssim \lambda_p$) downward density jump can lead to a qualitatively different injection process. As illustrated in Fig. 3.8, for a density profile containing two density plateaus with an abrupt change in between, the electron density peak formed in the high density region sits in the accelerating phase of the newly excited plasma wave in the low density region. Hence injection occurs very locally and a mono-energetic bunch can form. If the first plasma wave bucket is not strongly damped by the injected charge, shock front injection can also take place in the second wave bucket. As a result, dual bunches with a separation of $\sim \lambda_p$ can be generated [44].

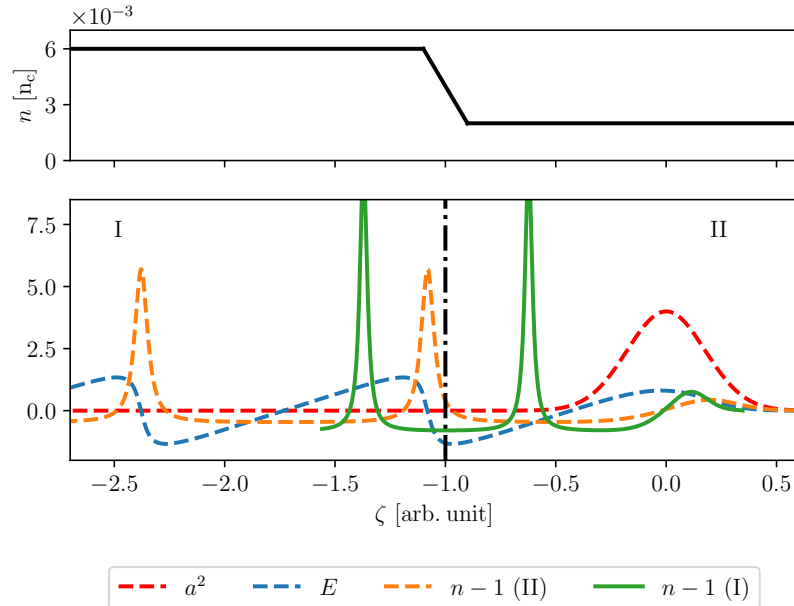


Figure 3.8: *Upper*: The assumed longitudinal density profile of the plasma target. *Lower*: The dashed lines represent quantities related to the plasma wave that can be generated after the density jump inside region II. The green solid line is for the normalized electron density distribution of the plasma wave formed in the high density region I. Due to the sudden change in plasma wavelength, the green density peaks can get trapped in the newly formed plasma wave and mono-energetic electron beams can be produced.

Such a sharp density jump can occur at the shock front produced by introducing an obstacle, e.g. a sharp razor blade or a silicon wafer as used in the experiments underlying this work, to a supersonic gas flow; c.f. Sec. 3.6.1. Consequently, this injection scheme is commonly referred to as shock front injection [17].

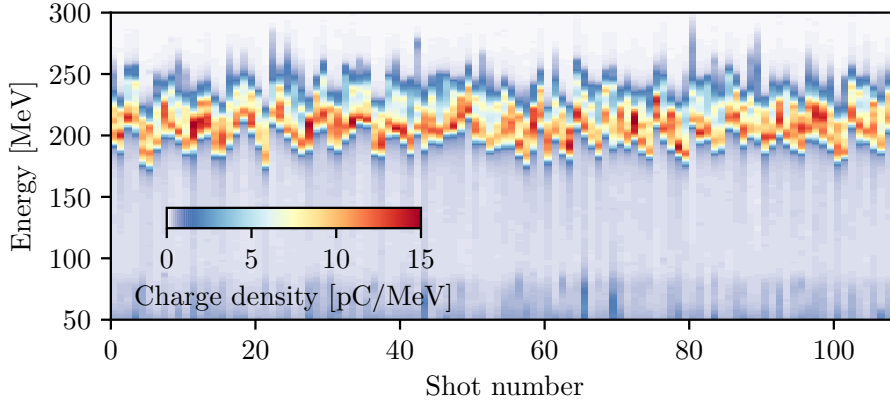


Figure 3.9: Demonstration of quasi-monoenergetic electron beams generated with a supersonic gas jet equipped with a silicon wafer as the shock front injector. By courtesy of J. Götzfried.

Figure 3.9 exemplifies the performance of properly set up shock front injection with electron spectra of 110 consecutive shots taken during the course of this thesis work. The spectral peak is around 200 MeV (limited only by the length of gas jet used for the experiment) and the charge density is well above 10 pC/MeV. This charge density is of a more than 5-fold increase compared to the self-injection data shown in Sec. 3.8, owing to the much narrower energy spread of a few percent. Interested readers are referred to J. Götzfried’s work [44] for more details.

Besides a high bunch quality, shock front injection offers energy and charge tunability. The beam energy can be easily controlled by altering the accelerator length; the bunch charge can be tuned by modifying the shock length and gradient—realized by properly positioning the blade/wafer for shock creation relative to the gas nozzle. With further refinements, shock front injection offers a promising path towards practical particle accelerators.

3.4.2 Ionization injection

Besides trapping electrons from the background plasma as required by self-injection and density down-ramp injection, one can also create electrons directly inside the wakefield. Thanks to the large difference in the ionization threshold between the inner and outer atomic shells of a high- Z gas, e.g. N_2 , its first ionization levels occur at the low intensity foot (typically below $10^{16} \text{ W cm}^{-2}$) of the drive laser to form the plasma wave. Only near the peak of the driver, the laser intensity is high enough to ionize the innermost shell. Via barrier suppression, an electron is born within the wakefield at ζ_{ion} , such that $a(\zeta_{\text{ion}}) \approx 0$, and $p(\zeta_{\text{ion}}) \approx 0$; cf. section 2.4. Therefore its Hamiltonian is simply

$$H_{\text{ion}} = 1 - \varphi(\zeta_{\text{ion}}). \quad (3.48)$$

Hence ionization injection requires a) $H_{\text{ion}} < H_{\text{sep}}$;^v cf. Fig. 3.5; and b) sufficiently high intensity. The phase space volume fulfilling simultaneously those two conditions affects the injected charge as well as the energy spread. Apparently, a larger injection volume leads to a higher charge and most likely a larger energy spread. That hints at two limitations of ionization injection: electrons will be continuously injected as long as the laser intensity remains above the ionization threshold; there can be multiple points within the drive pulse where the phase condition $H_{\text{ion}} < H_{\text{sep}}$ is fulfilled so that injection takes place in a sizable volume—both limit the achievable energy spread.

Experiments employing ionization injection typically use a gas mixture as plasma source, where the low- Z target gas, e.g. H_2 or He , is doped with a few percent of high- Z gas such as N_2 or Ar . In case a small energy spread is desired, the injection can be terminated by using a very short jet of mixed gas, in combination with an energy boosting stage of pure low- Z gas. Using a single stage of mixed gas, reduction of the injection volume can also be achieved by localizing the inner-shell ionization to a well-defined point. Quasi-mono-energetic spectra can be produced by engineering either the laser’s focusing geometry or its temporal profile. For the former, ionization self-truncates as the result of the interplay between the oscillation of an initially unmatched focus spot and over-loading of the wakefield [20–22]. For the latter, it has been proposed to use a counter-propagating ionization laser [23] or a co-propagating third harmonic wave [24] to create a sharp region where the threshold E -field for ionization is reached. These advanced ionization schemes employing multiple beams, yet to be experimentally demonstrated, promise high-quality bunches with percent-level energy spread and μm -level transverse emittance, making ionization injection an active area of research.

3.4.3 Colliding pulse injection

A counter-propagating laser can lead to injection not only by ionizing the gas mixture [23], but also by localized electron heating [25]. In the region where two pulses collide, their interference creates a standing beat wave with a node separation of half the laser wavelength, $\lambda_L/2$.^{vi} The ponderomotive force in the beat wave is hence on the order of $a_0 a_1 / \lambda_L$, where $a_{0,1}$ denotes the peak normalized vector potential of each pulse, in contrast to the single pulse’s ponderomotive force of the order $a_0^2 / c\tau$ with $c\tau$ being the pulse length. For the 30-fs-pulses used in this work, $c\tau \gg \lambda_L$ so the beat wave’s ponderomotive will be much larger than that of the driver when $a_1 \sim a_0$. This large ponderomotive force can preaccelerate the plasma electrons and effectively lower the trapping threshold.

Colliding pulse injection is experimentally demanding as it requires precise temporal ($\sim \text{fs}$) and spatial ($\sim \mu\text{m}$) overlap between two, or even more laser beams for more sophisticated collision schemes. Once these technical challenges have been overcome, the colliding pulse

^vA trapped electron has a smaller Hamiltonian than that of the separatrix, because the Hamiltonian corresponds to the sum of the kinetic energy with the potential energy that is negative valued for a trapped electron. This can also be understood when one considers an electron moving in the wakefield as an analogy to an electron moving in the Coulomb potential of an ion. A trapped electron is thus the counterpart of a bound electron whereas a fluid electron is the counterpart of a free/ionized electron.

^{vi}It is assumed here for simplicity that the two colliding laser pulses have equal wavelength. In general they can have different wavelengths so the node separation is the average of the two wavelengths and the beat note is determined by the wavelength difference.

3.4. Controlled injection schemes

injection scheme features several advantages: first, localized injection results in very narrow (< 10 per cent) energy spread and short (< 10 fs) electron bunch [25]; second, the injection position is prescribed by the collision point, offering a knob to tune the acceleration length hence the accelerator's energy output in a wide range (cf. Fig. 3.10); third, the colliding laser's intensity and focal spot size determine the injection volume, hence the charge and energy spread of the bunch can also be tuned; last but definitely not least, a wakefield accelerator with an colliding pulse injector can be turned into an all-optical Thomson scattering source offering photon energies tunable in the hard Xray to gamma ray range [27, 79], when electrons can be injected via a shock front injector, or a third injector beam.

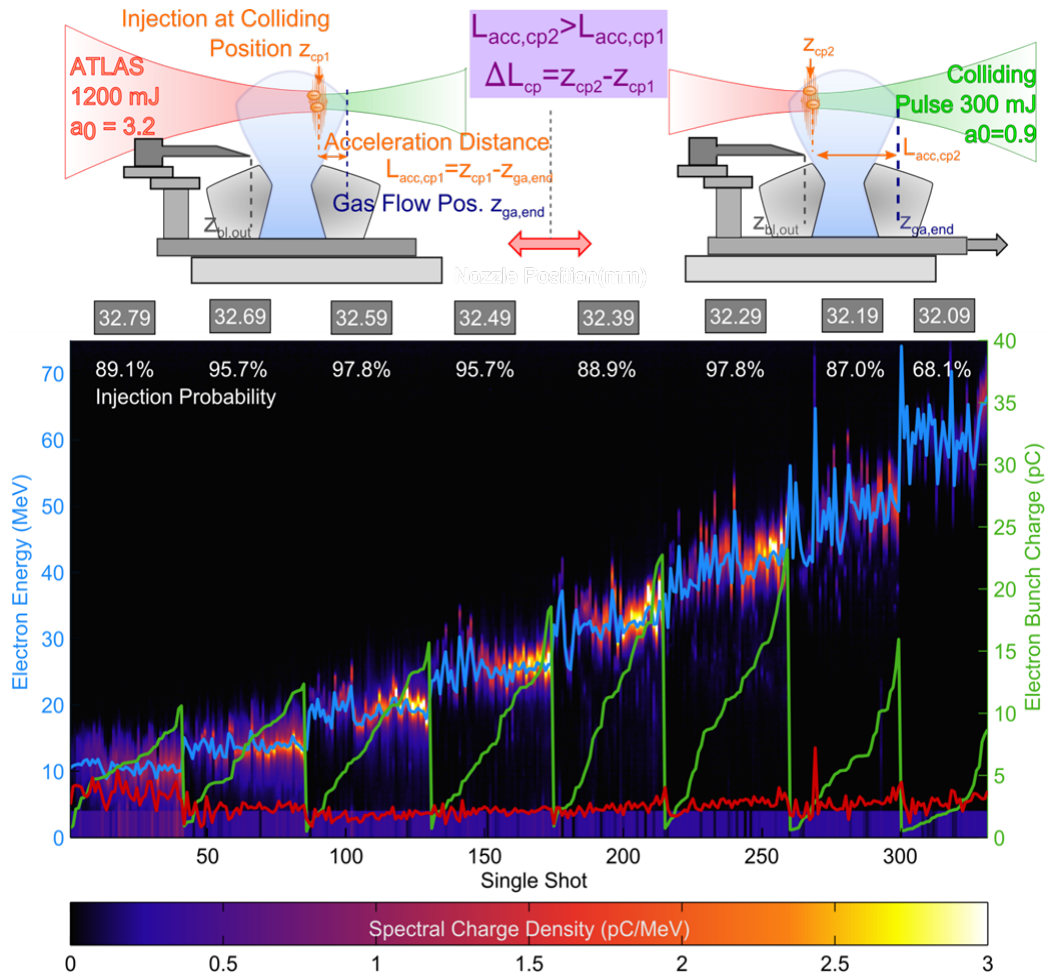


Figure 3.10: Illustration of colliding pulse injection. A scan of the collision position from 32.79 mm to 32.09 mm with a step size of 0.1 mm results in an increase of electron beam energy from 10 MeV to 60 MeV as shown by the blue line. An injection probability at 90%-level was achieved for all settings but the one with the highest energy. At each setting, the spectra are sorted according to the injected charge as indicated by the green curve. By courtesy of J. Wenz.

3.5 Acceleration limits and scalings

The research field of laser wakefield acceleration has seen tremendous development in the past few decades: methods for controlled injection introduced in the previous section dramatically improved the beam quality. Multi-GeV beams are routinely generated in laboratories around the globe. LWFA-based light and particle sources are seeing increasingly more applications. To achieve the overarching goal of energy-frontier colliders and make LWFAs more competitive for near-term applications, there are several limitations intrinsic to the LWFA process that must be addressed, which are usually summarized as three “D”s—depletion, dephasing, and diffraction. This section discusses these limitations and strategies to tackle them.

Depletion

During previous discussions of wakefield excitation, the drive laser’s evolution was neglected for simplicity. In reality, however, energy conservation demands a net energy transfer from the driver to the wakefield, and eventually to the injected electrons. Analysing the evolution of intense ($a \gg 1$) laser pulses in under-dense plasmas, Decker et al. [80] showed that nonlinear wakefield formation leads to a localized pump depletion—the driver’s head etches back at a velocity of $\beta_{\text{etch}} \simeq \omega_p^2/\omega_L^2$ while the tail propagates in the blow-out created by the head. Thus the laser energy depletes over a pump depletion length of

$$L_{\text{pd}} \simeq \frac{c\tau}{\beta_{\text{etch}}} \simeq \frac{\omega_L^2}{\omega_p^2} c\tau, \quad (3.49)$$

with $c\tau$ being the pulse length. Recall the conditions of the gas cell experiment presented in subsection ???: $c\tau \approx 9 \mu\text{m}$ and $n_e = 1.67 \times 10^{18} \text{cm}^{-3}$, corresponding to $\omega_L^2/\omega_p^2 \approx 1042$. A pump depletion length of $L_{\text{pd}} \approx 9.4 \text{mm}$ can be calculated, roughly equal to the dephasing length of $L_{\text{deph}} = 9.7 \text{mm}$.

Apparently, the pump depletion length is larger in lower-density plasmas ($L_{\text{pd}} \propto n_e^{-1}$), but so is the plasma wave phase velocity hence the injection threshold; cf. Sec. 3.2. Furthermore, a wider spot and longer pulse length—both meaning higher laser energy in a pulse for a given a_0 —are required at a lower density to resonantly drive the wakefield; cf. Secs. 3.1.2 & 3.1.3. One can therefore not indefinitely reduce the plasma density to extend the pump depletion length, as the ultimate limit is the total energy contained in the driver. With pulse energies at 100-J level readily available with contemporary fs-laser technologies and kJ-class on the horizon, a single-stage LWFA’s energy output can soon reach 10 GeV and beyond.

To reach even higher energy levels, e.g. TeV required by the HEP community, staging is probably the most viable path for LWFAs. Intriguing results on multi-stage coupling have blossomed in the literature [81, 82]. Another way to realize TeV electron beams is to use relativistic particle beams as the wakefield driver instead of lasers, which is a vibrant research field commonly referred to as (for historic reasons) plasma wakefield acceleration (PWFA). For example, the AWAKE collaboration at CERN uses the proton beam from the Super Proton Synchrotron (SPS), which contains 19 kJ of energy in the bunch.

Dephasing

An important consequence of pump depletion is that the plasma wave phase velocity β_p will be slower than the drive laser's linear group velocity $\beta_g = \eta$ by the amount of β_{etch} , namely,

$$\beta_p \simeq \eta - \beta_{\text{etch}} \simeq 1 - \frac{3 \omega_p^2}{2 \omega_L^2} \quad (3.50)$$

for a sufficiently under-dense plasma. In contrast, a highly relativistic electron bunch can move at almost the vacuum speed of light c . Therefore an electron bunch—initially injected at the back of the wakefield period—can gradually catch up with the driver and transition from the accelerating phase of the wakefield to the decelerating phase. The dephasing length L_{deph} is defined as the distance in the lab frame over which an electron can advance its wakefield phase to the dephasing point. Since only the rear half of a wake period is accelerating (Secs. 3.1.1 & 3.1.2), an estimate for the dephasing length L_{deph} can be give as [35]

$$L_{\text{deph}} = \frac{R_b}{1 - \beta_p} \simeq \frac{4 \omega_L^2 \sqrt{a_0}}{3 \omega_p^2 k_p}, \quad (3.51)$$

where $R_b \simeq 2\sqrt{a_0}/k_p$ denotes the bubble (blow-out) radius introduced in Sec. 3.1.3. Again, the dephasing length favors a low plasma density as $L_{\text{deph}} \propto n_e^{-3/2}$.

For an optimal LWFA performance, the acceleration length should be slightly larger than the dephasing length so that the phase space rotation leads to the minimum achievable energy spread. Imposing $L_{\text{pd}} \gtrsim L_{\text{deph}}$ results in $c\tau \gtrsim 2R_b/3$, complementing the resonant condition $c\tau \sim \lambda_p/2$ introduced in Sec. 3.1.2

Great efforts have been invested to battling dephasing. To name a few examples, a scheme for bunch rephasing has been proposed and demonstrated [83, 84], where the key element is a density up-ramp to shorten the bubble by locally increasing the plasma wave phase velocity—the exact opposite of density down-ramp injection outlined in Subsec. 3.4.1. This scheme can delay dephasing until acceleration is limited by other factors such as pump depletion or diffraction (details below), but it can not completely counteract dephasing as infinite plasma densities would eventually be required. Methods based on advanced optical design such as flying focus [85, 86] and axiprabola [87, 88] have attracted broad interest. Utilizing pulse front tilt, Debus et al. [89] proposed a propagating wave LWFA. Alternatively, a relativistic particle beam driver can be used instead of a laser driver.

Diffraction

Another limiting factor arising from a laser driver is natural diffraction. Assuming a laser pulse with transverse Gaussian intensity profile propagating in a uniform plasma, the spot size evolves as [8]

$$\frac{w^2(z)}{w_0^2} = 1 + \left(1 - \frac{P}{P_c}\right) \frac{z^2}{z_R^2}, \quad (3.52)$$

where $z_R = \pi w_0^2/\lambda_L$ is the Rayleigh range (Subsec. 2.1.2), and P_c is the critical power for relativistic self-focusing (Subsec. 2.6.1). Hence $P \gtrsim P_c$ is required so that self-focusing can

maintain the relativistic intensity over the acceleration length, which poses a lower bound for the plasma density. More specifically, Lu et al. [35] showed that stable self-guiding requires $a_0 \sim (\omega_L^2/\omega_p^2)^{1/5}$.

When external guiding is employed an even lower density can be used and the acceleration will then be limited by depletion or dephasing.

3.6 Experimental arrangement

Experimental study of laser wakefield acceleration (LWFA) requires various instruments. At the very least, one needs a suitable laser system as the driver, a plasma (or neutral gas) source as the target. Figure 3.11 depicts a schematic of the experimental setup used during the measurement campaign underlying this work. Inside an 8-m-long vacuum chamber, laser pulses from the ATLAS laser system (Sec. 3.7) are focused with an off-axis parabolic (OAP) mirror into a gas target, e.g. a supersonic jet with a shock front injector (Sec. 3.6.1) or a varying-length cell. As the laser pulses propagate, they excite plasma waves where electrons can get trapped and accelerated.

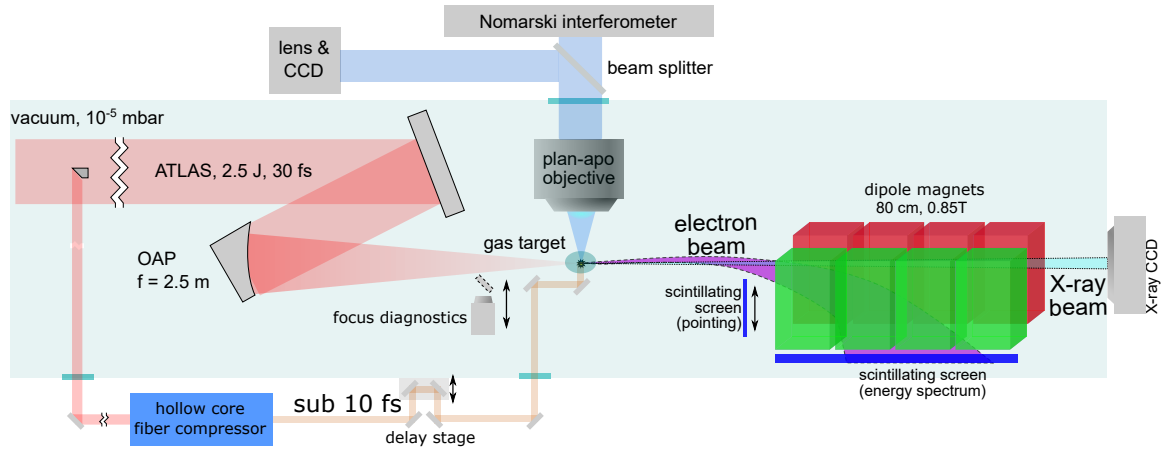


Figure 3.11: Schematic overview of experimental setup. By courtesy of M. F. Gilljohann.

3.6.1 Supersonic gas jet with shockfront injector

A popular choice of target for LWFA experiments is de Laval (converging-diverging) nozzles, because they allow formation of gas jets with desired shape (a few-mm-long density plateau, with sharp rising/falling edges) and density ($\sim 10^{18} \text{ cm}^{-3}$) with relatively simple and robust setup. The open geometry also makes diagnostic access straight forward. All experimental results presented in this thesis were obtained with de Laval nozzles, with the only exception of those presented in Sec. 3.8 where a gas cell was used. For the nozzles used in this work, Hütter [90] carried out the design and characterization during his master thesis, which also forms the basis of this subsection.

3.6. Experimental arrangement

The gas jet produced by such a nozzle is usually modelled as an isentropic flow. The relation between the flow's Mach number M and its cross-sectional area A can be given as

$$\frac{dM}{dA} = \frac{M \left(1 + \frac{\kappa - 1}{2} M^2 \right)}{A(M^2 - 1)}, \quad (3.53)$$

where $\kappa = C_p/C_V$ is ratio of the specific heat for constant pressure over that for constant volume, which amounts $\kappa = 5/3$ for monoatomic gases and $\kappa = 7/5$ for diatomic gases. Since $\kappa > 1$, $A > 0$, and $M > 0$, the sign of this derivative is purely determined by the sign of $M^2 - 1$. That is, for a subsonic flow ($M < 1$) the stream velocity decreases with the increase of the area. On the contrary, a supersonic flow accelerates with a larger area. In a de Laval nozzle, the cross section first converges to a minimum, the so-called throat, where the initially subsonic gas flow accelerates until it becomes sonic and locally choked. A supersonic flow is then generated in the diverging segment of the nozzle.

To reach the desired gas density at the nozzle exit, the required nozzle geometry can be deduced from the stagnation ratios

$$\frac{T}{T_0} = \left(1 + \frac{\kappa - 1}{2} M^2 \right)^{-1} \quad (3.54)$$

$$\frac{\rho}{\rho_0} = \left(1 + \frac{\kappa - 1}{2} M^2 \right)^{\kappa - 1} \quad (3.55)$$

$$\frac{p}{p_0} = \left(1 + \frac{\kappa - 1}{2} M^2 \right)^{\frac{\kappa - 1}{\kappa}} \quad (3.56)$$

$$\frac{A}{A^*} = \frac{1}{M} \left(\frac{2}{\kappa + 1} + \frac{\kappa - 1}{\kappa + 1} M^2 \right)^{\frac{\kappa + 1}{2(\kappa - 1)}} \quad (3.57)$$

where T denotes the temperature, ρ the density, and p the pressure. The subscript 0 indicates the initial condition at the nozzle inlet, and the asterisk is for the condition at the throat.

Disturbance of a supersonic flow leads to shock formation. A normal shock is a sharp change of the gas properties along the flow, with an extremely thin interface perpendicular to the flow direction. The flow's Mach number immediately before (denoted with subscript 1) and after (denoted with subscript 2) the shock are linked via

$$M_2^2 = \frac{(\kappa - 1)M_1^2 + 2}{2\kappa M_1^2 - (\kappa - 1)}. \quad (3.58)$$

It can be shown that $M_2 < 1$ when $M_1 > 1$,^{vii} namely, a shock wave always turns a supersonic flow into a subsonic one. Relation for the densities can be given in terms of M_1 as

$$\frac{\rho_2}{\rho_1} = \frac{(\kappa + 1)M_1^2}{2 + (\kappa - 1)M_1^2}. \quad (3.59)$$

Hence the density increases after the shock.^{viii}

^{vii} $M_2^2 - 1 = (\kappa + 1)(1 - M_1^2)/[2\kappa M_1^2 - (\kappa - 1)] < 0$

^{viii} $\rho_2/\rho_1 - 1 = 2(M_1^2 - 1)/[2 + (\kappa - 1)M_1^2] > 0$

Inserting an obstacle into a supersonic gas flow leads to formation of an oblique shock, which not only brakes but also deflects the flow. Let δ denote the deflection angle, and β the shock wave angle; cf. Fig. 3.12. The flow velocities' parallel (to the shock wave) component is conserved across the oblique shock, and the perpendicular (with respect to the shock wave) components, i.e. $M_{1\perp} = M_1 \sin \beta$ and $M_{2\perp} = M_2 \sin(\beta - \delta)$, follow equation (3.58).

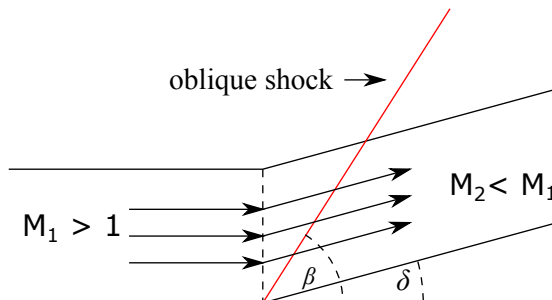


Figure 3.12: Illustration of an oblique shock. By courtesy of M. Hüther.

3.7 ATLAS-300 laser system

Looking back to the history of laser driven particle accelerators, milestones are often reached accompanied by breakthroughs in the laser technology. It is no exception that this work emerged from an upgrade of the laser. The Advanced Titanium:sapphire LASer system, ATLAS for short, has been driving the development of the high-field laser physics at the Max-Planck-Institute for quantum optics over the past decades. In 2013 it was relocated to the Laboratory for EXtreme photonics (LEX) and upgraded to a specified peak power of 300 TW (detailed in the master's thesis of Günther [91]). To reach such a high peak power, ATLAS utilizes the principle of chirped pulse amplification (CPA) [7].

As shown in figure 3.13, a pulse train is generated in the passively Kerr-lens mode-locked Ti:sapphire oscillator (FEMTOLASERS SYNERGYTM) with an initial pulse duration below 10 fs. For further amplification, the repetition rate is reduced from 70 MHz to 10 Hz by a pulse picker Pockels cell. An Öffer type grating stretcher stretches the pulse duration to about 300 ps. In the stretcher, a programmable acoustic optical modulator (FASTLITE, DAZZLERTM) is installed to fine-tune the spectral phase up to the fourth order. The stretched pulses are then amplified in a regenerative amplifier where the spectrum will be shaped by another programmable acoustic optical modulator (FASTLITE, MAZZLERTM). This spectral shaping will pre-compensate the spectral gain narrowing in the regenerative amplifier and the gain shifting in the power amplifiers. As a result, the FWHM bandwidth is larger than 50 nm at the end of the power amplifier chain, centered around 800 nm.

One major challenge in operating such a high-power laser system lies in damage prevention. A top-hat beam profile^{ix} is therefore preferred over a Gaussian intensity profile, as it allows for more energy in the beam for the same peak fluence on the optics. For practical reasons,

^{ix}The intensity distribution of a top-hat beam is usually modeled with a super-Gaussian function of order n , i.e. $I(r) = I_{\text{peak}} \exp[-2(\frac{r}{w})^n]$.

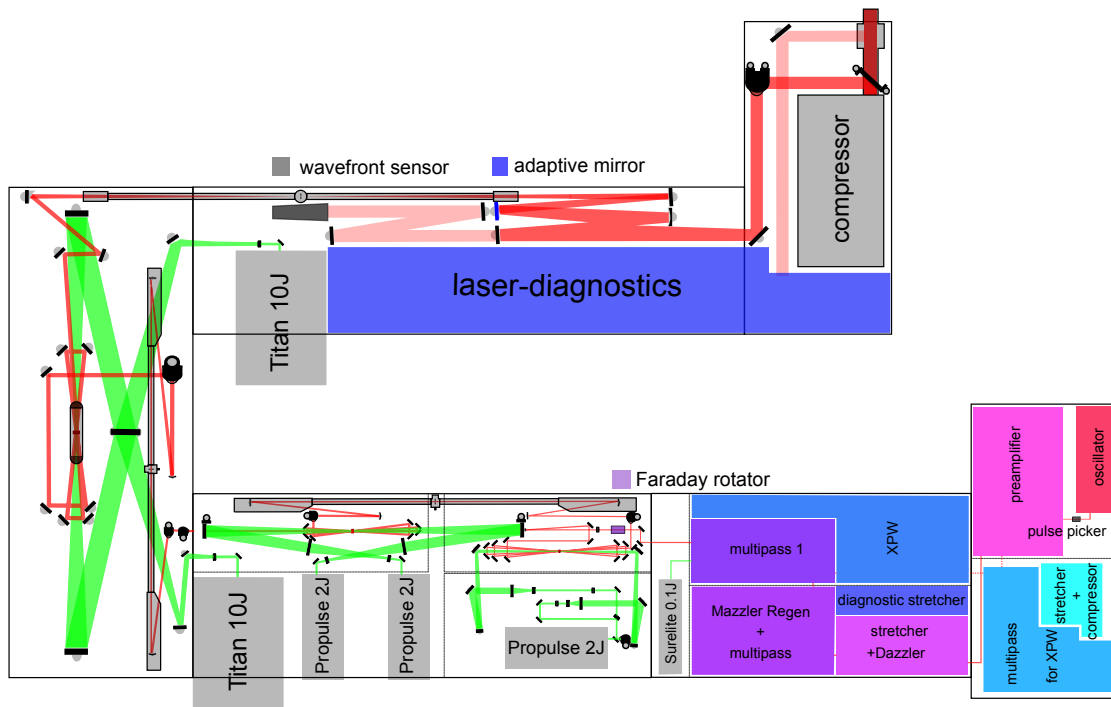


Figure 3.13: Schematic of ATLAS 300 layout. By courtesy of B. Günther.

the beam size is usually kept as small as possible, and the optics are often used near their damage threshold. Deterioration of the beam quality, such as hot spots in the beam, may therefore lead to damage of the optical surfaces. In order to minimize the chance of damage, the ATLAS system design incorporated spatial filters in between each two power amplifier stages, which homogenize the beam near-field profile.

With the limited laser energy available, the highest possible intensity is reached when the pulses have a flat wavefront (spatial phase) as well as a clean temporal structure (spectral phase) before the final focusing. Similar to the Dazzler that corrects the spectral phase, the wavefront aberrations can be mitigated with a close-looped adaptive optics system. The combination of a deformable mirror based on piezoceramics (AKA Optics SAS Bimorph) and a wavefront sensor based on quadriwave lateral shearing interferometry (PHASICS S.A SID4) was employed for that purpose.

Only measured properties can be optimized, therefore various laser pulse diagnostics were implemented after the compressor, such as a spectral interferometer with crossed polarized wave generation (FASTLITE Wizzler) and a second-harmonic-generation-based frequency-resolved optical gating (SHG-FROG) device (Swamp Optics GRENOUILLE) for the pulse duration, a third-order crosscorrelator (Amplitude Technologies Sequoia) for the temporal intensity contrast, and an inverted field autocorrelator (internal name Prezelator) for the pulse-front tilt.

3.8 LWFA experiment with variable-length gas cell

As outlined in section 3.3, driving a wakefield to the wave-breaking limit allows for self-injection of electrons into the wakefield. In an experiment employing a hydrogen-filled variable-length gas cell as the plasma source, electron beams with energies in the GeV range were generated; see dissertation of Chou [92] for details of the gas cell setup. Figure 3.14 depicts the evolution of electron energy spectrum (cf. Sec. 4.2 for the magnetic spectrometer) as the the gas cell length increases. The spectra feature two peaks: the peak with higher energy emerges from wave breaking induced self-injection, and its energy depends sensitively on the gas cell length; in contrast, the lower energy peak below 200 MeV is most likely explained by the injection at the down-ramp (Subsec. 3.4.1) at the very end of the gas cell, as its energy is almost independent of the gas cell length over a wide range from 4 mm to 8 mm (detailed below).

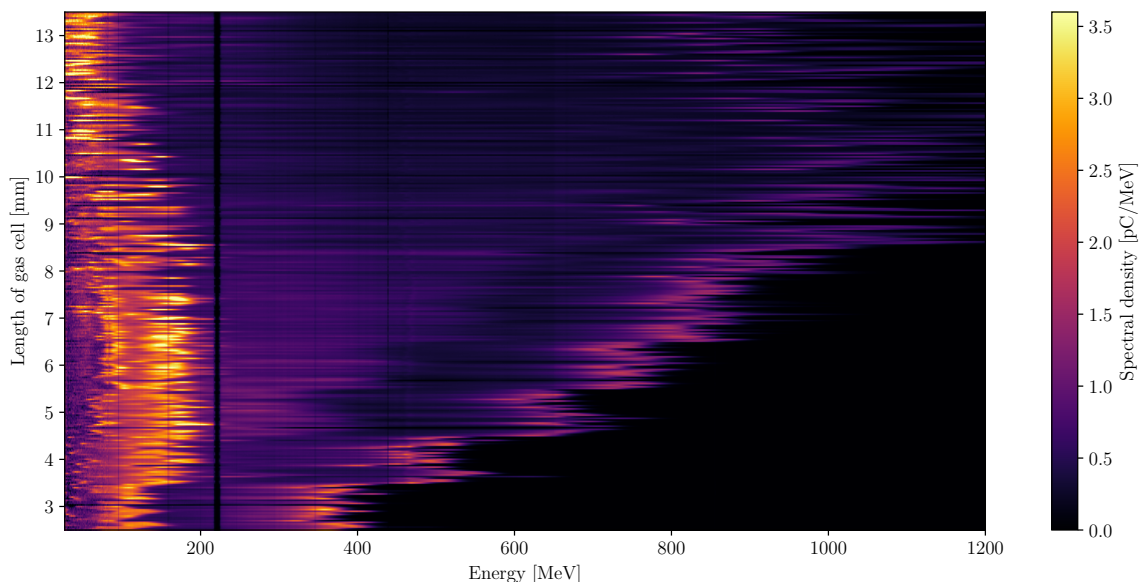


Figure 3.14: Evolution of the electron spectrum as the gas cell length increases from 3 mm to 13 mm with a step of 1 mm. Each horizontal slice is an angle-integrated single-shot spectrum measured with the magnetic spectrometer described in Sec. 4.2. Each cell length contains 30 shots. The high-energy peak, resulted from self-injection, is accelerated from about 0.4 GeV (~ 3 mm cell length) to over 1 GeV when the cell length exceeds 10 mm. The low-energy peak below 200 MeV, hypothetically injected at the gas-cell’s exit down ramp, is less influenced by the gas cell length. The black strip near 200 MeV is not covered by the imaging camera; other black vertical lines are markers on the scintillating screen for imaging calibration. The data were taken on May-25-2016.

Properties of the high energy peak, such as its central energy, energy spread, and the charge contained in the peak, of each spectrum are extracted from a skewed Gaussian fit. Evolution of the peak energy can be well described by a parabolic model as shown in Fig. 3.15, implying that the acceleration process is limited by dephasing (cf. Sec. 3.5). Extrapolating the fitting curve to zero energy results in an injection position at 1.1 mm and a maximum acceleration gradient of 210.8 GeV/m. It can be inferred that the maximum energy of 1025.3 MeV is achieved at 10.8 mm, corresponding to a dephasing length of 9.7 mm. According to the

Lu-scaling [35] for the dephasing length L_{deph} and maximum energy \mathcal{E} (cf. Sec. 3.5):

$$L_{\text{deph}} = \frac{4 \omega_L^2 \sqrt{a_0}}{3 \omega_p^2 k_p} = 9.7 \text{ mm} \quad (3.60)$$

$$\frac{\mathcal{E}}{m_e c^2} = \frac{2 \omega_L^2}{3 \omega_p^2} a_0 = \frac{1025.3 \text{ MeV}}{511 \text{ keV}}, \quad (3.61)$$

an electron density of $1.67 \times 10^{18} \text{ cm}^{-3}$ can be deduced along with an a_0 of 2.94.

For reference, the ideal gas law predicts a H_2 density of $3.2 \times 10^{18} \text{ cm}^{-3}$ for the gas cell filling pressure of 130 mbar (measured at the valve) at a room temperature of 20°C . The gas density in the cell is as such roughly a quarter of the density at the valve assuming fully ionized H_2 , in good agreement with the OpenFOAM 3D fluid dynamics simulation performed by Chou [92]. Based on this density estimation, the 1D cold wave-breaking field should be 124.2 GeV/m . The acceleration gradient deduced from the high-energy peak, 210.8 GeV/m , is therefore 1.79, $\sim \sqrt{a_0}$, times the 1D cold wave-breaking field. Furthermore, this density estimate requires a matched laser strength of $a_m \simeq (P/P_c)^{1/3} \approx 3.14$, which agrees reasonably well with the value of 2.94 deduced from the high-energy peak. This self-consistency confirms that the LWFA is operated in the bubble regime [9, 35] during this campaign. A matched spot size of $r_m \simeq 2\sqrt{a_m}/k_p \approx 15.1 \mu\text{m}$, which ensures stable laser propagation, can be reached by relativistic self-focusing in the plasma prior to the injection point at 1.1 mm.

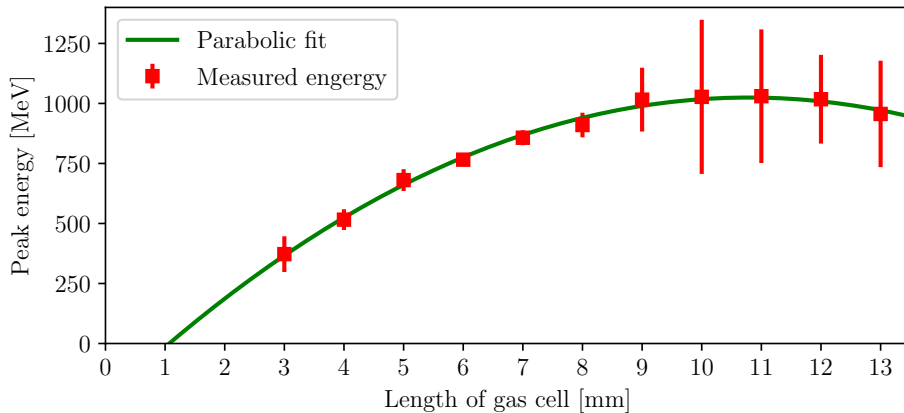


Figure 3.15: Analyses of the high energy peak in figure 3.14. Each data point is an average of 30 consecutive shots; error bars represent the standard deviation.

Figure 3.16 depicts the evolution of charge and total beam energy in the high energy peak and the whole beam. There are several features worth noting:

- about 40% of the charge in the high-energy peak gets lost when lengthening the cell from 3 mm to 5 mm, whereas the total bunch charge keeps increasing until 7 mm of cell length. It is hypothesized that this charge loss is due to the wakefield evolution caused by the strong drive laser leaving the plasma before diffraction or depletion could sufficiently reduce the driver intensity. This hypothesis is complemented by the energy boost of the down-ramp injection at the end of the gas cell, i.e. the low energy part

of the spectrum. The apparent increase in the total beam charge can be attributed to the low-energy beam being accelerated to above the magnetic spectrometer's detection limit of 20 MeV.

- after 7 mm of propagation, the total charge in the bunch (above 20 MeV) drops, while the peak charge remains a constant, indicating that the down-ramp injection becomes less effective. This ineffectiveness could be either a decreased chance of injection, or a weaker accelerating field hence less charge above 20 MeV and more lower-energy charge—both of which can be linked to the reduction in driver intensity due to diffraction and depletion.
- the stagnation of total bunch energy is probably due to the cancellation between the charge reduction and energy gain of individual electrons.
- around the dephasing point of 11 mm, roughly one fifth of the laser energy (~ 1.5 J within the first Airy disk) is transferred to the electron bunch, of which about 45% is in the high-energy peak, i.e. 9% of the clean laser energy is in the high-energy bunch.
- the highest efficiency of energy transfer occurs at 9 mm for both the peak and the whole bunch

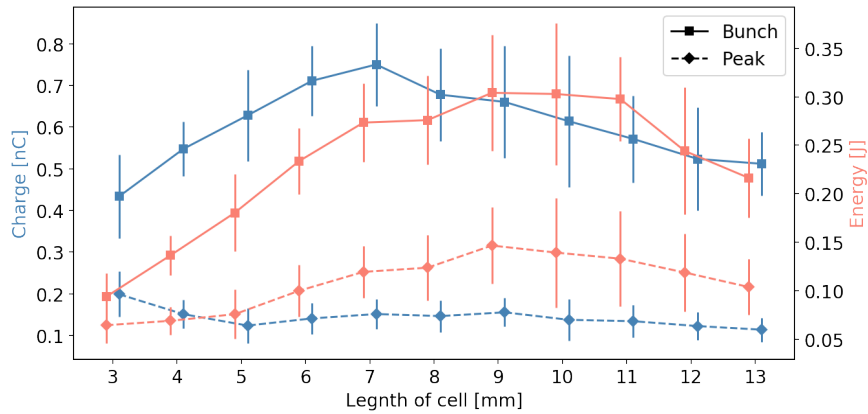


Figure 3.16: Evolution of the charge and total energy contained in the high energy peak and the whole bunch. Bunch charge and energy are inferred from a skewed Gaussian fit for the high-energy peak, whereas for the low-energy part a direct integration of the spectrum is used instead. The lines are only to guide the eye and error bars represent standard deviation.

4 Basic Diagnostics

The non-linear nature of its dynamics, as well as the limited precision of knowledge and control over experimental conditions often render a laser wakefield accelerator (LWFA) a black box. To shed some light into this black box and monitor the performance of an LWFA, diagnostic tools for key experimental parameters are indispensable. There exist many established diagnostic techniques in the radio-frequency (RF) accelerator community, but they are usually not suitable for LWFAs for the following reasons. First, typical beam parameters of LWFAs are of a different order of magnitude. For example, the micrometer-scale structure of a plasma wave limits the maximal possible bunch size in both transverse and longitudinal directions, which calls for bunch diagnostics with much higher spatial (μm) and temporal (fs) resolution; the large bunch energy spread, sometimes up to 100%, requires spectrometers with a large energy coverage. Second, contrary to the quasi-stationary accelerating structure in RF accelerators, the driver pulses and consequently the plasma waves they excite can evolve significantly during the LWFA process, meaning the diagnostics should offer time-resolved information on the time scale of plasma oscillation (~ 10 fs). Moreover, the interaction between a high-intensity laser pulse and a plasma creates a harsh electro-magnetic environment, which, many conventional electronic detectors cannot withstand. As a result, the LWFA community has developed a new set of tools. This chapter gives an introduction to some commonly used basic diagnostics for LWFAs alongside a brief discussion of their strengths and limitations.

4.1 Scintillating screen

The arguably simplest beam diagnostic is a scintillating screen imaged onto a camera. When hit by energetic electrons or X-ray photons, phosphorescent compounds in the screen absorb a tiny amount ($\sim \text{keV}$ per relativistic electron) of energy and emit scintillation photons over a typical decay time of milliseconds. Simulations and measurements have shown that the deposition in the phosphor layer is almost independent of the kinetic energy for incident electrons that are more energetic than 3 MeV [93]. As will be shown in subsection 4.1.1, the number of emitted photons is proportional to the impinging charge over a wide range. Hence the scintillation intensity distribution directly reflects the pointing and transverse profile of the electron beam.

Besides pointing and beam profile, the bunch charge is another important beam characteristic that can be measured with scintillating screens, if the intrinsic response of the screens and the geometry is known. The latter includes the distance from the camera to the screen,

the f-number of the imaging optics, the observation angle etc. In the remaining part of this section, methods for quantifying those aspects will be discussed.

4.1.1 Absolute calibration of scintillating screens

Scintillating screens are widely used in cassettes for clinical X-ray radiography purposes, but their efficiency as an electron detector is usually not quantitatively investigated by the manufacturer. The efficiency of different screens models can vary dramatically, depending on the type and concentration of phosphor, as well as the material and thickness of the cladding. Dozens of models have been used by different labs due to the variety of brands and accelerator parameters, among which the efficiency of many are unknown yet. For that reason, many groups using them for LWFA acceleration research still put arbitrary units to the charge axis.

Within the LWFA community, a handful of attempts [93–97] have been made to determine the intrinsic efficiency of scintillating screens. Those measurements were usually performed with well characterized electron sources such as an RF accelerator, whose public access is very limited. In an effort to improve that situation, we recently characterized the electron response several popular types of screens and proposed methods for cross-laboratory implementation of the results Kurz et al. [96]. That series of calibration measurements were carried out at Helmholtz Zentrum Dresden Rossendorf (HZDR) using the Electron Linac for beams with high Brilliance and low Emittance (ELBE) linear accelerator (linac). While this campaign was headed by me, the main results have been described as part of the Master Thesis by Thomas Kurz whom I supervised at the beginning of his thesis, therefore I will just summarize the most important results here.

The ELBE linac can generate sub-10 ps electron pulses at 13 MHz repetition rate. Alternatively, it can operate in a pulse train mode, delivering trains consisting of a variable number of 77-ns-spaced pulses, at a repetition rate of up to 1000 trains per second. The charge of each individual bunch is tunable up to 80 pC and the bunch energy is tunable up to 40 MeV. Despite the fact that this energy is far below the typical energy delivered by an LWFA, the energy independence of the response [93] should still give correct calibration values .

During the campaign for absolute charge calibration, the length of the 23.5 MeV, 1 Hz pulse train was varied from 1 to 1400 pulses, as detailed in Ref. [96]. The charge in each pulse was set to 15 pC, resulting in a total charge range of 15 pC to 21 nC per train. Note that the duration of the longest pulse train, $\sim 0.1 \mu\text{s}$, remained well below the $\sim \text{ms}$ decay time of scintillation screens.

Figure 4.1 depicts the setup employed for the measurement. Inside a vessel that was directly connected to the accelerator vacuum, electron beams provided by the ELBE linac were focused by quadruple magnets to a nearly Gaussian spot with an area of $\sim 2 \text{ mm}^2$. An integrating current transformer (Bergoz ICT-082-070-05:1-VAC) recorded the charge of each individual shot. Six types of screens were mounted on a target wheel at an angle of $\varphi = 22(1)^\circ$ relative to the electron beam axis and imaged with a C-mount telephoto-lens (Ricoh FL-CC6Z1218A-VG) onto a charge coupled device (CCD) camera (Basler acA1300-30gm) under normal viewing angle. For the purpose of cross-calibration, a gaseous tritium light source

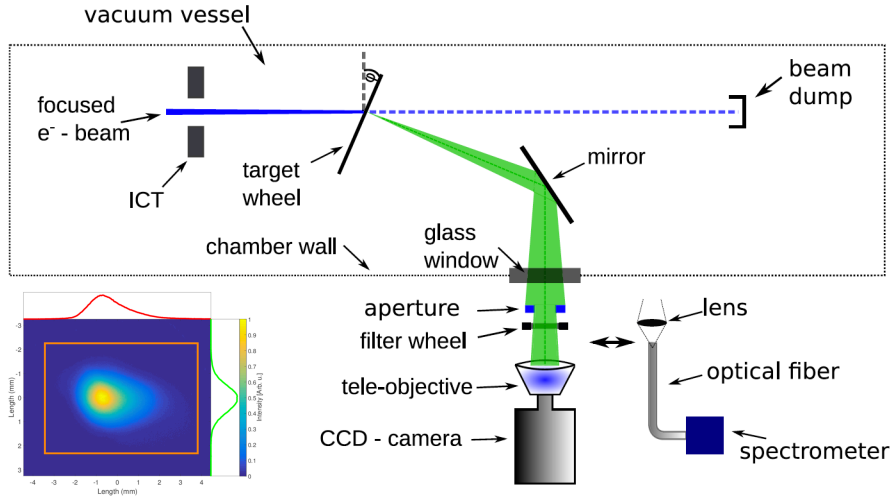


Figure 4.1: Setup for absolute calibration of scintillating screens. *Inset:* A representative e-beam profile recorded with the camera, with horizontal and vertical lineouts through the peak. By courtesy of T. Kurz, figure reproduced from Ref. [96] with permission of the author.

was also mounted on the target wheel; cf. subsection 4.1.2. The wheel angle was chosen so that the pick-off mirror can be mounted off-axis, while still collecting the light emitted normal to the screen’s surface. The arrangement was chosen in order to prevent the detection of optical transition radiation from the screen or from the mirror, which would be generated if the electron beam intersected the mirror. In order to record a sufficient dynamic range, a set of calibrated neutral-density filters with optical densities ranging from 0.5 to 4.0 could be placed before the camera. The effective collection angle was $3.18(7)$ msr, defined by an aperture with a diameter of $22.96(5)$ mm, situated $361(4)$ mm from the target in front of the objective. Thanks to the small solid angle, the lateral variation of the signal can be ignored. A fiber-coupled spectrometer (Ocean optics HR4000) can be put in position of the camera, as the spectra are required when determining the spectral throughput of the optical system and the quantum efficiency of the CCD chip.

The absolute calibration of a scintillating screen C_{scint} , i.e. the photon number N_{ph} emitted into solid angle Ω upon incidence of charge Q , can thus be given as

$$C_{\text{scint}} = \frac{N_{\text{ph}}}{Q\Omega} = \frac{N_{\text{CCD}} \cos \varphi}{Q\Omega\eta_{\text{total}}}. \quad (4.1)$$

Here N_{CCD} denotes the total counts within the region of interest of the background-corrected CCD image. The factor of $\cos \varphi$ accounts for the increase of effective interaction length due to the incidence angle of electron beam. The total light collection efficiency η_{total} takes into account the 97(1) % reflection of the off-axis mirror, the 91.3(5) % transmission of the vacuum window, the 88(1) % throughput of the objective, and the 32.8(17) % photon-to-count conversion efficiency of the CCD chip (Sony ICX445) that combines the photon-to-electron quantum efficiency and the loss of the readout electronics.

The absolute photon yield is shown in Fig. 4.2. Up to a peak charge density of $\sim \text{nC mm}^{-2}$ the response of the measured screens remains linear. A linear fit to the data results in cali-

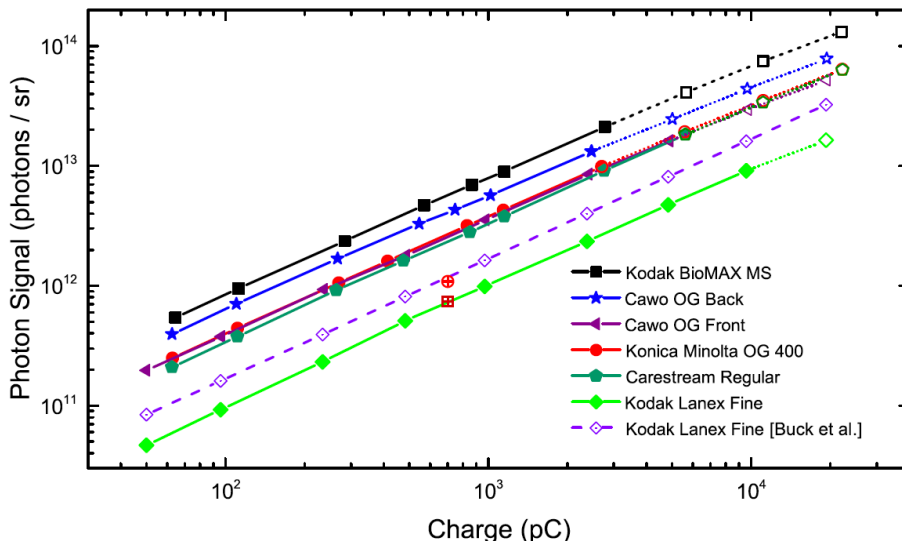


Figure 4.2: Absolute calibration of various types of scintillating screens. The solid line and filled markers of each calibration curve indicate the linear region, whereas the dotted line and open markers show the non-linear part. For comparison with other published results on Kodak Lanex Fine, the red square is deduced from experimental data in Glinec et al. [93]. The dashed line and red circle are reproduced from Buck et al. [94], where the value of red circle is based on the Monte Carlo simulation reported in [93]. By courtesy of T. Kurz, figure reproduced from [96] with permission of the author.

bration factors listed in Tab. 4.1. Note that only data points with less than -10% deviation from the linear model (indicated by filled markers) are considered, because saturation and degeneration effects [96] occur for higher peak charge densities. A model following the Birks' law

$$\rho_{\text{scint}} = \frac{\rho_{\text{ICT}}}{1 + B\rho_{\text{ICT}}} \quad (4.2)$$

describes this saturation behaviour, with the Birks' constant B as the free parameter. The variable ρ_{ICT} denotes the peak charge density derived from the bunch charge measured by the ICT and the beam profile recorded in the linear regime assuming a charge-independent beam shape. ρ_{scint} is obtained from the saturated beam profile on the scintillator using the absolute calibration C_{scint} . A saturation threshold ρ_{sat} is deliberately defined at 90% level, cf. Tab. 4.1, that is, the scintillation signal drops to 90% of the prediction by the linear model when $\rho_{\text{ICT}} = \rho_{\text{sat}}$. This choice of the threshold ensures a clear separation between saturation effects and the statistical fluctuation in the linear regime. The saturation effect observed in the calibration campaign does not play an important role for the $\sim 100 \text{ pC/mm}^2$ of charge densities relevant in this work; cf. Fig. 4.4. However, in future wakefield acceleration experiments e.g. those planned for CALA where charge densities above nC/mm^2 can be anticipated, saturation may eventually leads to underestimate of the charge determined from scintillating screens.

A final remark of this subsection: the scintillating screens are often packaged in pairs, with one screen intended for the front side of the radiographic cassette and the other back. The front screen has usually a higher spatial resolution and a lower light yield compared to the back one. For instance, the front screen of the CAWO OG 16 set used for this work is only

4.1. Scintillating screen

about 64% as efficient as the back screen; cf. Tab.4.1. A factor-of-1.5 error in electron beam charge would occur if a front screen is mistaken for a back one or vice versa.

Screen	Abs. calibration [10^9 ph/sr/pC]	Sat. threshold [nC/mm ²]	Birks' constant [10^{-5} mm ² /pC]
Kodak BioMAX MS	7.6 ± 1.3	1.6 ± 0.2	7.1 ± 0.8
CAWO OG 16 Back	5.8 ± 1.0	1.8 ± 0.2	6.0 ± 0.6
CAWO OG 16 Front	3.7 ± 0.7	1.8 ± 0.2	6.1 ± 0.7
Konica Minolta OG 400	3.7 ± 0.7	1.9 ± 0.2	5.8 ± 0.6
Carestream Lanex Regular B	3.1 ± 0.6	1.9 ± 0.2	5.9 ± 0.6
Kodak Lanex Fine	1.0 ± 0.2	3.5 ± 0.3	3.1 ± 0.4

Table 4.1: Absolute calibration, saturation threshold, and Birks' constant of some commonly used scintillating screens. The annotations "front" and "back" for CAWO OG 16, and "B" for Carestream Lanex Regular indicate the two screens from the same package are different. Values are drawn from the data presented in Fig. 4.2; cf. main text.

4.1.2 Cross-calibration with constant light source

Implementing absolute calibration results requires careful characterization of the imaging geometry, which is rather impractical to perform on a daily bases, especially when the geometry of setup is frequently modified to fit the goal of each experiment day. It would be therefore desirable to eliminate the geometric dependence of the detector signal.

This subsection introduces a method of cross-calibration originally proposed by Buck et al. [94], where a constant light source (CLS) serves as the reference, and the bunch charge Q is simply deduced from the background-corrected CCD image as

$$Q = \frac{N_{e\text{-beam}}}{N_{\text{CLS}}} \times C_{\text{cross}}, \quad (4.3)$$

where $N_{e\text{-beam}}$ denotes the total counts caused by the electron beam and N_{CLS} the integrated counts of the CLS. The cross-calibration factor

$$C_{\text{cross}} = \frac{I_{\text{CLS}} \times t_{\text{exposure}}}{C_{\text{scint}}} \quad (4.4)$$

depends on the CLS's radiant intensity I_{CLS} , i.e. number of photons emitted into a unit solid angle per unit time, the exposure time of the camera t_{exposure} , and of course, the intrinsic efficiency of the deployed scintillating screen C_{scint} . Apparently, to get C_{cross} in the first place, the CLS also needs an absolute calibration.

This cross-calibration method is reliable, when the CLS fulfills

- the photon flux does not vary significantly from day to day;
- the spectrum is similar to that of the scintillating screen;
- the emission character is Lambertian;

- the brightness is comparable to the scintillating screen, i.e., given a properly set integration time (e.g., ~ 100 ms for the experiments in this work), the CLS produces a detector signal on the same order of magnitude as the scintillation screen hit by an electron bunch.

As already forecast in Subsec. 4.1.1, trilightTM gaseous tritium light sources (GTLs) from mb-microtec were implemented as CLSs for the measurement underlying this work. In particular, the GTLS-4, cf. radioactive source catalogue of LEX photonics, was measured during an absolute calibration campaign in September 2015, and $I_{\text{GTLs-4}} = 3.6(4) \times 10^7$ ph/sr/ms was found. It follows Eq. (4.4) immediately that the cross-calibration factor back then, e.g. for 100 ms of exposure time and CAWO OG 16 Back screen, was

$$C_{\text{cross}} = \frac{3.6 \times 10^7 \text{ ph/sr/ms} \times 100 \text{ ms}}{5.8 \times 10^9 \text{ ph/sr/pC}} = 0.62 \text{ pC}. \quad (4.5)$$

A GTLS is made of an airtight glass capsule several millimeters in length, filled with tritium gas. The inner capsule walls are coated with zinc sulphide phosphorescent powders so that electrons from tritium beta-decay are captured and their energy converted into visible light. Since the light yield of these capsules depends primarily on the amount of tritium, and tritium has a half-life of 12.32 years, GTLSs should in theory offer a nearly constant light output for months at least. In practice, the combined effect of tritium decay and phosphor aging results in about ten percent signal reduction after only one year. As a result, it is necessary to re-calibrate the GTLSs every year. Another drawback of GTLSs originates from their radioactivity. Despite the low average kinetic energy (5.7 keV) of the produced electrons, tritium gas is radiotoxic once inhaled. Therefore the capsules need to be handled with care to prevent damage. On the flip side, a GTLS has a good mobility thanks to its compactness, making an annual re-calibration feasible.

In order to study the decay characteristic of GTLSs quantitatively, T. Kurz built a dedicated testbed, which consists of a light-proof aluminium case, a CCD camera, a mounting plate for GTLSs, and an LED-based master light source, see master's thesis of Kurz [98] for more details. Since every component of the setup is installed at a fixed position relative to each other, the influence of changing geometry can be ruled out. Furthermore the master LED proves to offer a constant light yield over at least a decade considering its working condition. Consequently, the radiant intensity of a GTLS is unambiguously determined by its photon flux, or equivalently, the CCD counts, as long as the total counts of the master LED remain unchanged.

The decay history of some sources is depicted in Fig. 4.3 (a). Note that the GTLS-4, 6, 7 share a similar decay rate, whereas the GTLS-1 appears to have a significantly slower decay. A possible cause lies in the fact that the GTLS-1 is about 6 years older than other GTLSs. The reduced activity of tritium due to the age leads to a slower degradation of the phosphor hence a longer apparent characteristic time. An exponential function

$$\bar{\phi}_{\text{CLS}}(t) = \exp[-(t - a)/\tau] + b \quad (4.6)$$

is fitted to the normalized photon flux $\bar{\phi}_{\text{CLS}}$ that combines the data from GTLS-4, 6, 7, cf. Fig. 4.3 (b), and the parameters are found as $a = -35.6$, $\tau = 29.3$, and $b = 0.713$.

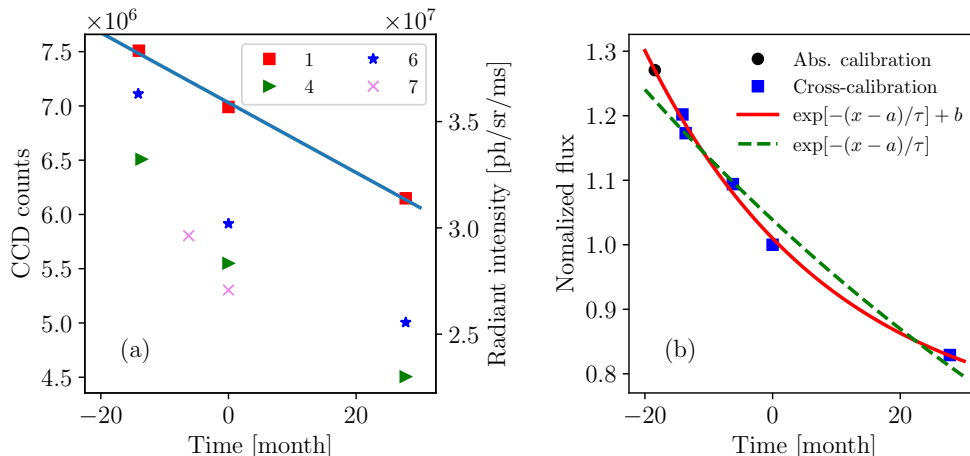


Figure 4.3: (a) decay history of the individual GTLSs in LEX photonics along with a linear fit (blue solid line; cf. main text) to the radiant intensity of the GTLS-1. (b) exponential fits to the data, where the flux of each GTLS, excluding the GTLS-1, is normalized on its own by the value in March 2017 i.e. 0 of Time axis. The mean value of normalized flux is taken if multiple GTLSs were measured on the same day. Note that fits are applied only to blue squares, and the black dot is extrapolated using the red solid curve.

The offset b in the model is not physically motivated. It is introduced only because the available data could not constrain $\exp[-(t-a)/\tau]$ well enough. Further investigation is required to clarify this issue. With the absolute calibration of GTLS-4 from September 2015 (cf. subsection 4.1.1) and the extrapolation of the exponential model to that date, the camera counts in Fig. 4.3 (a) are converted into radiant intensity as shown by the right y -axis. Contrary to the exponential model above, an over-simplified linear model

$$I_{\text{GTLS-1}}(t) = (-1.65t + 359) \times 10^5 \text{ ph/sr/ms} \quad (4.7)$$

is employed to describe the decay of the GTLS-1 due to limited data availability. The cross calibration factor C_{cross} in Eq. (4.4) then follows the decay law given by either Eq. (4.6) or Eq. (4.7).

4.1.3 Pointing screen in LEX photonics

Combining the intrinsic efficiency of scintillating screens (Subsec. 4.1.1) and the cross-calibration technique (Subsec. 4.1.2), a functional beam pointing and profile monitor can be built. During the measurement in LEX photonics, CAWO OG 16 Front screens (B2NV5U) were implemented in conjunction with the GTLS-1 as the CLS for charge determination. This screen provided a spatial resolution of 1 LP/mm at 50%, or 3 LP/mm at 10% of the modulation transfer function. With $\text{Gd}_2\text{O}_2\text{S:Tb}$ as the phosphor material, the emission spectrum of the screen peaks around 545 nm.

The stray light from laser would cause undesired background signal hence should be carefully shielded. An aluminium plate is therefore inserted upstream the vacuum chamber segment hosting the screen to block scattered laser beam, with a hole around the laser axis allowing

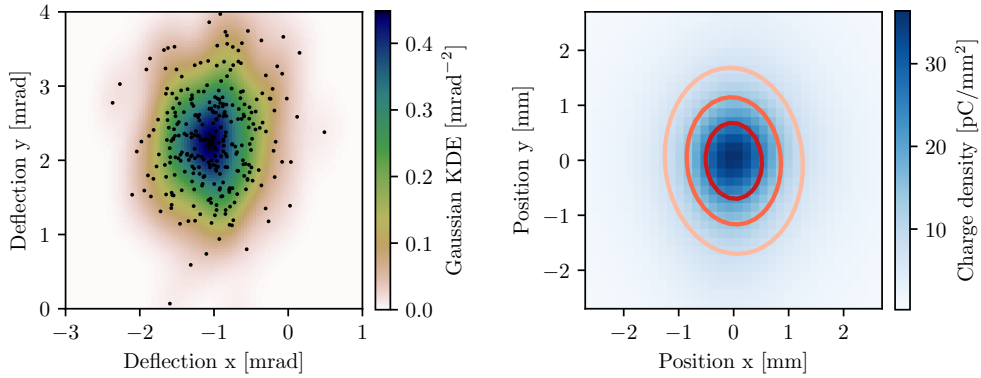


Figure 4.4: Results from the pointing screen. *Left*: pointing distribution of 311 shots in the run 3 of September-22-2016. The pointing of each shot is obtained from a 2D Gaussian fit to the electron beam profile. The r.m.s. pointing jitter of this run is 0.48 mrad in the horizontal direction and 0.88 mrad in the vertical direction. Color-coded is the Gaussian kernel density estimation of the distribution. *Right*: pointing-corrected average beam profile with contours at 1σ , 2σ , and 3σ levels. The beam center is deliberately shifted to the origin of coordinates. The projected r.m.s. beam divergence is 0.74 mrad horizontal and 1.0 mrad vertical, corresponding to a size of 2.3 mm^2 on the screen. The averaged total charge in the beam is about 232 pC.

electron beams to pass through. In addition, the 14-bit camera (Pointgrey Grasshopper GRAS-14S3M-C) viewing at the screen was equipped with, among others, a band-pass filter of 550 nm central wavelength that can suppress the laser and transmit the scintillation.

To mitigate laser-induced damage, the non-emitting surface of the screen was attached to a fifty-micron-thick Al foil. The assembly was positioned 1.8 m downstream the target and 0.3 m in front of the electron spectrometer, with the Al foil facing towards the laser pulse.

Seen from Fig. 4.4, the scintillating screen allows for online monitoring of the pointing and profile of electron beams, however, only in an energy-integrated fashion. Moreover the scattering of electrons inside the screen increases beam divergence significantly. As will be shown later in the next section, this divergence increase hinders energy-resolved divergence measurement and further reduces the energy resolution of the spectrometer; cf. Fig. 4.7. Therefore the screen was mounted on a motorized flipper and can be removed from the beam path on demand, to allow electron beams to enter the magnetic spectrometer undisturbed.

4.2 Magnetic spectrometer

Unlike electron bunches from RF accelerators, LWFA bunches often do not have a well-defined energy distribution. Instead, the bunch energy \mathcal{E} fluctuates and the energy spread $\Delta\mathcal{E}/\mathcal{E}$ can be sometimes as large as 100%. To cope with such bunch properties, a spectrometer for laser-plasma-based accelerator research is usually made of large-area (up to meters in length) scintillating screens and dipole magnets that deflect each energy component of the electron bunch to a different position on the screen; cf. Fig. 4.5. The spectrometer magnet used in this work is an array of 8 units as shown in Fig. 4.6. Each unit is 10 cm long and has

4.2. Magnetic spectrometer

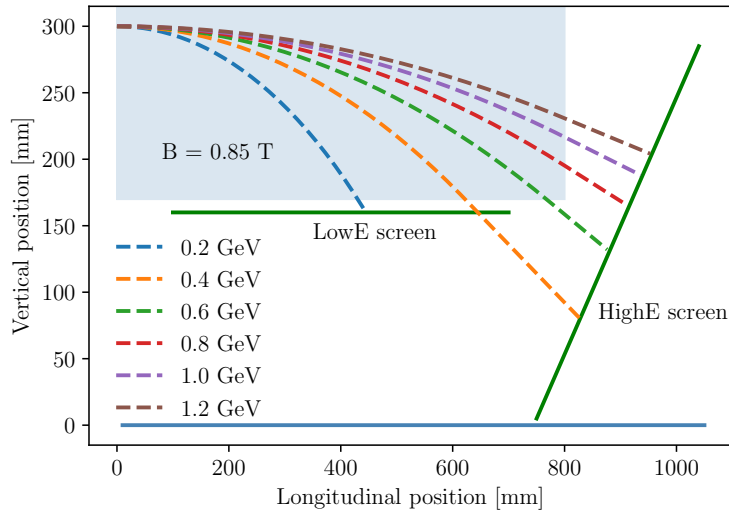


Figure 4.5: Schematic side view of the magnetic spectrometer. The shaded area indicates the B-field of dipole magnets. Dashed lines represent trajectories of electrons with different kinetic energies. This configuration was used to obtain the data presented in Sec. 3.8

six VACODYM 764 TP [55] magnets attached to a steel yoke. There is a 40 mm horizontal gap between magnets for electrons to pass through, with an in-gap dipole B-field strength of approximately 0.85 T. The spectrometer entrance is 2.1 m away from the target, resulting in a horizontal acceptance angle around 8 mrad for the middle section of the spectrometer, where the most electrons of interest are detected.

The magnet bends the electron beam towards the ground. About 3 cm, or 5 mm for experiments prior to raising up the magnet, below the magnet, scintillating screens (CAWO OG 16 A2FL5V Back) are placed in a 2-mm-thick light-tight aluminium case, imaged via folding mirrors onto a 14-bit CCD camera (Pointgrey Grasshoper GRAS-20S4M). In Fig. 4.7 some typical spectrometer images taken with the pointing screen in place are compared with those without the pointing screen. The pointing screen results in a roughly 7-fold increase in the

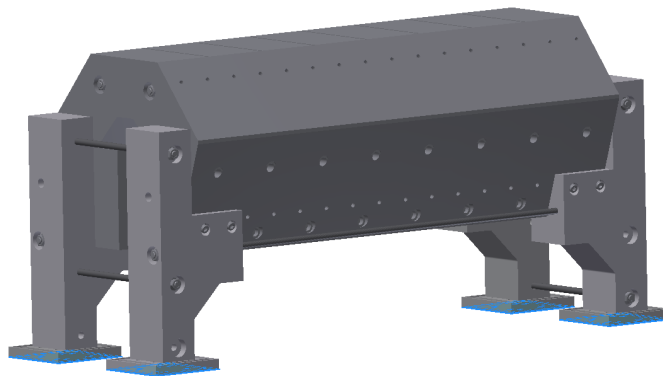


Figure 4.6: Rendering of the spectrometer magnet, courtesy G. Schilling.

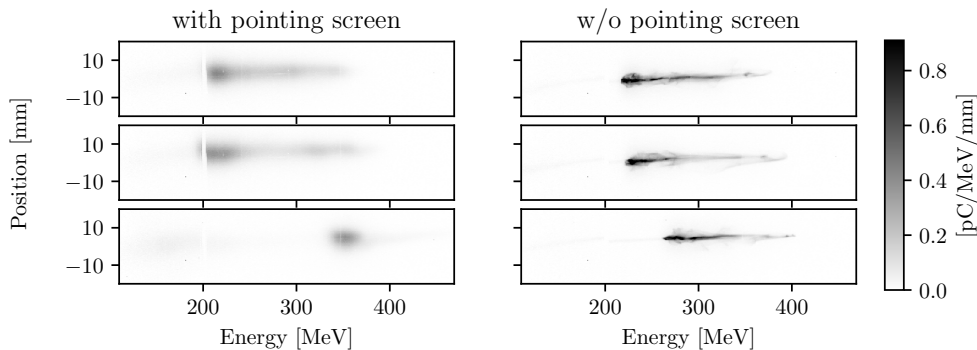


Figure 4.7: Comparison between images from electron spectrometer with (Run 3, September-22-2016) and without (Run 4, same day) the pointing screen. Other experimental parameters were set the same. The color range is chosen to saturate the right column in order to improve the visibility of the left column. The white vertical bars in the images are due to either markers on the screen or the gap between folding mirrors in the imaging setup.

slice divergence, measured using the full width at half maximum (FWHM) at the spectral peak, for the presented shots.

Quantitative conclusions can be drawn from the spectrometer only if its energy and charge axes are calibrated. As the charge calibration was already mentioned in Sec. 4.1, this section will focus on the energy axis.

4.2.1 Electron tracking

The distribution of magnetic field is essential to determine the precise correlation between an electron's kinetic energy and its final position on the scintillation screen. Therefore a Hall sensor was scanned over the central volume between the magnets. The fringe field outside the yoke was also covered by that scan, as shown in the inset of Fig. 4.8.

Taking the measured magnetic field distribution as input, single electron trajectories in the spectrometer were calculated with the software package General Particle Tracer (GPT) [99]. Figure 4.8 illustrates the final position of an electron on the scintillating screen (3 cm below magnets) as a function of its kinetic energy. It is apparent that the incidence angle into the magnetic field plays an important role in determining the energy calibration of the spectrometer, so an unknown beam pointing leads to an uncertainty in beam energy. For example, a vertical pointing error of 1 mrad corresponds to an energy uncertainty of 5 MeV @ 300 MeV; cf. Fig. 4.4.

Inserting a scintillating screen into the beam path and recording simultaneously pointing and spectrum allows one to correct the energy later on. A caveat is that the screen deteriorate the beam's divergence, which in turn causes new errors; cf. Fig. 4.7.

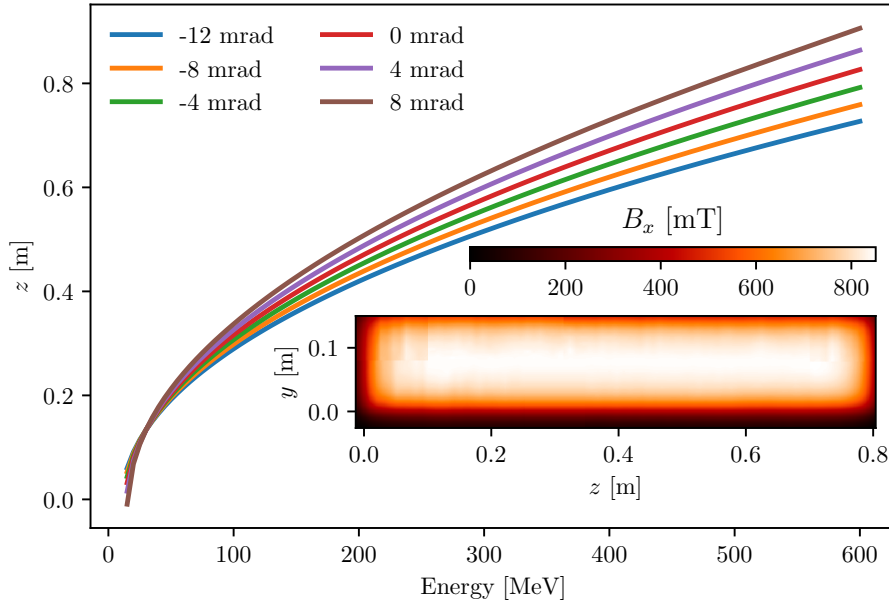


Figure 4.8: Energy calibration of the magnetic spectrometer for various incidence angles, calculated with General Particle Tracer. *Inset*: Magnetic field map measured with a Hall sensor, by courtesy of S. Raith.

4.2.2 Magnet focusing

The aforementioned energy uncertainty due to pointing error and beam divergence can be reduced by utilizing the focusing property of magnets.

Figure 4.9 depicts electron trajectories inside a 2.1-m-long 0.85 T magnet for various kinetic energies. The B-field is modeled as a constant of 0.85 T within a rectangular region and zero outside. The electron source is point-like and situates 2.7 m from the magnet entrance, so-chosen to match initial experimental configuration in CALA. The inclination angles are ± 2 mrad. When exiting the magnet from the lower edge, electrons with a positive inclination will experience more bending in the field compared to those with a negative inclination (note that this effect does not apply to electrons leaving the field from the right edge). As a result, the magnet will focus the electron beam. Analogous to a lens that focuses optical rays, the dipole magnet images the electron source to a focal surface, and each point in the surface can be associated with a different energy bin.

In general, the focal surface is not flat. Moreover, the measured magnetic field distribution can not make a perfect focus due to aberrations just as any realistic lens. However, given the ~ 1 LP/mm spatial resolution of scintillating screens and the ~ 1 mrad converging angle, a plane is a reasonably good approximation to the focal surface. Electrons of up to 1 GeV energy can be imaged inside the experimental chamber using the setup described above. To facilitate focusing of multi-GeV of energies for the experiments in CALA, either a stronger magnet shall be used for more bending, or the spectrometer shall be flipped upside down for more space.

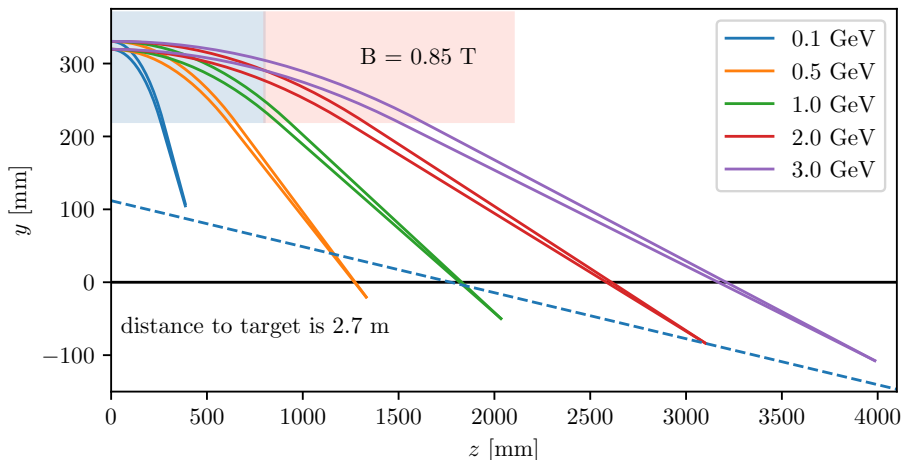


Figure 4.9: Focusing of electron beams with various kinetic energies and inclinations of ± 2 mrad (solid lines) in a 2.1-m-long dipole magnet with a constant B-field strength of 0.85 T (shaded area, both blue and pink). The source is 2.7 m away from the magnet. The dashed line represent the focal plane, obtained with a linear fit to the energy-dependent focal points.

4.3 Interferometry

4.3.1 Nomarski interferometer

A central question in the LWFA research is the plasma density, to which one often seeks answers from interferometers. In particular, the Nomarski-type interferometer [100] offers a simple yet robust solution in a laser-plasma experiment to measure the electron density. As shown in the Figure 4.10, a Nomarski interferometer is an inline setup consisting of a Wollaston prism—two birefringent prisms with perpendicular optic axes cemented together, a pair of polarizers—either orthogonal or parallel oriented, and an imaging system.

The working principle of a Nomarski interferometer is as follows (see Fig. 4.10 for reference): the lens images the object plane, in which laser-plasma interaction takes place, to the image plane with a proper magnification; polarizer 1 sets the laser polarization to 45° relative to the optical axes of both segments of the Wollaston prism; as such, the Wollaston prism splits the beam into two replicas, thus creating two virtual sources in the focal plane of the imaging lens, with equal intensity but orthogonal polarization; polarizer 2 rotates the polarization of both beams to the same direction and enables interference in the region where both beams overlap. Ideally, the overlap region should contain the plasma shadow from one beam and vacuum propagation from the other beam. The fringe spacing, δ , is determined by the beam separation angle, ε , and the position of the Wollaston prism as

$$\delta = \frac{\lambda_L d_I}{\varepsilon d_F}, \quad \text{for } d_I \ll d_F, \quad (4.8)$$

where d_I and d_F denote the distance from the beam separation point in the Wollaston prism to the image plane and the focus position of the imaging lens, respectively, and λ_L is the wavelength of the probe laser.

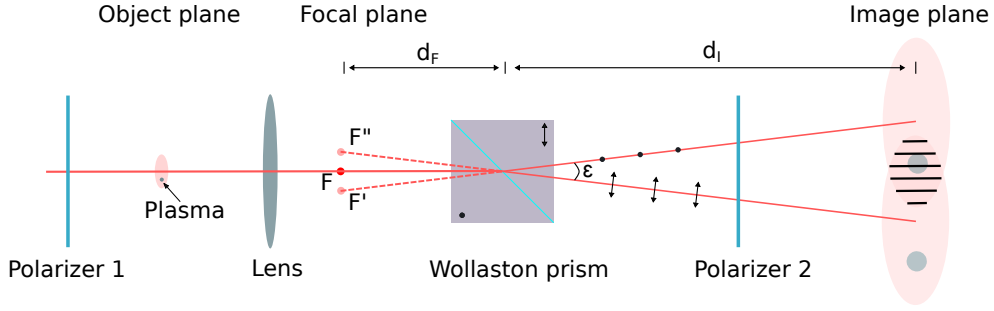


Figure 4.10: Schematic of a Nomarski interferometer.

An interferogram, recorded with a Nomarski interferometer, of a gas jet interacting with an ultrashort laser pulse is shown in Figure 4.11, where the bending of fringes encodes the accumulated phase difference, $\Phi(\mathbf{r})$, between the propagation in free space and that through the laser-generated plasma, namely,

$$\Phi(\mathbf{r}) = \frac{2\pi}{\lambda_L} \int dx [1 - \eta(x, \mathbf{r})]. \quad (4.9)$$

Here $\mathbf{r} = (y, z)$ is a shorthand notation for the two dimensional coordinates in the image plane. λ_L denotes the probe laser wavelength and η the refractive index of the plasma defined in Eq. (2.49). The coordinate system is defined so that the drive laser propagates to the z -direction and the probe laser to the x -direction.

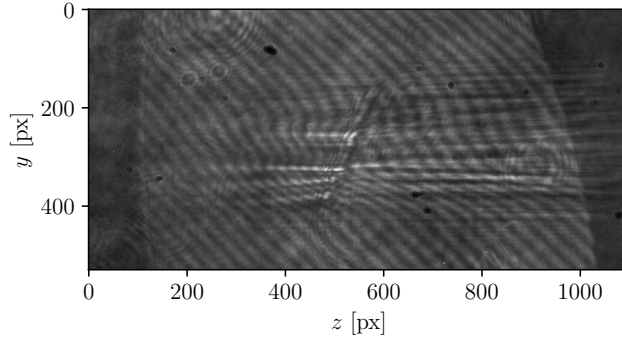


Figure 4.11: Raw data from a Nomarski interferometer.

Expanding the refractive index using Taylor series, and truncating to the first order yields

$$\eta = \sqrt{1 - \frac{n_e}{n_c}} \approx 1 - \frac{n_e}{2n_c}. \quad (4.10)$$

Eq. (4.9) can thus be simplified as

$$\Phi(\mathbf{r}) \approx \frac{\pi}{\lambda_L n_c} \int dx n_e(x, \mathbf{r}), \quad (4.11)$$

which connects the phase with the electron density.

4.3.2 Phase retrieval

The quantitative relation between the phase difference $\Phi(\mathbf{r})$ and the intensity distribution $I(\mathbf{r})$ measured in the interferogram can be obtained from a simple two-beam interference. Let $E_1 = \exp[i\mathbf{k}_1 \cdot \mathbf{r}]$ and $E_2 = \exp[i\mathbf{k}_2 \cdot \mathbf{r} + i\Phi(\mathbf{r})]$ represent the E-fields of the interfering beams in the image plane (the amplitude of the two beams is assumed equal for simplicity), it follows immediately that the intensity

$$\begin{aligned} I(\mathbf{r}) &= |E_1 + E_2|^2 \\ &= 2 + 2 \cos[\Delta\mathbf{k} \cdot \mathbf{r} + \Phi(\mathbf{r})]. \end{aligned} \quad (4.12)$$

The wave vector $\Delta\mathbf{k} = \mathbf{k}_2 - \mathbf{k}_1$ is related to the fringe spacing as $\Delta\mathbf{k} = 2\pi/\delta$; cf. Eq. (4.8)

Thus the phase $\Phi(\mathbf{r})$ can be retrieved from the raw interferogram using a method based on fast Fourier transform (FFT). By masking out a narrow band in the Fourier space and discarding the negative frequencies, the interferogram can be converted into complex numbers whose complex phase representing the phase accumulation. The software IDEA-Interferometric Data Evaluation Algorithms [101] offers a powerful suite of tools for interferogram analysis and was used to obtain data presented in this work.

4.3.3 Abel Inversion

Assuming an axially symmetric electron density distribution and dropping z -dependence for brevity, equation (4.11) can be written with polar coordinates as

$$\Phi(y) = \frac{2\pi}{\lambda L n_c} \int_y^\infty \frac{n_e(r) r dr}{\sqrt{r^2 - y^2}}. \quad (4.13)$$

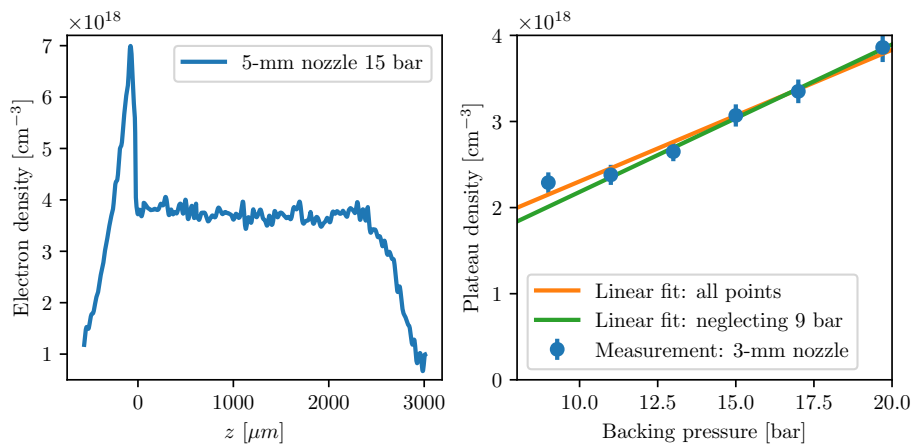


Figure 4.12: Interferometric measurement of gas jet density. *Left*: Longitudinal density profile of the 5-mm nozzle with shockfront. *Right*: The plateau density as a function of the backing pressure for the 3-mm nozzle.

4.3. Interferometry

The equation above is an Abel transformation, therefore the inversion formula can be readily given:

$$n_e(r) = -\frac{\lambda_L n_c}{\pi^2} \int_r^\infty \frac{\partial \Phi(y)}{\partial y} \frac{dy}{\sqrt{y^2 - r^2}}. \quad (4.14)$$

If the assumption of axial symmetry is not physically justified, special cares need to be taken, e.g. using the methods proposed in Ref. [102]. Figure 4.12 is an example of applying Abel inversion to determine the average plasma density produced with de Laval nozzle targets.

5 Few-cycle shadowgraphy

The basic diagnostic tools introduced in the previous chapter provide mostly information on the final state properties of a laser wakefield accelerator (LWFA). With this information, the community has come a long way in maturing the LWFA technology; cf. Refs. [8, 12, 81, 103]. The key to gaining better control over the acceleration process lies, however, in understanding its time-dependence and dynamic evolution. In this regard, great effort has been made in creating increasingly sophisticated numerical methods [38, 39] to simulate the experimental conditions. Due to the broad range of the involved scales, i.e. the laser wavelength ($\sim \mu\text{m}$) and the acceleration length ($\sim \text{cm}$) and the large number (normally $> 10^6$) of particles to be considered, these simulations are inherently computationally costly. Furthermore, the limited knowledge about the detailed experimental parameters and the imperfections in modelling often mean that the simulations need to be fine-tuned to reproduce the experiments. As a result, though current particle-in-cell (PIC) simulations could eventually reach quantitative agreement with experiments, they do not yet lend themselves to visualize experiments in real-time. In pursuance of validating the simulations and more importantly, online monitoring of the experiments, time-resolved diagnostics are required. An ultimate LWFA diagnostic should offer information on the electron density function in the 6+1 dimensional $(\mathbf{x}, \mathbf{p}, t)$ phase space, which is only partially fulfilled in practice. In this chapter, the few-cycle shadowgraphy technique pioneered by Sävert et al. [40, 45] will be introduced, which could provide information in 2+1 D, or 3+1 D with some additional effort.

5.1 Few-cycle probe setup

In order to efficiently excite plasma waves, the plasma density in an LWFA experiment is usually chosen to fulfill the resonant condition $c\tau \sim \lambda_p/2$ (cf. Chapter 3). This implies that the bandwidth of the laser is often insufficient for time-resolved study of the transient behaviour of plasma dynamics. To address this issue, a hollow-core fiber based pulse compressor was implemented in the framework of this dissertation, and Felix Daiber's master's thesis [104]; cf. Ref. [43] and Fig. 5.1.

A fraction of the compressed ATLAS beam containing about 20 mJ of energy (hereafter referred to as the probe pulse) is clipped out by a half inch mirror in front of the final focusing optic. The probe pulse is sent subsequently through a 1-mm-thick fused silica window to an optical table outside the vacuum target chamber. An iris and ND filters adjust the diameter and the energy of the probe pulse to about 8 mm and 1 mJ, respectively. A dispersive mirror array together with a variable-thickness glass wedge pair compensates the group delay

5.1. Few-cycle probe setup

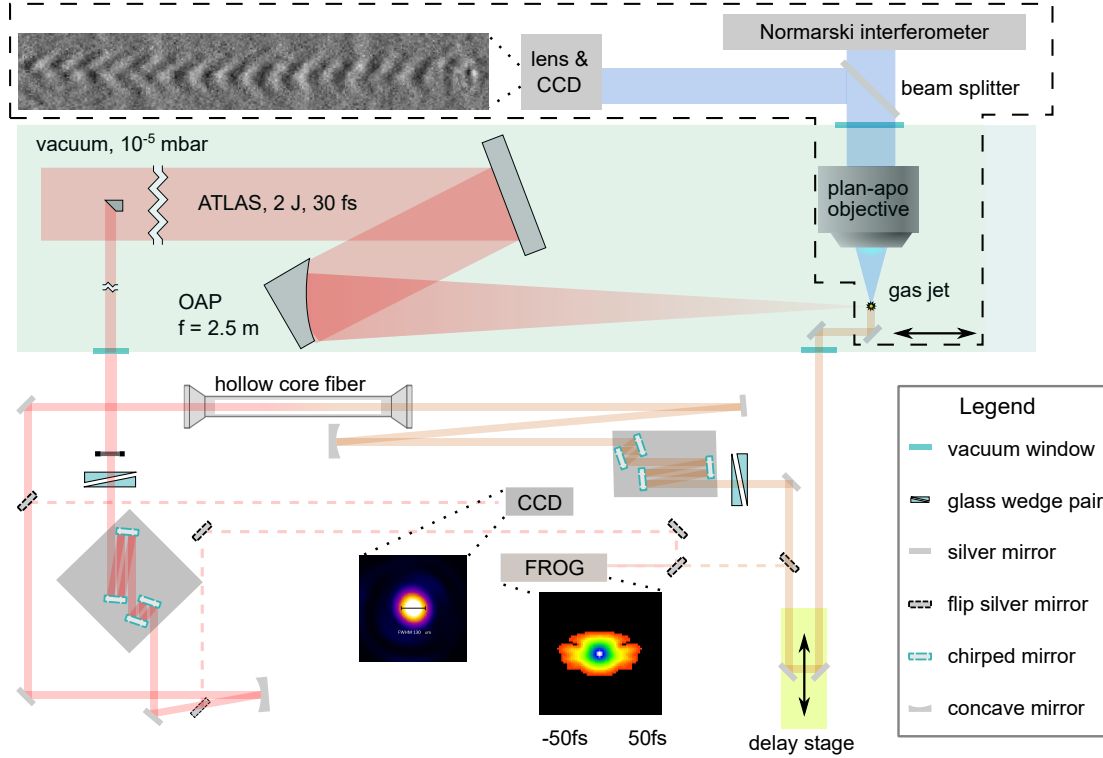


Figure 5.1: Schematic of the pump-probe setup. Image adopted/modified from Ref. [43].

dispersion (GDD) accumulated during pre-fiber propagation and therefore ensures effective self phase modulation (SPM) inside the Ar-filled hollow core fiber. The installed dispersive mirrors (UltraFast Innovations PC70) are designed for the spectral range of 500 - 1050 nm and they need to be used in pairs with incidence angles of 5 and 19 degrees. The hollow-core fiber in this setup (FEMTOLASER KaleidoscopeTM) has an inner-diameter of 240 μm and a length of 0.9 m. With 500 mbar of argon pressure, about 400 μJ can be transmitted through the fiber. A second array of dispersive mirrors and a wedge pair compress the spectrally broadened pulse to close to its Fourier limit. A motorized delay stage sets the proper synchronization between the main pulse and the probe. At the same time, it allows for study of plasma wave evolution by setting the relative delay. The probe pulse is then sent transversely through the interaction region and collected with a long working distance plan apochromatic microscope objective (Mitutoyo Plan Apo NIR 5X or 10X, depending on the magnification requirement of the experiment) to form either shadowgrams or interferograms with a spatial resolution of $\sim 2 \mu\text{m}$. The whole imaging setup as marked by the dashed line in Fig .5.1, excluding the gas jet, but including the last folding mirror before the target, can be shifted along the main laser axis thus allowing different part of the target to be sampled without altering the relative delay.

5.2 Shadowgraphic observation of linear and nonlinear plasma waves

Figure 5.2 depicts a raw shadowgram recorded with a 12-bit CMOS camera (Allied Vision Mako G-419B-NIR). As in other types of shadowgrams, the measured intensity contrast originates from phase contrast in the object under probing [105]. The apparent light intensity is proportional to the second derivative of the refractive index with respect to the spatial coordinate in the plane transverse to the probe laser's propagation direction. On the other hand, the distance between the object plane and the plane being imaged also affects the intensity contrast. For the typical plasma density used in this work ($\sim 4 \times 10^{18} \text{ cm}^{-3}$), the contrast was found the best when the plane about $100 \mu\text{m}$ away from the plasma wave was imaged.

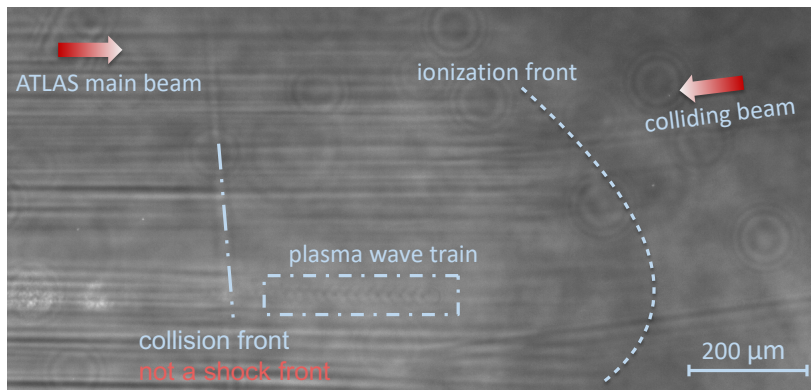


Figure 5.2: An example raw shadowgram of two laser pulses colliding in a hydrogen plasma.

At first glance, horizontal striations are probably the most prominent structure. They extend over the entire region where the laser intensity is (or once was) above the threshold of barrier suppression ionization (cf. Sec. 2.4). In this region initially neutral gas molecules get rapidly ionized, decreasing the local refractive index and defining the outer boundary of the observed pattern, or the so-called ionization front. The actual striations are likely caused by the speckles from high-frequency diffraction surrounding the laser focus, which modulate the ionization degree in the low-energy wings and thus cause refractive index gradients.

Owing to the few-cycle duration of the probe pulse, the laser-driven plasma wave can be directly observed, which manifests as an periodic modulation of the probe beam intensity along the laser axis. Though the intensity distribution of probe beam does not directly translate into electron density, the periodicity of the modulation reflects the local plasma wavelength.

As the starting point of the visible plasma wave marks the position of the high intensity peak of the laser, the distance between the head of the plasma wave and the ionization front gives a rough estimate of the temporal intensity contrast of the laser pulse. For instance, the ionization front is $\sim 300 \mu\text{m}$ away from the plasma wave in Fig. 5.2, indicating a contrast of $\sim 10^{-5}$ @ -1 ps , considering that the ionization intensity for hydrogen is on the order of $10^{13} \text{ W}/\text{cm}^2$; cf. Table 2.1.

As already outlined in Sec. 3.1, a plasma wave is excited when a laser pulse with relativistic

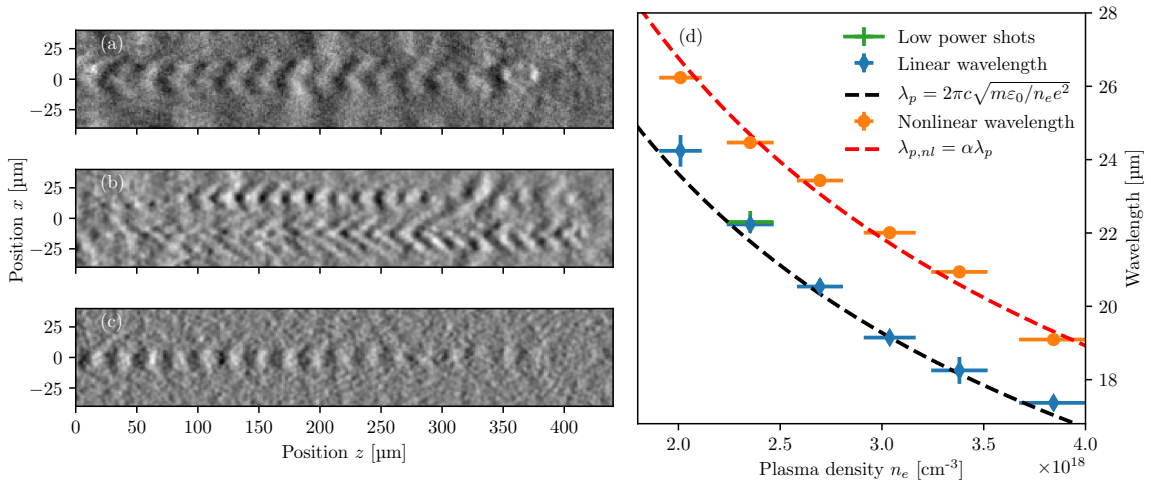


Figure 5.3: *Left:* Representative shadowgrams of laser driven plasma waves in the plasma density range of $n_e = 2 - 4 \times 10^{18} \text{ cm}^{-3}$. (a) a nonlinear plasma wave driven by a 70 TW pulse. (b) a strongly nonlinear plasma wave driven by a 70 TW pulse with a weaker secondary wave above it. Note that the secondary wave starts at the same position as the main wave, but its modulation at the front is poorly visible due to its overlap with a diffraction feature in the probe’s near-field profile. (c) a quasi-linear plasma wave driven by a 13 TW pulse. *Right:* The wavelength of plasma oscillation as a function of electron density. The nonlinear wavelengths (orange dots) are obtained from the main waves whereas the linear wavelengths (blue dots) are deduced from the filaments; cf. panel (b). The low power shots (green dot) are taken at 13 TW; cf. panel (c). Each data point is an average of 2 to 9 shots. The vertical error bars represent the standard error of mean (s.e.m.) of each run. The horizontal error bars are the estimated uncertainties in the density retrieval from interferometry. A least square fit to the nonlinear wavelengths (dashed red line) yields the elongation factor $\lambda_{p,nl}/\lambda_p$ of $\alpha = 1.13$. Figure reproduced from Ref. [43].

intensity propagates inside an underdense plasma. Depending on the intensity of the driver, there are different regimes. Employing the full pulse energy ATLAS provided during this experiment (70 TW on target, vacuum $a_0 \simeq 1.6$), plasma waves similar to that shown in Fig. 5.3 (a) were often observed. The curved wave fronts clearly indicate that this wave is nonlinear. Occasionally, secondary plasma waves with shorter wavelengths appeared in the vicinity of the main wave; cf. Fig. 5.3 (b). This is likely due to the laser being out of focus at the gas jet edge and its imperfect mid/far-field intensity distribution. As those filaments are expected to have lower intensities than the main focus, this observation hints at an intensity-dependent plasma wavelength. Therefore, a comparative measurement was carried out at reduced laser power (13 TW on target, vacuum $a_0 \simeq 0.7$). The plasma wavelength was now significantly shorter than that of a nonlinear wave at the same density, yet similar to that of the filaments; cf. Fig. 5.3 (c).

To establish a quantitative relation between the measured plasma wavelengths and the analytical non-relativistic model Eq. (3.27), Normaski-type interferometry was performed to independently determine the electron density. Owing to the large field of view of the interferometry camera, this provided an in-situ measurement of the phase difference between the plasma column fully ionized by the drive laser and the background gas in the jet. The density can then be retrieved via Abel inversion, assuming a cylindrical symmetry of the

plasma channel; cf. Sec. 4.3.

In the density plateau of a 3-mm-long hydrogen gas jet (about 1.8 mm of propagation in plasma), at full power the wavelength deduced from shadowgrams is $\lambda_{p,nl} = 1.13\lambda_p$ for the main wave in a density range of $n_e = 2 - 4 \times 10^{18} \text{ cm}^{-3}$. In contrast, the wavelength of both the filament- and low-power driven waves does not significantly differ from the expected cold λ_p ; cf. Fig. 5.3 (d).

5.3 Nonlinear plasma wavelength scaling

Based on the theory introduced in subsection 3.1.2, it should be straightforward to deduce the local peak potential a_0 from the measured plasma wave elongation. In the 13 TW case, all models predict an elongation of 1 – 2%, which is within the measurement uncertainty. However, it turns out that relating the measured $\lambda_{p,nl}$ to a realistic value of driver a_0 is much more difficult at 70 TW, as is summarized in Table 5.1.

Method	Estimated a_0
1D nonlinear model for rectangular pulse	1.6
1D nonlinear model for gaussian pulse	1.95
Momentum based estimate	1.15
Momentum based estimate (FWHM average)	2.15
Vacuum focus	1.6
Matched spot size	4.0
Particle-in-cell simulation	4.5

Table 5.1: *Upper part:* Various estimates for the laser a_0 based on models for the nonlinear plasma wavelength (cf. Sec. 3.1) and the measured value $\lambda_{p,nl} = 1.13\lambda_p$. *Lower part:* Comparison with estimates based on the measured focal spot and pulse energy, the matched spot size for $P = 70 \text{ TW}$ and $n_e = 3 \times 10^{18} \text{ cm}^{-3}$ and the result from a PIC simulation after 2 mm of propagation.

Interpreting the measured elongation factor of 1.13 using the analytical solution of 1D fluid theory with a square pulse, Eq. (3.31), yields a laser peak potential $a_0 = 1.6$ and a scaling parameter $\chi = 0.85$. Note that the scaling factor χ considerably differs from the model’s validity range ($\chi \ll 1$), rendering this result rather unreliable. Given the experimental pulse shape cannot be considered a rectangle anyway, a more realistic Gaussian pulse will be considered next. The numerical solution of Eq. (3.22) suggests a slightly higher value of $a_0 = 1.95$.

On the other hand, the observed lengthening can be associated with the relativistic increase of the electron mass, yielding a γ -factor of 1.28 at full power. Based on Eq. (3.32) this would correspond to a normalized potential of 1.12, even lower than the inferred vacuum potential. However, the assumption that all electrons experience the same intensity, i.e. the peak potential a_0 , is unrealistic. Instead, the retrieved value should be interpreted as an averaged potential $\langle a \rangle$. By assuming a Gaussian shape of the intensity profile and taking the average potential within the full width at half maximum in both transverse and longitudinal directions to be 1.12, a peak value of $a_0 = 2.15$ is obtained.

To sum up, there is a large variation between the estimates from models discussed in Sec. 3.1. The results are roughly compatible with the vacuum focus intensity, but the laser will self-focus inside the plasma and a much higher value for a_0 is expected inside the plasma. For a 70 TW laser in a plasma with $n_e = 3 \times 10^{18} \text{ cm}^{-3}$, a matched spot has a waist $w_0 = 12 \mu\text{m}$ and a peak potential $a_0 = 4.0$ according to Lu et al. [36], if the energy deposition to the plasma can be neglected. Hence the a_0 values deduced from the measured elongation factor using the models plotted in Fig. 3.3 are significantly too small. On the other hand, as no external guiding technique is applied and the initial spot size does not fulfill the self-guiding condition, the laser is also expected to evolve strongly during the propagation. Consequently, there is considerable uncertainty in the driver intensity at the measurement point.

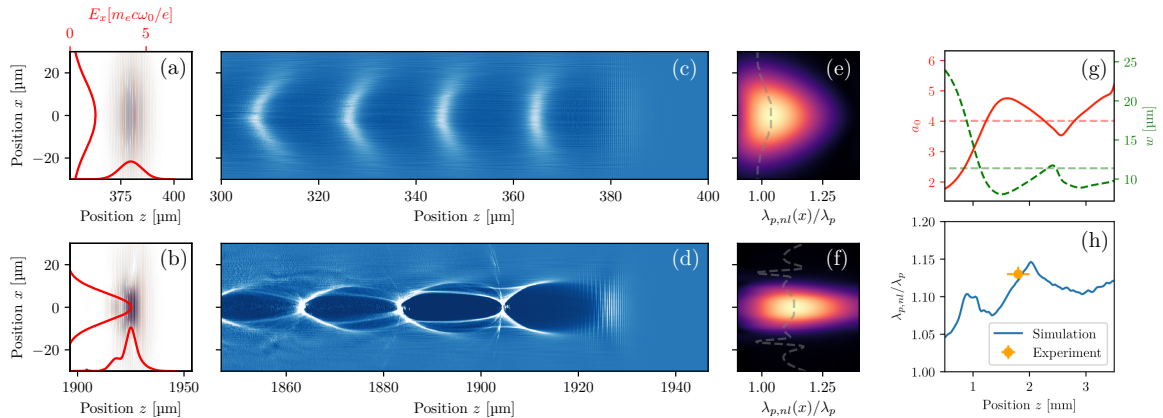


Figure 5.4: Snapshots of a quasi-3D simulation of a 70 TW 30 fs (FWHM) pulse propagating in a 3-mm-long hydrogen gas jet with a nominal electron density of $n_e = 3 \times 10^{18} \text{ cm}^{-3}$: upper panels are for the beginning of the jet and lower panels are for the center of the jet where the experimental data are taken (cf. Fig. 5.3). From left to right: (a-b) the intensity distribution (false color) together with the E-field envelope of the laser pulse in transverse and longitudinal direction (red lines), normalized by $m_e c \omega_0 / e$, with ω_0 the laser carrier frequency. (c-d) the electron density distribution. (e-f) line-by-line Fourier transform of the electron density with the abscissa converted from wave number to wavelength and the intensity corrected by the Jacobian ($\partial k_p / \partial \lambda_p$; to account for the non-uniform sampling; false color), and the position of the intensity maximum at each transverse coordinate x (the dashed line). Note that the wiggles in (f) are a numerical artifact due to the weak density modulation outside the drive laser. (g) the evolution of the peak laser potential (red solid line) and the beam waist (green dashed line). The horizontal lines indicate the matched condition from Lu et al. [36]. (h) the evolution of the elongation factor (blue line), which shows good agreement with the measurement (orange dot). The vertical error bar of the measured dot indicates the 95% confidence interval of the elongation estimate and the horizontal error bar is the sum in quadrature of the length of the visible wave train and the uncertainty in determining the length of the gas jet up-ramp. Figure reproduced from Ref. [43].

In order to understand the experimental results in detail, and to gain insight on the evolution of the drive laser, quasi-3D simulation of the laser propagation and plasma wave formation is carried out using FBPIC [39]. Similar to other quasi-3D codes such as CALDER-CIRC [38], FBPIC employs an azimuthal Fourier decomposition, where the lowest two modes are associated with the radial symmetric component of the wakefield and the laser field, respectively. As the wake can become asymmetric at large laser intensities, higher order modes $m > 2$ might become necessary to model the system [38]. Here $m = 4$ modes, and the resolution is $\Delta z = \lambda_0 / 30$ in longitudinal and $\Delta r \approx \lambda_p / 100$ in the radial direction for a simulation

window of $z \times r = (100 \times 65) \mu\text{m}^2$, initialized with 32 particles per cell for $r < 30 \mu\text{m}$. The plasma is considered as completely pre-ionized with a longitudinal density profile consisting of a $150 \mu\text{m}$ linear ramp, followed by a constant density of $n_e = 3 \times 10^{18} \text{cm}^{-3}$. The driver is a laser pulse initialized in vacuum with a FWHM duration $\tau = 30 \text{fs}$, a FWHM spot size of $30 \mu\text{m}$, and a peak potential $a_0 = 1.6$. The simulation results are summarized in Fig. 5.4.

At the beginning of the gas jet, the 70 TW laser pulse has a FWHM spot diameter of $30 \mu\text{m}$, larger than its FWHM pulse length $c\tau = 9 \mu\text{m}$ and the linear plasma wavelength $\lambda_p = 19.3 \mu\text{m}$, hence the plasma motion is still predominantly longitudinal. As a result, the lengthening of the plasma wave train follows roughly the laser's radial intensity distribution and the wave fronts become curved with the curvature increasing farther behind the driver; cf. Fig. 5.4 (c) and (e).

Over the first millimeters of propagation, self-focusing reduces the spot size to below λ_p and the transverse component of the ponderomotive force becomes comparable to its longitudinal one. In this case, transverse plasma oscillations cause complete electron cavitation behind the driver, leading to the well-known bubble-like structure [9, 106]. Furthermore, comparing the dashed lines in Figs. 5.4 (e,f), the plasma wavelength ceases to vary in the transverse direction and appears to be almost a constant throughout the wave due to phase mixing of plasma oscillation.

As shown in the Fig. 5.4 (g), the peak laser intensity oscillates in the range $a_0 = 3.5$ to 4.5 around the matched value of $a_0 = 4$; this oscillation is caused by the unmatched initial spot size. At the same time, Fig. 5.4 (h) shows the lengthening of the wave train $\lambda_{p,nl}/\lambda_p$, which is between $1.10 - 1.15$. This value is much smaller than the prediction of the models in Sec. 3.1 for a pulse with $a_0 \sim 4$, yet compatible with the experimental data. Indeed, at the center of the jet, the simulation accurately reproduces the measured plasma wave lengthening of 13%.

The poor performance of the widely established analytical models compared to the good agreement between simulation and experiment therefore indicates that the physics of plasma wave trains is also influenced by effects that are not included in the model. In particular, it is too simplistic to assume that the wave train formation is dominated by a single parameter, the peak potential a_0 . As the plasma wave is generated by the ponderomotive force [8], $\vec{F}_p = -m_e c^2 \vec{\nabla}(a^2/2)$ (for $a_0 \ll 1$), which depends on the gradient of the intensity, the wave formation will not only depend on the peak value a_0 , but also the pulse length and width. The latter is particularly important, as it directly influences the transverse motion of electrons and therefore plays a major role in the breakdown of any 1D laminar model.

To illustrate this behavior, Fig. 5.5 shows simulation results for both the plasma waves and the trajectories of plasma electrons driven by laser pulses of different peak intensities and spot sizes, with a width-to-length ratio $w_0/c\tau = 3$ in the left, and $w_0/c\tau = 1$ in the right column.

As expected, in the case of a wide focal spot, a simple extension of the 1D theory to higher dimensions assuming laminar motion still seems reasonable for peak potentials $a_0 < 3$. The wave amplitude and wavelength are modulated by the radial intensity profile of the laser, leading to a horse-shoe like structure in the laser's wake. With peak potentials $a_0 > 3$, the

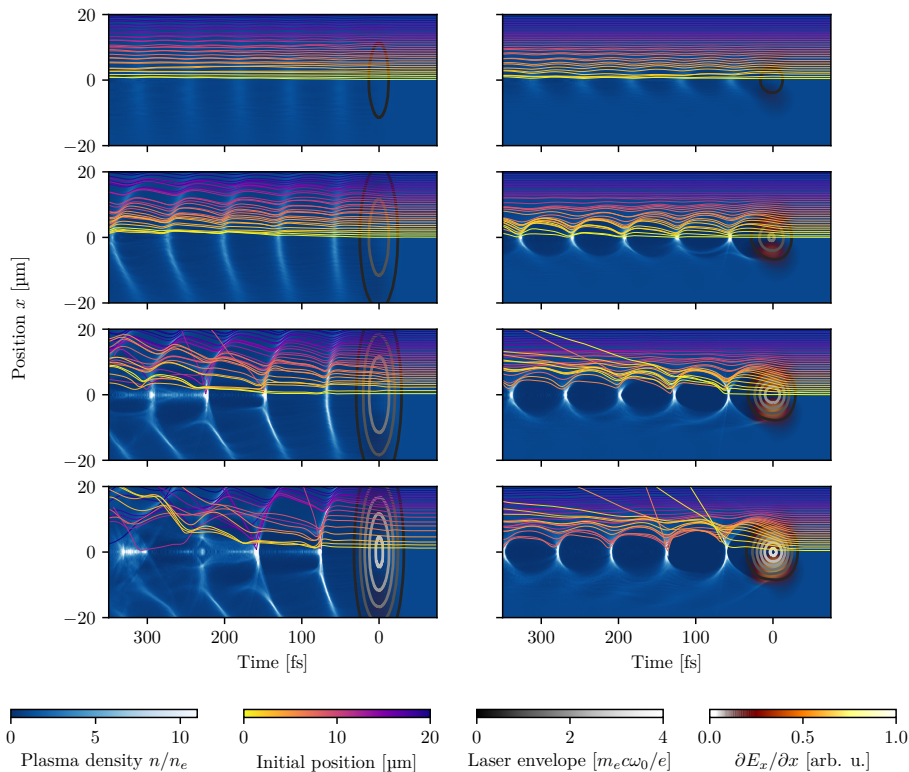


Figure 5.5: Comparison of plasma wave train formation in the wake of a tightly focused spot (right) and a 3 times as wide spot (left) at various laser peak potentials ($a_0 = [1.0, 2.0, 3.0, 4.0]$ from top to bottom). Colored lines show the trajectories of electrons with different initial position in radial coordinates. The normalized E-field strength of the laser is shown as grey-scale contour plot and the transverse field gradient is indicated with an overlaid colormap. The transverse gradient of the tightly focused laser leads to stronger transverse electron motion and thus prevents them from experiencing the peak laser potential. This further leads to cavitation and suppresses the elongation of the wave train. In contrast, the simulations for a wide focal spot are comparable to laminar models, with a characteristic horseshoe-like shape, until wavebreaking sets in for $a_0 \gtrsim 3$. All simulations are performed for a plasma density $n_e = 3 \times 10^{18} \text{ cm}^{-3}$ and using an FWHM pulse duration of $\tau = 30 \text{ fs}$. Figure reproduced from Ref. [43].

fields reach the (relativistic) wave-breaking limit and hence the fluid model breaks down, marked by the self-injection into the wakefield.

For the tightly focused case, the fluid model breaks down even sooner and the dynamics of the plasma wave fundamentally change. Due to the increasingly transverse motion, many electrons drift farther away from laser axis even before they experience the local intensity peak of the laser pulse. As a result, a high proportion of the plasma electrons involved in the wake formation do not experience the peak laser potential, reducing their oscillation strength. The fluid model therefore fails in this case for $a_0 \gtrsim 1$.

To quantify these effects, a series of 20 simulations with $a_0 = 0.5 - 4.0$ and varying aspect ratios $w_0/c\tau = 1 - 4$ of the laser pulse are performed; cf. Fig. 5.6. Within this parameter range, $\Delta\lambda = \lambda_{p,nl} - \lambda_p$ obtained from simulation data can be reasonably well described with

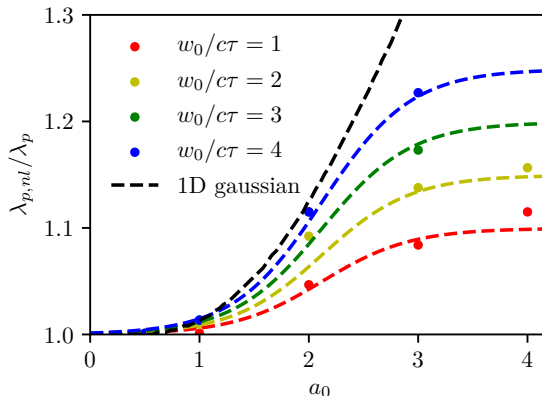


Figure 5.6: Plasma wave elongation according to PIC simulations with different aspect ratios $w_0/c\tau$ of the laser pulse (dots). The fit function (colored dashed lines) agrees well with the simulations, while approaching the 1D nonlinear model for $w_0/c\tau \gg 1$ and $a_0 \gtrsim 2$. Figure reproduced from Ref. [43].

a sigmoid function along a_0 , while the wavelength also increases proportionally to the aspect ratio $w_0/c\tau$:

$$\Delta\lambda(a_0, w_0) = \frac{p_0}{1 + e^{-p_1 \cdot (a_0 - p_2)}} \times \left(1 + \frac{w_0}{c\tau}\right). \quad (5.1)$$

A least-squares fit yields the parameters $p_0 = 0.05$, $p_1 = -2.5$, and $p_2 = 2.1$. The sigmoid's midpoint p_2 of this fit function can be taken to be the value of a_0 at which damping becomes significant. This damping, which is absent in the one-dimensional case, can be explained by the aforementioned effect that the plasma wave is mainly formed by electrons from outer radii. These electrons only interact with the outer part of the laser where the potential is $a \sim 1 - 2$. An increase in a_0 only moves these zones further outwards and leads to a slightly larger transverse bubble size, but it does not substantially increase the peak intensity experienced by the plasma electrons which form the wake. In contrast, for a wider laser the average field experienced by plasma electrons is higher and thus, the plasma wavelength will increase with the aspect ratio.

For even wider drivers, the electron motion becomes more and more longitudinal and the plasma wave formation gradually approaches the solution to the 1D nonlinear wave equation (3.22), and the elongation factor can be $\lambda_{p,nl}/\lambda_p > 1.2$.

On the contrary, the plasma waves driven by tightly (self-)focused drivers clearly differ from the models plotted in Sec. 3.1, and show only a weak increase of the order of 10% in the plasma wavelength, as a_0 is increased. It is important to note that this behavior is not covered by the model of Lu et al. [36], which only concerns the first bubble and not multi bubble trains as shown in Fig. 5.5. The main problem here is that the electrons which form the first bubble are not that same which oscillate in the second and the third. It is therefore important to develop new theoretical models for this regime of wakefield formation, which is central to many future experiments such as multi-pulse wakefield excitation [107, 108].

5.4 Plasma wave evolution in density up-ramp

Discussion so far concentrates on plasma waves in a uniform plasma e.g. the density plateau of a gas jet where the dynamics is dominated by the laser evolution. As outlined in subsection 3.4.1, density gradients will also impact the wave dynamics in a non-uniform plasma; cf. the electron probing work by Zhang et al. [77, 78]. This section presents direct experimental evidence, obtained with few-cycle shadowgraphy, of plasma wave elongation in a density up-ramp.

The left column of figure 5.7 shows snapshots at five different time instances of the propagation of a laser driven plasma wave in a density up-ramp before a shock front. The shock front is produced by inserting a Si wafer into the supersonic flow from a de Laval nozzle; cf. Sec. 3.6.1. The time 0 is defined as the instance when the bubble is located in the region of interest between the dashed yellow lines around $z = -364 \mu\text{m}$, and $z = 0$ represents the starting point of the density plateau i.e. the right edge of the shock front's shadow. By visual inspection, one could already confirm that the plasma wave at a given z elongates as the time passes by.

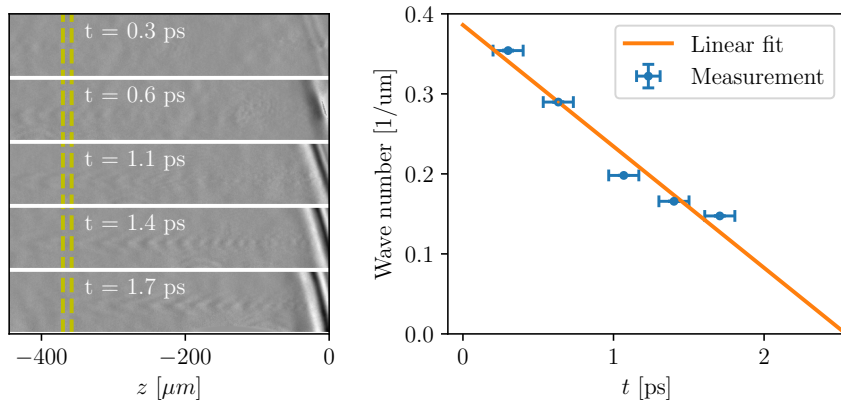


Figure 5.7: *Left:* Few-cycle shadowgrams of laser generated plasma waves in the density up-ramp before a shock front. *Right:* The plasma wave number in dependence of the probe delay t . The wave numbers are measured in the region between the yellow dashed lines in the left panel. Vertical error bars represent standard deviation in the region of interest. Horizontal error bars account for the timing uncertainty originated from the uncertainty in determining the location of the plasma bubble and the shock front.

A quantitative analysis is depicted in the right column, where the ROI-averaged plasma wave number $k_p = 2\pi/\lambda_p$, calculated with continuous wavelet transform [109], is plotted as a function of the probe timing t . Indeed the wave number decreases gradually. As the plasma expands into vacuum at the sound speed, the density profile does not change significantly on a picosecond time scale. Neglecting the plasma density profile evolution, the plasma wave number should change at a constant rate. A linear fit to the data yields

$$k_p [\mu\text{m}^{-1}] = -0.152t [\text{ps}] + 0.386, \quad (5.2)$$

or $\partial k_p / \partial t = -0.152 \mu\text{m}^{-1} \text{ps}^{-1}$. This result is in excellent agreement with the conclusion drawn from the interferometric measurement shown in Fig. 4.12, where a parabolic fit to

the density up-ramp results in $\partial\omega_p/\partial z = 0.152 \mu\text{m}^{-1} \text{ps}^{-1}$. At such a changing rate, the wake reversal effect reported by Zhang et al. [77] should occur within a few picoseconds (the zero-crossing point of the wave number is 2.5 ps), which should be easily verifiable by future experiments employing few-cycle shadowgraphy and a similarly designed gas jet.

5.5 Phase reconstruction and wave amplitude

Besides wavelength, the amplitude i.e. the electron density modulation depth of a plasma wave is of special interest, as it determines the maximal acceleration gradient of the wakefield. According to the 1D cold fluid theory introduced in Sec. 3.1, the wavelength of a plasma wave can be uniquely determined by its amplitude, or vice versa. In an experiment, transverse electron motion (cf. Sec. 5.3) and beam loading [44] make such an association not trivial anymore. Therefore it would be desirable if the the wave amplitude could also be deduced from the shadowgrams.

As shadowgram in essence is a phase contrast measurement, there exist established methods for phase retrieval. The iterative algorithm proposed by Gerchberg and Saxton [110] was employed in this work. Implementation of Gerchberg-Saxton algorithm requires the knowledge of the intensity distributions at two different object planes, which can be obtained either by scanning the imaging lens or by recording the image in multiple image planes after a splitting the beam.

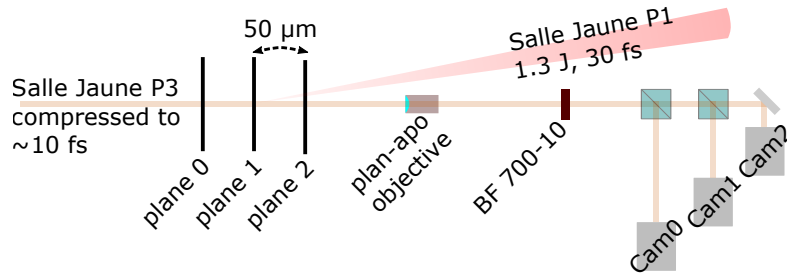


Figure 5.8: Schematic of the multi-plane imaging setup employed at Laboratoire d’Optique Appliquée. Salle Jaune is a Ti:Sapphire laser system delivering 5 J of energy at a repetition rate of 2 Hz. The energy is evenly divided into two main beams P1 and P2, plus a lower energy ($>$ millijoule) probe beam P3. All three beams are fully synchronized, and independently compressible to ~ 30 fs of pulse duration. Plasma waves driven by P1 are probed by P3. Three cameras, labeled as Cam0-3, are set up to image three equally ($50 \mu\text{m}$) spaced plane 0-3, respectively. A bandpass filter BF700-10 is placed in the beam path to enable Gerchberg-Saxton reconstruction of the plasma wave and reduce chromatic aberration.

During the upgrade of ATLAS (Sec. 3.7) to a petawatt system in the summer of 2018, the hollow-core fiber compressor was transported to Laboratoire d’Optique Appliquée (LOA) and was successfully integrated into the Salle Jaune laser system; cf. Fig. 5.8. After probing the laser driven plasma wave, the probe beam was split twice to expose three 16-bit cameras with the same laser shot. The three cameras were set up to image three planes with a separation of $50 \mu\text{m}$ between adjacent planes. Additionally, a bandpass filter transmitting a 10-nm (FWHM) band around the central wavelength of 700 nm was installed in the common path

of the cameras as the Gerchberg-Saxton algorithm is only strictly valid for a monochromatic wave. Furthermore, the narrow bandpass filter reduces the chromatic aberration of the imaging system and improves the shadowgram quality.

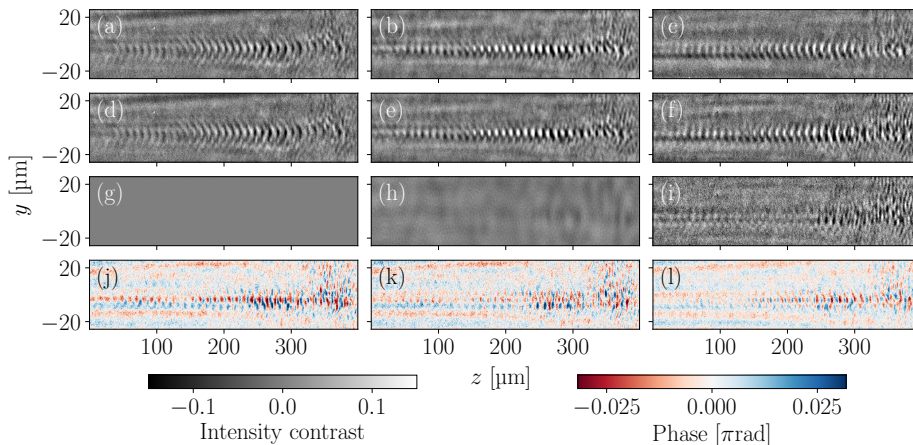


Figure 5.9: Gerchberg-Saxton phase retrieval of a laser driven plasma wave. From left to right, the columns represent the far-, mid- and near-field, respectively. The far- and mid-field data are fed into the algorithm for calculation and the near-field is used as validation. From top to bottom, panels (a-c) are the measured intensities, (d-f) the reconstructed intensities, (g-i) the differences between measurement and reconstruction, (j-l) the reconstructed phases. Note that the iterative intensity substitution stops at the far-field, hence (d) and (a) are identical and (g) is zero everywhere.

An example of Gerchberg-Saxton phase retrieval with the python package LightPipes [111] is shown in Fig. 5.9. After 10 iterations, the retrieved phase in panel (j) already allows to propagate the measured far-field intensity (a or d) back to the mid- (e) and near-field (f) with high fidelity, indicating a successful phase retrieval.

Phase retrieval is only the first step to reconstruct the plasma wave. Deducing the electron density distribution from the phase is the next important yet challenging step, which is beyond the scope of this work. Interested readers are referred to Moritz Förster’s work on this topic.

5.6 Plasma wave gallery

The remaining of this chapter presents some interesting phenomena recorded with few-cycle shadowgraphy, without detailed quantitative analyses.

5.6.1 Plasma waves driven by LWFA electron bunches

During the measurement campaign in LEX photonics, the bunch charge from the laser wakefield accelerator was approaching a nanocoulomb [44]. Taking into account the few femtosecond duration of these bunches [112], a peak current on the order of tens of kiloampere was achieved. Sending such dense LWFA bunches into a second gas jet, it is anticipated that

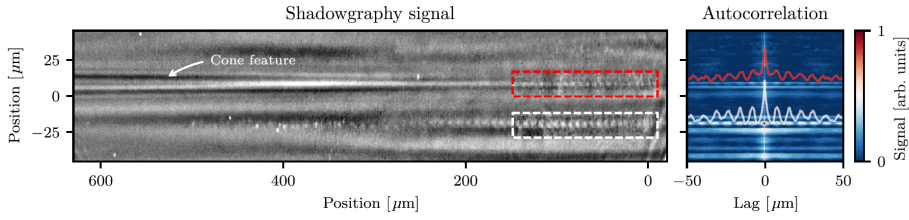


Figure 5.10: *Left*: Few-cycle shadowgram of an LWFA-bunch driven plasma wave. The plasma wave driven the electron bunch is marked with a red rectangle, which is followed by a cone feature as a signature of ion motion described by Gilljohann et al. [42]. The white rectangle marks the wave driven by the remaining laser, with no trailing cone feature. *Right*: Autocorrelation traces of the corresponding plasma waves marked by the rectangles in the left panel, indicating a strong periodic modulation of the observed intensity in the region of interest. Figure reproduced from Ref. [42].

the bunches can drive a strong wakefield on their own. The first direct observation of plasma waves driven by an LWFA-bunch is shown in Fig. 5.10. In this example, two plasma waves can be seen in the shadowgram: one driven by the electron bunch (on top) while the other by the remainder laser (on the bottom). The separation of two waves is caused by the laser refraction due to gas density gradient along the nozzle axis i.e. the vertical direction in the figure. Interestingly, a cone structure is observed trailing the electron-driven plasma wave, which is caused by the ion motion induced by the ponderomotive force associated with the wakefield (see Gilljohann et al. [42] for more detailed discussion).

The result presented above was a collaborative effort led by M. F. Gilljohann and me. While I carried out the measurement of the plasma waves and identified the cone feature as the evidence for the electron-driven wave, Gilljohann performed and interpreted the simulations that unveiled the physics mechanism underlying the cone formation.

5.6.2 Fully broken bubble after shock front injection

Another interesting observation is shown in Fig. 5.11, where the usual wave train structure extending over more than ten wave periods does not appear. Instead, strong diffraction from a single plasma bubble, originally described by Pukhov and Meyer-ter Vehn [9], can be observed. This “lucky” shot was obtained in an experiment studying shock front injection (Subsec. 3.4.1). At the time of writing this thesis, the exact experimental conditions leading to this observation are not fully resolved.

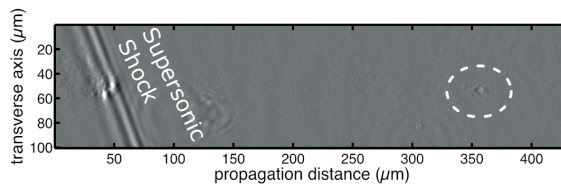


Figure 5.11: Few-cycle shadowgram of a fully broken plasma bubble.

5.6.3 Bubble shape change in colliding pulse injection

Picking off a portion of ATLAS beam and sending it to counter-propagate and collide with the ATLAS main beam, a sequence of shadowgraphic snapshots was recorded near the point where the colliding pulses injection (Subsec. 3.4.3) takes place; see Fig. 5.12. The apparent shape of the bubble changed after the injection event: a crescent-shaped shadow with a curvature opposite to all other wave periods appeared. This shadow suggests that the density gradient at the leading edge becomes much sharper, likely due to the laser steepening during the collision process.

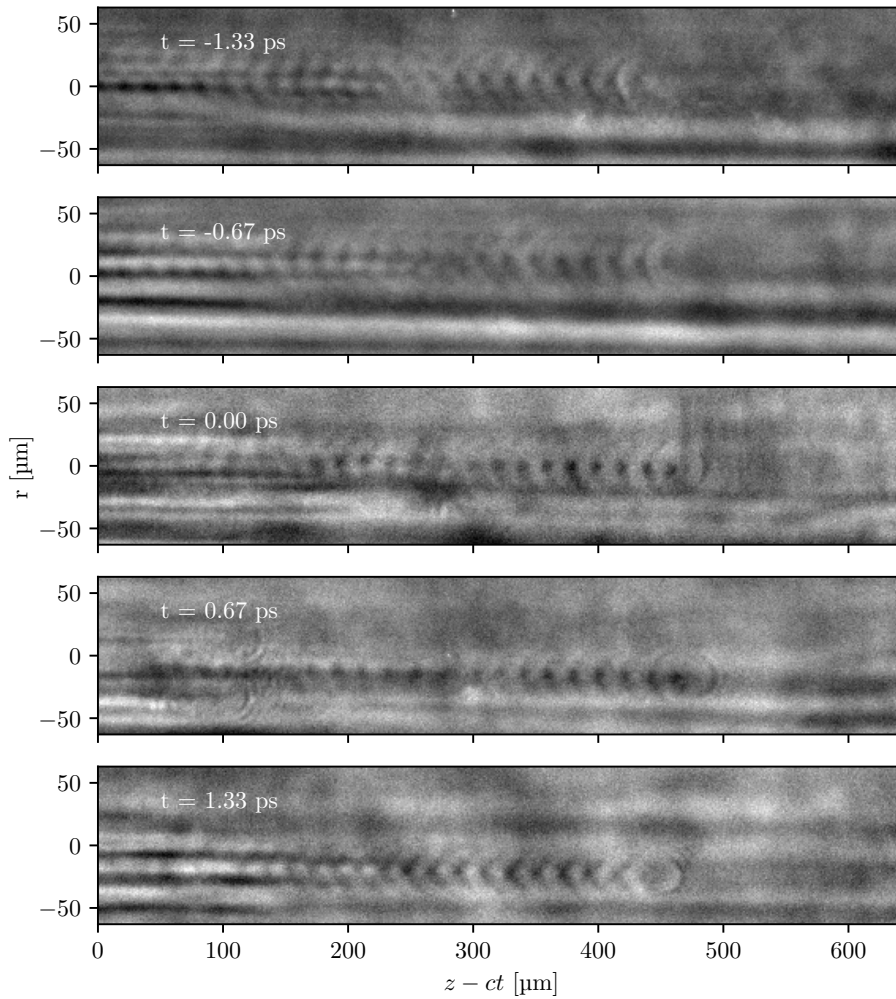


Figure 5.12: Change of bubble shape at five time instances during colliding pulse injection. $t = 0$ is the injection time. For $t < 0$, i.e., before the colliding point, the first wave period appears as a dark accompanied by a crescent-shaped shadow, very similar to the trailing periods. In contrast, a crescent-shaped shadow with inverted curvature appears at the leading edge of the first plasma bucket $t \geq 0$, indicating a steepening of density gradient after injection takes place.

5.6.4 Off-center plasma wave

Sometimes, when things go wrong, plasma waves can give a first hint. An example is given below in Fig. 5.13, where the plasma wave train does not appear along the symmetry axis as one would normally expect. Instead, it is offset by roughly a quarter the transverse size of the observed plasma plume. This offset suggests strong asymmetry of the laser pulse, which was corrected by a tuning of the pulse front tilt [55] and subsequent alignment of the final off-axis parabolic mirror.

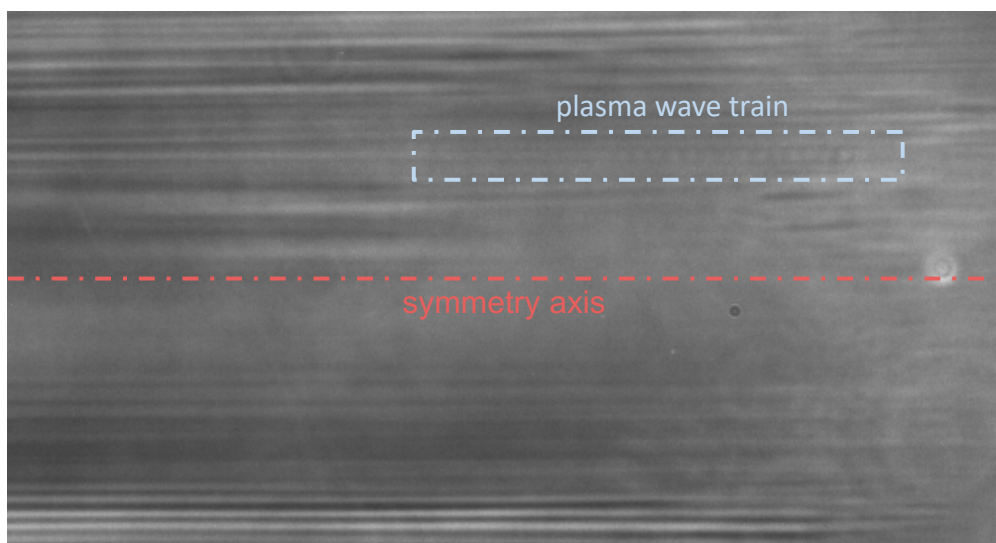


Figure 5.13: Shadowgram of an off-axis plasma wave, suggesting strong pulse front tilt and misalignment of the final focusing optic.

6 Summary and outlook

In summary, this thesis made two advancements: development of diagnostic tools for the laser wakefield acceleration (LWFA) experiments powered by the ATLAS-300 laser facility at the Laboratory for Extreme (LEX) Photonics described in Chapter 4, and studies of laser-driven plasma waves using few-cycle shadowgraphy as the central tool presented in Chapter 5.

Diagnostic tools developed in the framework of this thesis, including calibrated scintillating screen, magnetic spectrometer, Nomarski interferometer, and the few-cycle shadowgraphy setup, made significant contribution to the success of the LWFA activities at LEX photonics. They provided knowledge of the plasma wavelength and density, as well as electron beam charge, pointing, and spectral density in absolute terms. This enabled quantitative comparison of experiments, theories, and numerical simulations, from which sparked numerous important results. To name a few examples: electron acceleration with steady-flow gas cell producing double bunches with the high-energy bunch containing > 100 pC of charge above the (tunable) energy of 1 GeV (Sec 3.8); laser-particle hybrid wakefield experiment demonstrating the first observation of LWFA-bunch-driven plasma waves and ion dynamics [42]; studies on beam loading effects in laser-driven wakefields [44]; and the main finding of this thesis: a scaling law for the nonlinear plasma wavelength [43].

Combining the plasma wavelength obtained from few-cycle shadowgrams and the plasma density deduced from on-shot interferograms, it is demonstrated that the analytical- [8] and phenomenological models [37] currently available are insufficient to capture all important physics in the nonlinear lengthening of laser-driven plasma waves. Especially in the regime most relevant to experiments, weakly nonlinear plasma waves are driven by tightly focused laser pulses, hence transverse electron motion contributes significantly to the plasma wave formation. A new scaling law is proposed based on a series of particle-in-cell (PIC) simulations (cf. Ref. [43] and Chapter 5), which accounts for both the laser peak intensity (quantified by its associated a_0) and the laser spot aspect ratio (characterized by $w_0/c\tau$). Given its excellent agreement with the measurement, this new scaling law can be used to guide the design of future experiments where multiple pulses will be required to drive the wakefield—to determine the delay between pulses particularly.

There are several aspects that can be considered as natural continuation or short-term outlook of the current work. Below are some examples.

- **Multi-plane shadowgraphy—plasma wave density reconstruction**

As alluded in Chapter. 5, reconstruction of the plasma wave density modulation from experimental observables is an important milestone toward the understanding and

control of the LWFA process. Few-cycle shadowgraphy proves to be a powerful tool in this respect. The multi-plane shadowgraphy technique and Gerchberg-Saxton phase retrieval outlined in section 5.5 mark the first step of reconstructing the plasma density modulation. What remains is the inversion of the projected phase into 3D density. Initial analyses by Förster et al. [113] have shown inspiring results: density modulation has been successfully reconstructed for a linear plasma wave with cylindrical symmetry using e.g. Abel inversion.

- **Single-shot recording of plasma wave evolution**

The interaction between the probe beam and the laser-driven plasma wave is described by linear refraction, given the probe beam is weak enough to not perturb the plasma under probing. The superposition principle implies that different spectral components of a chirped probe pulse (cf. subsection. 2.1.1) can be considered as independent probe pulses arriving at different time instances. It is hence possible to record the plasma wave evolution in a single shot by intentionally chirping the probe pulse and simultaneously measuring multiple spectral bands. Note that the temporal resolution of probing is not limited by the spectrally integrated duration, which is elongated by the chirp of the probe pulse. Instead, it is the coherent time of the spectral band of interest, which is determined solely by the bandwidth, that limits the temporal resolution. Intuitively, a higher temporal resolution demands a broader spectrum.

Techniques based on similar principle were previously employed to characterize ultra-short laser pulses. For example, STRIPED FISHⁱ developed at the Trebino group at Georgia Institute of Technology makes use of holograms for a complete spatial-temporal reconstruction of a laser pulse [114]; in contrast, TRICⁱⁱ developed by the Schreiber group at LMU Munich relies on the expansion of near-critical-density plasma to map out the laser intensity contours in the focal region [115].

- **Correlating diagnostics**

Each individual diagnostic tool introduced in this thesis has its strengths and can be useful by its own. However, richer physics can be explored when multiple diagnostic tools are correlated. For example, Swanson et al. [116] showed that the electron beam pointing is correlated with the shock front angle by actively changing the orientation of the whole target assembly during the experiment. Since the shock front angle can be directly deduced from shadowgrams, this hints at a non-invasive way to monitor the e-beam pointing, which could enable correcting the pointing-induced beam energy uncertainty without spoiling the beam by inserting a pointing screen.

Researches outlined above can be carried out at the ATLAS-3000 laser system at the Centre for Advanced Laser Applications (CALA) with minor (or no) modifications to the existing hardware.

Going forward, with ATLAS-3000 reaching full-power operation, it is anticipated that a plasma density in the range of 10^{17} cm^{-3} will be necessary [12]. At such low densities, the contrast of the few-cycle shadowgram is likely to suffer, because the gradient of refractive

ⁱSpatially and Temporally Resolved Intensity and Phase Evaluation Device: Full Information from a Single Hologram

ⁱⁱTemporally Resolved Intensity Contouring

index is diminishing at the current wavelength of the probe pulse. Sävert [45] proposed to use a longer probe wavelength to recover the shadowgram contrast, e.g. by frequency down-converting the probe pulse to mid-IR. This approach requires mid-IR detectors with sufficient spatial resolution that are yet to be developed.

In longer terms, the field of LWFA research could benefit from the rapid development of the fiber laser technology, and from arguably the hottest topic of the present time—machine learning (ML).

Fiber lasers, compared with the Ti:sapphire lasers used in this work, excels in the average-power scalability. The low quantum defectⁱⁱⁱ and the large surface-to-volume ratio due to the quasi-1D geometry make fiber lasers less demanding to cool.^{iv} They can readily deliver kilowatts of average power by operating at multi-kHz repetition rate [117]. Techniques such as coherent combining of output of multiple fibers [118, 119] can further push the peak power to meet the requirement of LWFA research, making fiber lasers a promising candidate to power next-generation accelerators.

Another major boost to the LWFA research is likely to emerge from implementation of contemporary ML techniques. Several groups have successfully utilized ML schemes such as Bayesian optimization [120, 121] for the automated optimization of the LWFA operation. Such advances would eventually relieve physicists from the mundane yet time-consuming (sometimes impossible) task of manual optimization in a multi-dimensional parameter space. Furthermore, as the community moves towards advanced control and inference based on statistical analyses [44, 122], non-trivial correlations among parameters found through ML could enable virtual diagnostics [123].

ⁱⁱⁱFor example, Yb-doped fibers can lase at 1030 nm while being pumped at 980 nm. In contrast, Ti:sapphire needs ~ 500 nm pump to lase around 800 nm.

^{iv}Beside the physics limit of quantum defect, there are also technological limitations for further up-scaling Ti:sapphire systems. One thing particular is that the lasers used to pump the Ti:sapphire crystal, usually a frequency-doubled Nd:YAG laser, rely on flash-lamp pumping, whose electrical-to-optical efficiency is typically below one percent.

List of Figures

2.1	Pulses with identical spectral amplitude and various spectral phase.	7
2.2	Electron motion in a plane wave in the relativistic regime	12
2.3	Electron trajectory in a laser pulse	13
2.4	Schematic representation of strong-field ionization mechanisms	15
3.1	Electric field distribution of a linear plasma wave	26
3.2	Comparison of 1D linear and nonlinear plasma waves	27
3.3	Comparison of nonlinear plasma wavelength scalings.	28
3.4	Extension of 1D nonlinear wakefield theory to 3D for a wide driver.	29
3.5	Stationary phase space orbits of electrons in the wakefield	31
3.6	Trapping threshold for various conditions	32
3.7	Schematic representation of 2D wave breaking scenarios.	34
3.8	Schematic representation of shock front injection	36
3.9	High-quality electron beams generated with shock front injection	37
3.10	Illustration of colliding pulse injection	39
3.11	Schematic overview of experimental setup	42
3.12	Illustration of an oblique shock	44
3.13	Schematic of ATLAS 300 layout	45
3.14	GeV electrons from a variable length gas cell	46
3.15	Analyses of the high energy peak	47
3.16	Evolution of bunch charge and beam energy	48
4.1	Setup for absolute calibration of scintillating screens	51

List of Figures

4.2	Absolute calibration of scintillating screens	52
4.3	Decay history of GTLSs in LEX photonics	55
4.4	Results from the pointing screen	56
4.5	Schematic of the magnetic spectrometer	57
4.6	Rendering of the spectrometer magnet	57
4.7	Spectrometer images, with and without the pointing screen	58
4.8	Energy calibration of the magnetic spectrometer	59
4.9	Focusing of the 2.1 m magnet	60
4.10	Schematic of Nomarski interferometer	61
4.11	Raw data from a Nomarski interferometer.	61
4.12	Interferometric measurement of gas jet density.	62
5.1	Schematic of the pump-probe setup.	65
5.2	An example raw shadowgram.	66
5.3	Comparison between linear and nonlinear plasma waves	67
5.4	Simulation of propagation of a 70 TW pulse	69
5.5	Comparison of plasma waves driven by a wide spot and a tightly focused spot	71
5.6	Empirical scaling of plasma wave lengthening	72
5.7	Evolution of plasma wave in a density upramp.	73
5.8	Schematic of setup employed at LOA.	74
5.9	Gerchberg-Saxton phase retrieval of plasma wave.	75
5.10	Few-cycle shadowgram of an LWFA-bunch driven plasma wave	76
5.11	Few-cycle shadowgram of a fully broken bubble.	76
5.12	Change of bubble shape during colliding pulse injection.	77
5.13	Shadowgram of an off-axis plasma wave.	78

List of Tables

2.1	Ionization threshold of selected ions	16
3.1	Summary of natural units and normalization.	23
4.1	Absolute calibration of scintillating screens	53
5.1	Various estimates for the laser a_0 in an experiment	68

Bibliography

- [1] The ATLAS Collaboration. Observation of a new particle in the search for the Standard Model Higgs boson with the ATLAS detector at the LHC. *Physics Letters, Section B: Nuclear, Elementary Particle and High-Energy Physics*, 716(1):1–29, 2012.
- [2] The CMS collaboration. Observation of a new boson at a mass of 125 GeV with the CMS experiment at the LHC. *Physics Letters B*, 716(1):30–61, 2012.
- [3] The CMS Collaboration. Evidence for the direct decay of the 125 GeV Higgs boson to fermions. *Nature Physics*, 10(8):557–560, 2014.
- [4] Robert W. Hamm and Marianne E. Hamm. The beam business: Accelerators in industry. *Physics Today*, 64(6):46–51, 2011.
- [5] E. A Peralta, K Soong, R. J England, E. R Colby, Z Wu, B. Montazeri, C. McGuinness, J. McNeur, K. J. Leedle, D. Walz, E. B. Sozer, B. Cowan, B. Schwartz, G. Travish, and R. L. Byer. Demonstration of electron acceleration in a laser-driven dielectric microstructure. *Nature*, 503(7474):91–94, 2013.
- [6] Toshiki Tajima and John M. Dawson. Laser Electron Accelerator. *Physical Review Letters*, 43(4):267–270, 1979.
- [7] Donna Strickland and Gerard Mourou. Compression of amplified chirped optical pulses. *Optics Communications*, 56(3):219–221, 1985.
- [8] E. Esarey, C. Schroeder, and W. Leemans. Physics of laser-driven plasma-based electron accelerators. *Reviews of Modern Physics*, 81(3):1229–1285, 2009.
- [9] Alexander Pukhov and Jürgen Meyer-ter Vehn. Laser wake field acceleration: the highly non-linear broken-wave regime. *Applied Physics B: Lasers and Optics*, 74(4-5): 355–361, 2002.
- [10] X. Wang, R. Zgadzaj, N. Fazel, S. A. Yi, X. Zhang, W. Henderson, Y.-Y. Chang, R. Korzekwa, H.-E. Tsai, C.-H. Pai, Z. Li, H. Quevedo, G. Dyer, E. Gaul, M. Martinez, A. Bernstein, T. Borger, M. Spinks, M. Donovan, S. Y. Kalmykov, V. Khudik, G. Shvets, T. Ditmire, and M. C. Downer. Petawatt-laser-driven wakefield acceleration of electrons to 2 GeV in 10^{17} cm⁻³ plasma. In *AIP Conference Proceedings*, volume 1507, pages 341–344, 2013.
- [11] Hyung Taek Kim, V. B. Pathak, Ki Hong Pae, A. Lifschitz, F. Sylla, Jung Hun Shin, C. Hojbota, Seong Ku Lee, Jae Hee Sung, Hwang Woon Lee, E. Guillaume, C. Thaury,

- Kazuhisa Nakajima, J. Vieira, L. O. Silva, V. Malka, and Chang Hee Nam. Stable multi-GeV electron accelerator driven by waveform-controlled PW laser pulses. *Scientific Reports*, 7(1):1–8, 2017.
- [12] A. J. Gonsalves, K. Nakamura, J. Daniels, C. Benedetti, C. Pieronek, T. C.H. De Raadt, S. Steinke, J. H. Bin, S. S. Bulanov, J. Van Tilborg, C. G.R. Geddes, C. B. Schroeder, Cs Tóth, E. Esarey, K. Swanson, L. Fan-Chiang, G. Bagdasarov, N. Bobrova, V. Gasilov, G. Korn, P. Sasorov, and W. P. Leemans. Petawatt Laser Guiding and Electron Beam Acceleration to 8 GeV in a Laser-Heated Capillary Discharge Waveguide. *Physical Review Letters*, 122(8):84801, 2019.
- [13] S. Bulanov, N. Naumova, F. Pegoraro, and J. Sakai. Particle injection into the wave acceleration phase due to nonlinear wake wave breaking. *Physical Review E - Statistical Physics, Plasmas, Fluids, and Related Interdisciplinary Topics*, 58(5):R5257–R5260, 1998.
- [14] H. Suk, N. Barov, J. B. Rosenzweig, and E. Esarey. Plasma electron trapping and acceleration in a plasma wake field using a density transition. *Physical Review Letters*, 86(6):1011–1014, 2001.
- [15] C. G.R. Geddes, K. Nakamura, G. R. Plateau, Cs Toth, E. Cormier-Michel, E. Esarey, C. B. Schroeder, J. R. Cary, and W. P. Leemans. Plasma-density-gradient injection of low absolute-momentum-spread electron bunches. *Physical Review Letters*, 100(21):215004, 2008.
- [16] K. Schmid, A. Buck, C. M.S. Sears, J. M. Mikhailova, R. Tautz, D. Herrmann, M. Geissler, F. Krausz, and L. Veisz. Density-transition based electron injector for laser driven wakefield accelerators. *Physical Review Special Topics - Accelerators and Beams*, 13(9):91301, 2010.
- [17] A. Buck, J. Wenz, J. Xu, K. Khrennikov, K. Schmid, M. Heigoldt, J. M. Mikhailova, M. Geissler, B. Shen, F. Krausz, S. Karsch, and L. Veisz. Shock-front injector for high-quality laser-plasma acceleration. *Physical Review Letters*, 110(18):185006, 2013. doi: 10.1103/PhysRevLett.110.185006.
- [18] E. Oz, S. Deng, T. Katsouleas, P. Muggli, C. D. Barnes, I. Blumenfeld, F. J. Decker, P. Emma, M. J. Hogan, R. Ischebeck, R. H. Iverson, N. Kirby, P. Krejcik, C. O’connell, R. H. Siemann, D. Walz, D. Auerbach, C. E. Clayton, C. Huang, D. K. Johnson, C. Joshi, W. Lu, K. A. Marsh, W. B. Mori, and M. Zhou. Ionization-induced electron trapping in ultrarelativistic plasma wakes. *Physical Review Letters*, 98(8):84801, 2007.
- [19] M. Chen, E. Esarey, C. B. Schroeder, C. G.R. Geddes, and W. P. Leemans. Theory of ionization-induced trapping in laser-plasma accelerators. *Physics of Plasmas*, 19(3):33101, 2012.
- [20] M. Zeng, M. Chen, Z.-M. Sheng, W. B. Mori, and J. Zhang. Self-truncated ionization injection and consequent monoenergetic electron bunches in laser wakefield acceleration. *Physics of Plasmas*, 21(3):30701, 2014.

- [21] M. Mirzaie, S. Li, M. Zeng, N. A. M. Hafz, M. Chen, G. Y. Li, Q. J. Zhu, H. Liao, T. Sokollik, F. Liu, Y. Y. Ma, L.M. Chen, Z. M. Sheng, and J. Zhang. Demonstration of self-truncated ionization injection for GeV electron beams. *Scientific Reports*, 5(1): 14659, 2015.
- [22] J. P. Couperus, R. Pausch, A. Köhler, O. Zarini, J. M. Krämer, M. Garten, A. Huebl, R. Gebhardt, U. Helbig, S. Bock, K. Zeil, A. Debus, M. Bussmann, U. Schramm, and A. Irman. Demonstration of a beam loaded nanocoulomb-class laser wakefield accelerator. *Nature Communications*, 8(1):1–7, 2017.
- [23] N. Bourgeois, J. Cowley, and S. M. Hooker. Two-pulse ionization injection into quasi-linear laser wakefields. *Physical Review Letters*, 111(15):155004, 2013.
- [24] M. Zeng, M. Chen, L.-L. Yu, W. B. Mori, Z.-M. Sheng, B. Hidding, D. Jaroszynski, and J. Zhang. Multi-chromatic narrow-energy-spread electron bunches from laser wakefield acceleration with dual-color lasers. *Physical Review Letters*, 114(8):1–5, 2014.
- [25] J. Faure, C. Rechatin, A. Norlin, A. Lifschitz, Y. Glinec, and V. Malka. Controlled injection and acceleration of electrons in plasma wakefields by colliding laser pulses. *Nature*, 444(7120):737–739, 2006. ISSN 0028-0836.
- [26] S. Corde, K. Ta Phuoc, G. Lambert, R. Fitour, V. Malka, A. Rousse, A. Beck, and E. Lefebvre. Femtosecond x rays from laser-plasma accelerators. *Reviews of Modern Physics*, 85(1):1–48, 2013.
- [27] K. Khrennikov, J. Wenz, A. Buck, J. Xu, M. Heigoldt, L. Veisz, and S. Karsch. Tunable all-optical quasimonochromatic Thomson X-ray source in the nonlinear regime. *Physical Review Letters*, 114(19):1–5, 2015.
- [28] A. Döpp, B. Mahieu, A. Lifschitz, C. Thaury, A. Doche, E. Guillaume, G. Grittani, O. Lundh, M. Hansson, J. Gautier, M. Kozlova, J. P. Goddet, P. Rousseau, A. Tafzi, V. Malka, A. Rousse, S. Corde, and K. Ta Phuoc. Stable femtosecond X-rays with tunable polarization from a laser-driven accelerator. *Light: Science & Applications*, 6(11):e17086–e17086, 2017.
- [29] J. Wenz, S. Schleede, K. Khrennikov, M. Bech, P. Thibault, M. Heigoldt, F. Pfeiffer, and S. Karsch. Quantitative X-ray phase-contrast microtomography from a compact laser-driven betatron source. *Nature Communications*, 6:1–6, 2015.
- [30] A. Döpp, L. Hehn, J. Götzfried, J. Wenz, M. Gilljohann, H. Ding, S. Schindler, F. Pfeiffer, and S. Karsch. Quick x-ray microtomography using a laser-driven betatron source. *Optica*, 5(2):199–203, 2018.
- [31] B. Mahieu, N. Jourdain, K. Ta Phuoc, F. Dorchie, J. P. Goddet, A. Lifschitz, P. Renaudin, and L. Lecherbourg. Probing warm dense matter using femtosecond X-ray absorption spectroscopy with a laser-produced betatron source. *Nature Communications*, 9(1):1–6, 2018.
- [32] J. C. Wood, D. J. Chapman, K. Poder, N. C. Lopes, M. E. Rutherford, T. G. White, F. Albert, K. T. Behm, N. Booth, J. S.J. Bryant, P. S. Foster, S. Glenzer, E. Hill,

- K. Krushelnick, Z. Najmudin, B. B. Pollock, S. Rose, W. Schumaker, R. H.H. Scott, M. Sherlock, A. G.R. Thomas, Z. Zhao, D. E. Eakins, and S. P.D. Mangles. Ultrafast Imaging of Laser Driven Shock Waves using Betatron X-rays from a Laser Wakefield Accelerator. *Scientific Reports*, 8(1):11010, 2018.
- [33] M. Oppelt, M. Baumann, R. Bergmann, E. Beyreuther, K. Brüchner, J. Hartmann, L. Karsch, M. Krause, L. Laschinsky, E. Leßmann, M. Nicolai, M. Reuter, C. Richter, A. Sävert, M. Schnell, M. Schürer, J. Woithe, M. Kaluza, and J. Pawelke. Comparison study of in vivo dose response to laser-driven versus conventional electron beam. *Radiation and Environmental Biophysics*, 54(2):155–166, 2015.
- [34] S. V. Bulanov, F. Pegoraro, A. M. Pukhov, and A. S. Sakharov. Transverse-Wake Wave Breaking. *Physical Review Letters*, 78(22):4205–4208, 1997.
- [35] W. Lu, M. Tzoufras, C. Joshi, F. S. Tsung, W. B. Mori, J. Vieira, R. A. Fonseca, and L. O. Silva. Generating multi-GeV electron bunches using single stage laser wakefield acceleration in a 3D nonlinear regime. *Physical Review Special Topics - Accelerators and Beams*, 10(6):61301, 2007.
- [36] W. Lu, C. Huang, M. Zhou, M. Tzoufras, F. S. Tsung, W. B. Mori, and T. Katsouleas. A nonlinear theory for multidimensional relativistic plasma wave wakefields. *Physics of Plasmas*, 13(5):56709, 2006.
- [37] W. Lu, C. Huang, M. Zhou, W. B. Mori, and T. Katsouleas. Nonlinear theory for relativistic plasma wakefields in the blowout regime. *Physical Review Letters*, 96(16):165002, 2006.
- [38] A. F. Lifschitz, X. Davoine, E. Lefebvre, J. Faure, C. Rechatin, and V. Malka. Particle-in-Cell modelling of laser-plasma interaction using Fourier decomposition. *Journal of Computational Physics*, 228(5):1803–1814, 2009.
- [39] R. Lehe, M. Kirchen, I. A. Andriyash, B. B. Godfrey, and J. L. Vay. A spectral, quasi-cylindrical and dispersion-free Particle-In-Cell algorithm. *Computer Physics Communications*, 203(24):66–82, 2016.
- [40] A. Sävert, S. P. D. Mangles, M. Schnell, E. Siminos, J. M. Cole, M. Leier, M. Reuter, M. B. Schwab, M. Möller, K. Poder, O. Jäckel, G. G. Paulus, C. Spielmann, S. Skupin, Z. Najmudin, and M. C. Kaluza. Direct Observation of the Injection Dynamics of a Laser Wakefield Accelerator Using Few-Femtosecond Shadowgraphy. *Physical Review Letters*, 115(5):055002, 2015.
- [41] M. C. Downer, R. Zgadzaj, A. Debus, U. Schramm, and M. C. Kaluza. Diagnostics for plasma-based electron accelerators. *Reviews of Modern Physics*, 90(3):35002, 2018.
- [42] M. F. Gilljohann, H. Ding, A. Döpp, J. Götzfried, S. Schindler, G. Schilling, S. Corde, A. Debus, T. Heinemann, B. Hidding, S. M. Hooker, A. Irman, O. Kononenko, T. Kurz, A. Martinez De La Ossa, U. Schramm, and S. Karsch. Direct Observation of Plasma Waves and Dynamics Induced by Laser-Accelerated Electron Beams. *Physical Review X*, 9(1):11046, 2019.

- [43] H. Ding, A. Döpp, M. F. Gilljohann, J. Götzfried, S. Schindler, L. Wildgruber, G. Cheung, S. M. Hooker, and S. Karsch. Nonlinear plasma wavelength scalings in a laser wakefield accelerator. *Physical Review E*, 101(2):23209, 2020.
- [44] J. Götzfried, A. Döpp, M. F. Gilljohann, F. M. Foerster, H. Ding, S. Schindler, G. Schilling, A. Buck, L. Veisz, and S. Karsch. Physics of High-Charge Electron Beams in Laser-Plasma Wakefields. *Physical Review X*, 10(4):041015, 2020.
- [45] Alexander Sävert. *Few-cycle microscopy of a laser wakefield accelerator*. PhD thesis, Friedrich-Schiller Universität Jena, 2016.
- [46] Richard P. Feynman, Robert B. Leighton, and Matthew Sands. The Feynman Lectures on Physics, New Millennium Edition, Vol. II: Mainly Electromagnetism and Matter.
- [47] Julius O. Smith. *Mathematics of the Discrete Fourier Transform (DFT)*. W3K Publishing, 2007.
- [48] Stefan Skupin. Lecture notes on fundamentals of modern optics, 2011.
- [49] Louis G. Gouy. *Sur une propriété nouvelle des ondes lumineuses*. Mélanges scientifiques. Gauthier-Villars, 1890.
- [50] Matthias Heigoldt. *Temporal dynamics of the longitudinal bunch profile in a laser wakefield accelerator*. PhD thesis, Ludwig-Maximilians-Universität München, 2017.
- [51] E. A. Startsev and C. J. McKinstrie. Multiple scale derivation of the relativistic ponderomotive force. *Physical Review E - Statistical Physics, Plasmas, Fluids, and Related Interdisciplinary Topics*, 55(6):7527–7535, 1997.
- [52] John D. Jackson. *Classical Electrodynamics*. John Wiley & Sons, 3rd edition, 1998.
- [53] Jens Osterhoff. *Stable , ultra-relativistic electron beams by laser-wakefield acceleration*. PhD thesis, Ludwig-Maximilians-Universität München, 2009.
- [54] Emmy Noether. Invariant variation problems. *Transport Theory and Statistical Physics*, 1(3):186–207, 1971.
- [55] Antonia Popp. *Dynamics of electron acceleration in laser-driven wakefields: Acceleration limits and asymmetric plasma waves*. PhD thesis, Ludwig-Maximilians-Universität München, 2011.
- [56] E. S. Sarachik and G. T. Schappert. Classical theory of the scattering of intense laser radiation by free electrons. *Physical Review D*, 1(10):2738–2753, 1970.
- [57] C. I. Moore, J. P. Knauer, and D. D. Meyerhofer. Observation of the transition from Thomson to Compton scattering in multiphoton interactions with low-energy electrons. *Physical Review Letters*, 74(13):2439–2442, 1995.
- [58] LV Keldysh. Ionization in the field of a strong electromagnetic wave. *Sov. Phys. JETP*, 20(5):1307–1314, 1965.
- [59] Paul Gibbon. *Short Pulse Laser Interactions with Matter*. Imperial College Press, London, 2005.

- [60] Francis F. Chen. *Introduction to Plasma Physics and Controlled Fusion*. Springer International Publishing, 3rd edition, 2016.
- [61] W. B. Mori. The physics of the nonlinear optics of plasmas at relativistic intensities for short-pulse lasers. *IEEE Journal of Quantum Electronics*, 33(11):1942–1953, 1997.
- [62] A. J. Gonsalves, K. Nakamura, C. Lin, J. Osterhoff, S. Shiraishi, C. B. Schroeder, C. G.R. Geddes, Cs. Tóth, E. Esarey, and W. P. Leemans. Plasma channel diagnostic based on laser centroid oscillations. *Physics of Plasmas*, 17(5):56706, 2010.
- [63] A A Vlasov. The vibrational properties of an electron gas. *Soviet Physics Uspekhi*, 10(6):721–733, 1968.
- [64] John M. Dawson. Nonlinear Electron Oscillations in a Cold Plasma. *Physical Review*, 113(2):383–387, 1959.
- [65] T. Matsuoka, C. McGuffey, P. G. Cummings, Y. Horovitz, F. Dollar, V. Chvykov, G. Kalintchenko, P. Rousseau, V. Yanovsky, S. S. Bulanov, A. G.R. Thomas, A. Maksimchuk, and K. Krushelnick. Stimulated Raman Side Scattering in Laser Wakefield Acceleration. *Physical Review Letters*, 105(3):034801, 2010.
- [66] J. Faure. Plasma injection schemes for laser-plasma accelerators. *CAS-CERN Accelerator School: Plasma Wake Acceleration 2014, Proceedings*, pages 143–157, 2014.
- [67] A. Akhiezer and R. Polovin. Theory of Wave Motion of an Electron Plasma. *Soviet Phys. JETP*, Vol: 3(5):696, 1956.
- [68] T. P. Coffey. Breaking of Large Amplitude Plasma Oscillations. *Physics of Fluids*, 14(7):1402, 1971.
- [69] T. Katsouleas and W. B. Mori. Wave-breaking amplitude of relativistic oscillations in a thermal plasma. *Physical Review Letters*, 61(1):90–93, 1988.
- [70] S. Corde, C. Thaury, A. Lifschitz, G. Lambert, K. Ta Phuoc, X. Davoine, R. Lehe, D. Douillet, A. Rousse, and V. Malka. Observation of longitudinal and transverse self-injections in laser-plasma accelerators. *Nature Communications*, 4:1501–1507, 2013.
- [71] A. Modena, Z. Najmudin, A. E. Dangor, C. E. Clayton, K. A. Marsh, C. Joshi, V. Malka, C. B. Darrow, C. Danson, D. Neely, and F. N. Walsh. Electron acceleration from the breaking of relativistic plasma waves. *Nature*, 377(6550):606–608, 1995.
- [72] V. Malka, S. Fritzler, E. Lefebvre, M. M. Aleonard, F. Burgy, J. P. Chambaret, J. F. Chemin, K. Krushelnick, G. Malka, S. P.D. Mangles, Z. Najmudin, M. Pittman, J. P. Rousseau, J. N. Scheurer, B. Walton, and A. E. Dangor. Electron acceleration by a wake field forced by an intense ultrashort laser pulse. 298(5598):1596–1600, 2002.
- [73] J. M. Cole, K. T. Behm, E. Gerstmayr, T. G. Blackburn, J. C. Wood, C. D. Baird, M. J. Duff, C. Harvey, A. Ilderton, A. S. Joglekar, K. Krushelnick, S. Kuschel, M. Marklund, P. McKenna, C. D. Murphy, K. Poder, C. P. Ridgers, G. M. Samarin, G. Sarri, D. R. Symes, A. G. R. Thomas, J. Warwick, M. Zepf, Z. Najmudin, and S. P. D. Mangles.

- Experimental evidence of radiation reaction in the collision of a high-intensity laser pulse with a laser-wakefield accelerated electron beam. *Phys. Rev. X*, 8:011020, 2018.
- [74] C. G.R. Geddes, Cs Toth, J. van Tilborg, E. Esarey, C. B. Schroeder, D. Bruhwiler, C. Nieter, J. Cary, and W. P. Leemans. High-quality electron beams from a laser wakefield accelerator using plasma-channel guiding. *Nature*, 431(7008):538–541, 2004.
- [75] J. Faure, Y. Glinec, A. Pukhov, S. Klselev, S. Gordienko, E. Lefebvre, J. P. Rousseau, F. Burgy, and V. Malka. A laser-plasma accelerator producing monoenergetic electron beams. *Nature*, 431(7008):541–544, 2004.
- [76] S. P.D. Mangles, C. D. Murphy, Z. Najmudin, A. G.R. Thomas, J. L. Collier, A. E. Dangor, E. J. Divall, P. S. Foster, J. G. Gallacher, C. J. Hooker, D. A. Jaroszynski, A. J. Langley, W. B. Mori, P. A. Norreys, F. S. Tsung, R. Viskup, B. R. Walton, and K. Krushelnick. Monoenergetic beams of relativistic electrons from intense laser-plasma interactions. *Nature*, 431(7008):535–538, 2004.
- [77] C. J. Zhang, J. F. Hua, Y. Wan, C. H. Pai, B. Guo, J. Zhang, Y. Ma, F. Li, Y. P. Wu, H. H. Chu, Y. Q. Gu, X. L. Xu, W. B. Mori, C. Joshi, J. Wang, and W. Lu. Femtosecond Probing of Plasma Wakefields and Observation of the Plasma Wake Reversal Using a Relativistic Electron Bunch. *Physical Review Letters*, 119(6):1–6, 2017.
- [78] C. J. Zhang, Y. Wan, B. Guo, J. F. Hua, C. H. Pai, F. Li, J. Zhang, Y. Ma, Y. P. Wu, X. L. Xu, W. B. Mori, H. H. Chu, J. Wang, W. Lu, and C. Joshi. Probing plasma wakefields using electron bunches generated from a laser wakefield accelerator. *Plasma Physics and Controlled Fusion*, 60(4):0, 2018.
- [79] S. Schindler, A. Döpp, H. Ding, M. Gilljohann, J. Götzfried, and S. Karsch. Tunable X-ray source by Thomson scattering during laser-wakefield acceleration. In *Laser Acceleration of Electrons, Protons, and Ions V*, number April, page 22. SPIE, 2019.
- [80] C. D. Decker, W. B. Mori, K. C. Tzeng, and T. Katsouleas. The evolution of ultra-intense, short-pulse lasers in underdense plasmas. *Physics of Plasmas*, 3(5):2047–2056, 1996.
- [81] S. Steinke, J. van Tilborg, C. Benedetti, C. G.R. Geddes, C. B. Schroeder, J. Daniels, K. K. Swanson, A. J. Gonsalves, K. Nakamura, N. H. Matlis, B. H. Shaw, E. Esarey, and W. P. Leemans. Multistage coupling of independent laser-plasma accelerators. *Nature*, 530(7589):190–193, 2016.
- [82] Y. Wu, J. Hua, Z. Zhou, J. Zhang, S. Liu, B. Peng, Y. Fang, X. Ning, Z. Nie, F. Li, C. Zhang, C.-H. Pai, Y. Du, W. Lu, W. B. Mori, and C. Joshi. High-throughput injection–acceleration of electron bunches from a linear accelerator to a laser wakefield accelerator. *Nature Physics*, 2021.
- [83] E. Guillaume, A. Döpp, C. Thaury, K. Ta Phuoc, A. Lifschitz, G. Grittani, J. P. Goddet, A. Tafzi, S.-W. Chou, L. Veisz, and V. Malka. Electron Rephasing in a Laser-Wakefield Accelerator. *Physical Review Letters*, 115(15):155002, 2015.

-
- [84] A. Döpp, E. Guillaume, C. Thaury, A. Lifschitz, K. Ta Phuoc, and V. Malka. Energy boost in laser wakefield accelerators using sharp density transitions. *Physics of Plasmas*, 23(5):56702, 2016.
- [85] A. J. Howard, D. Turnbull, A. S. Davies, P. Franke, D. H. Froula, and J. P. Palastro. Photon Acceleration in a Flying Focus. *Physical Review Letters*, 123(12):124801, 2019.
- [86] J. P. Palastro, J. L. Shaw, P. Franke, D. Ramsey, T. T. Simpson, and D. H. Froula. Dephasingless Laser Wakefield Acceleration. *Phys. Rev. Lett.*, 124(13):134802, 2020.
- [87] S. Smartsev, C. Caizergues, K. Oubrierie, J. Gautier, J.-P. Goddet, A. Tafzi, K. Ta Phuoc, V. Malka, and C. Thaury. Axiparabola: a long-focal-depth, high-resolution mirror for broadband high-intensity lasers. *Opt. Lett.*, 44(14):3414–3417, 2019.
- [88] C. Caizergues, S. Smartsev, V. Malka, and C. Thaury. Phase-locked laser-wakefield electron acceleration. *Nature Photonics*, 14(8):475–479, 2020.
- [89] A. Debus, R. Pausch, A. Huebl, K. Steiniger, R. Widera, T. E. Cowan, U. Schramm, and M. Bussmann. Circumventing the Dephasing and Depletion Limits of Laser-Wakefield Acceleration. *Physical Review X*, 9(3):31044, 2019.
- [90] Mathias Hüther. Design and Characterisation of Supersonic Nozzles for Shock Front Electron Injection in Laser Wakefield Acceleration. Master’s thesis, Ludwig-Maximilians-Universität München, 2015.
- [91] Benedikt Günther. Design, implementation and characterisation of the 300TW-upgrade of the ATLAS laser system. Master’s thesis, Technische Universität München, 2014.
- [92] Shao-Wei Chou. *Investigation of electron acceleration and deceleration in plasmas*. PhD thesis, Ludwig-Maximilians-Universität München, 2016.
- [93] Y. Glinec, J. Faure, A. Guemnie-Tafo, V. Malka, H. Monard, J. P. Larbre, V. De Waele, J. L. Marignier, and M. Mostafavi. Absolute calibration for a broad range single shot electron spectrometer. *Review of Scientific Instruments*, 77(10):103301, 2006.
- [94] A. Buck, K. Zeil, A. Popp, K. Schmid, A. Jochmann, S. D. Kraft, B. Hidding, T. Kudyakov, C. M. S. Sears, L. Veisz, S. Karsch, J. Pawelke, R. Sauerbrey, T. Cowan, F. Krausz, and U. Schramm. Absolute charge calibration of scintillating screens for relativistic electron detection. *Review of Scientific Instruments*, 81(3):033301, 2010.
- [95] K. Nakamura, A. J. Gonsalves, C. Lin, A. Smith, D. Rodgers, R. Donahue, W. Byrne, and W. P. Leemans. Electron beam charge diagnostics for laser plasma accelerators. *Phys. Rev. ST Accel. Beams*, 14:062801, 2011.
- [96] T. Kurz, J. P. Couperus, J. M. Krämer, H. Ding, S. Kuschel, A. Köhler, O. Zarini, D. Hollatz, D. Schinkel, R. D’Arcy, J.-P. Schwinkendorf, J. Osterhoff, A. Irman, U. Schramm, and S. Karsch. Calibration and cross-laboratory implementation of scintillating screens for electron bunch charge determination. *Review of Scientific Instruments*, 89(9):093303, 2018.

- [97] J.-P. Schwinkendorf, S. Bohlen, J. P. Couperus Cabadağ, H. Ding, A. Irman, S. Karsch, A. Köhler, J. M. Krämer, T. Kurz, S. Kuschel, J. Osterhoff, L. F. Schaper, D. Schinkel, U. Schramm, O. Zarini, and R. D'Arcy. Charge calibration of DRZ scintillation phosphor screens. *Journal of Instrumentation*, 14(09):P09025–P09025, 2019.
- [98] Thomas Kurz. Calibration of scintillation screens for bunch charge determination in laser wakefield acceleration. Master's thesis, Ludwig-Maximilians-Universität München, 2015.
- [99] General Particle Tracer. URL <http://www.pulsar.n1/gpt/>.
- [100] R. Benattar, C. Popovics, and R. Sigel. Polarized light interferometer for laser fusion studies. *Review of Scientific Instruments*, 50(12):1583–1586, 1979.
- [101] IDEA - Interferometric Data Evaluation Algorithms. URL <http://optics.tu-graz.ac.at/idea/idea.html>.
- [102] Paolo Tomassini and Antonio Giulietti. A generalization of Abel inversion to non-axisymmetric density distribution. *Optics Communications*, 199:143–148, 2001.
- [103] J. Wenz, A. Döpp, K. Khrennikov, S. Schindler, M. F. Gilljohann, H. Ding, J. Götzfried, A. Buck, J. Xu, M. Heigoldt, W. Helml, L. Veisz, and S. Karsch. Dual-energy electron beams from a compact laser-driven accelerator. *Nature Photonics*, 13(4):263–269, 2019.
- [104] Felix M. Daiber. Generation of Few Cycle Pulses for Direct Observation of the Plasma Wave. Master's thesis, Ludwig-Maximilians-Universität München, 2015.
- [105] S. C. Mayo, P. R. Miller, S. W. Wilkins, T. J. Davis, D. Gao, T. E. Gureyev, D. Paganin, D. J. Parry, A. Pogany, and A. W. Stevenson. Quantitative x-ray projection microscopy: phase-contrast and multi-spectral imaging. *Journal of Microscopy*, 207:79–96, 2002.
- [106] A. Pukhov, S. Gordienko, S. Kiselev, and I. Kostyukov. The bubble regime of laser–plasma acceleration: monoenergetic electrons and the scalability. *Plasma Physics and Controlled Fusion*, 46:B179–B186, 2004.
- [107] S. M. Hooker, R. Bartolini, S. P.D. Mangles, A. Tünnermann, L. Corner, J. Limpert, A. Seryi, and R. Walczak. Multi-pulse laser wakefield acceleration: A new route to efficient, high-repetition-rate plasma accelerators and high flux radiation sources. *Journal of Physics B: Atomic, Molecular and Optical Physics*, 47(23):234003, 2014.
- [108] J. Cowley, C. Thornton, C. Arran, R. J. Shalloo, L. Corner, G. Cheung, C. D. Gregory, S. P.D. Mangles, N. H. Matlis, D. R. Symes, R. Walczak, and S. M. Hooker. Excitation and Control of Plasma Wakefields by Multiple Laser Pulses. *Physical Review Letters*, 119(4):1–6, 2017.
- [109] P. Tomassini, A. Giulietti, L. A. Gizzi, M. Galimberti, D. Giulietti, M. Borghesi, and O. Willi. Analyzing laser plasma interferograms with a continuous wavelet transform ridge extraction technique: the method. *Applied Optics*, 40(35):6561, 2001.

- [110] R. W. Gerchberg and W. O. Saxton. A practical algorithm for the determination of the phase from image and diffraction plane pictures. *Optik*, 35:237–246, 1972.
- [111] LightPipes for Python. URL <https://opticspy.github.io/lightpipes/index.html>.
- [112] M. Heigoldt, A. Popp, K. Khrennikov, J. Wenz, S.-W. Chou, S. Karsch, S. I. Bajlekov, S. M. Hooker, and B. Schmidt. Temporal evolution of longitudinal bunch profile in a laser wakefield accelerator. *Physical Review Special Topics - Accelerators and Beams*, 18(12):121302, 2015.
- [113] M. Förster, H. Ding, A. Döpp, M. F. Gilljohann, S. Karsch, T. Heinemann, T. Kurz, A. Irman, S. Schöbel, P. San Miguel, S. Corde, and O. Kononenko. Quantitative reconstruction of wakefield electron density distribution. Poster presented at Laser-Plasma Accelerator Workshop 2019.
- [114] Pablo Gabolde and Rick Trebino. Single-shot measurement of the full spatio-temporal field of ultrashort pulses with multi-spectral digital holography. *Optics Express*, 14(23):11460, 2006.
- [115] D. Haffa, J. Bin, M. Speicher, K. Allinger, J. Hartmann, C. Kreuzer, E. Ridente, T. M. Ostermayr, and J. Schreiber. Temporally Resolved Intensity Contouring (TRIC) for characterization of the absolute spatio-temporal intensity distribution of a relativistic, femtosecond laser pulse. *Scientific Reports*, 9(1):1–9, apr 2019.
- [116] K. K. Swanson, H.-E. Tsai, S. K. Barber, R. Lehe, H.-S. Mao, S. Steinke, J. van Tilborg, K. Nakamura, C. G.R. Geddes, C. B. Schroeder, E. Esarey, and W. P. Leemans. Control of tunable, monoenergetic laser-plasma-accelerated electron beams using a shock-induced density downramp injector. *Phys. Rev. Accel. Beams*, 20(5):51301, 2017.
- [117] E. Shestaev, D. Hoff, A. M. Sayler, A. Klenke, S. Hädrich, F. Just, T. Eidam, P. Jójárt, Z. Várallyay, K. Osvay, G. G. Paulus, A. Tünnermann, and J. Limpert. High-power ytterbium-doped fiber laser delivering few-cycle, carrier-envelope phase-stable 100 μ J pulses at 100 kHz. *Opt. Lett.*, 45(1):97–100, 2020.
- [118] H. Stark, J. Buldt, M. Müller, A. Klenke, and J. Limpert. 1 kW, 10 mJ, 120 fs coherently combined fiber CPA laser system. *Opt. Lett.*, 46:969–972, 2021.
- [119] Q. Du, D. Wang, T. Zhou, D. Li, and R. Wilcox. 81-beam coherent combination using a programmable array generator. *Opt. Express*, 29:5407–5418, 2021.
- [120] R. J. Shalloo, S. J.D. Dann, J.-N. Gruse, C. I.D. Underwood, A. F. Antoine, C. Arran, M. Backhouse, C. D. Baird, M. D. Balcazar, N. Bourgeois, J. A. Cardarelli, P. Hatfield, J. Kang, K. Krushelnick, S. P.D. Mangles, C. D. Murphy, N. Lu, J. Osterhoff, K. Pöder, P. P. Rajeev, C. P. Ridgers, S. Rozario, M. P. Selwood, A. J. Shahani, D. R. Symes, A. G.R. Thomas, C. Thornton, Z. Najmudin, and M. J.V. Streeter. Automation and control of laser wakefield accelerators using bayesian optimization. *Nature Communications*, 11:6355, 2020.

- [121] S. Jalas, M. Kirchen, P. Messner, P. Winkler, L. Hübner, J. Dirkwinkel, M. Schnepf, R. Lehe, and A. R. Maier. Bayesian optimization of a laser-plasma accelerator. *Physical Review Letters*, 126:104801, 2021.
- [122] A. R. Maier, N. M. Delbos, T. Eichner, L. Hübner, S. Jalas, L. Jeppe, S. W Jolly, M. Kirchen, V. Leroux, P. Messner, M. Schnepf, M. Trunk, P. A. Walker, C. Werle, and P. Winkler. Decoding Sources of Energy Variability in a Laser-Plasma Accelerator. *Physical Review X*, 10:31039, 2020.
- [123] A. Hanuka, C. Emma, T. Maxwell, A. S. Fisher, B. Jacobson, M. J. Hogan, and Z. Huang. Accurate and confident prediction of electron beam longitudinal properties using spectral virtual diagnostics. *Scientific Reports*, 11:2945, 2021.

Acknowledgement

First of all, I want to thank my supervisor Prof. Stefan Karsch for making this thesis work possible in the first place.

Special thanks go to Prof. Carl Schroeder for reviewing this thesis; to Prof. Malte Kaluza, for introducing me to this exciting research field and for constantly supporting my career development; to Prof. Simon Hooker, for improving the manuscript of my paper.

A sincere thank you goes to Andreas Döpp for the enlightening discussions, probably more importantly, for demonstrating me how to get a paper finished.

It was a blessing for me to have worked on the same team with Max Gilljohann, Johannes Götzfried, Sabine Schindler, Gregor Schilling, Moritz Förster, Thomas Kurz, Ludwig Wildgruber, and Felix Daiber. You made the long nights in the lab cheerful and memorable, unless Max hat sicher was vergessen.

I am grateful to Johannes Wenz, Konstantin Khrenikov, and Matthias Heigoldt. The lab and social skills you taught me made my ride in Garching much less bumpy.

Colleagues in Jena, Maria Reuter, Stephan Kuschel, at HZDR, Jurjen Coperus-Cabag, Arie Irman, at LOA, Olena Kononenko, Prof. Sebastien Corde, at DESY, Thomas Heinemann, thank you for the interesting experiments and fruitful follow-up discussions at your labs in which I was fortunate enough to participate.

And the very last, dearest Jiamin, thank you for all the love along the journey and useful tips during the hardest time of finishing this thesis.